1-1-2015

Chirped-Pulse Fourier Transform Microwave Spectroscopy In Pulsed Uniform Supersonic Flows

Chamara S.w Abeysekera
Wayne State University,

CHIRPED-PULSE FOURIER TRANSFORM MICROWAVE SPECTROSCOPY IN PULSED UNIFORM SUPERSONIC FLOWS

by

CHAMARA S.W. ABEYSEKERA

DISSERTATION

Submitted to the Graduate School

of Wayne State University,

Detroit, Michigan

in partial fulfillment of the requirements

for the degree of

DOCTOR OF PHILOSOPHY

2015

MAJOR: CHEMISTRY (Physical)

Approved by:

_____

Advisor Date

_____

_____

_____

DEDICATION

This Dissertation is dedicated to my Parents, Shelton &

Annuruddika Abeysekera

ACKNOWLEDGEMENTS

Grad school is a challenging, yet exciting experience in any person's life. I would like to take this opportunity in thanking each individual and group that helped me get through this important chapter of my life. At the top of the list are my parents and wife Samanthi, who always believed that I was someone important. Thank you for never doubting me in any of the decisions I made and for always standing alongside me, giving constant courage and motivation at every hurdle I faced.

Next, I am sincerely thankful to my advisor Prof. Arthur G. Suits for allowing me to be a part of this exciting journey of CPUF and supporting me financially throughout the whole period. I am forever grateful for his valuable guidance, encouragement, patience and positive attitude with me for the last five years.

I also take this opportunity to thank all the past and current Suits group members for making my stay in lab a productive and enjoyable one. I was fortunate enough to work with many postdocs from whom I learned a great deal of new techniques and acquired knowledge. I would like to thank Dr. James Oldham, Dr. Baptiste Joalland, Dr. Kirill Prozument and Dr. Lindsay Zack for supporting me and believing in my abilities. I would specially like to thank Kirill and Lindsay for training me, while answering all of my ridiculous questions about the CP spectrometer and microwave spectroscopy. I am extremely thankful for your sincere friendship.

I was privileged enough to work with Prof. Robert W. Field and his group at MIT and Prof. Ian R. Sims at Université de Rennes 1. Their valuable insights and resourceful

support in their respective fields is highly commended and was vital in developing the instrument. I also thank my committee members Prof. Wen Li, Prof. Parastoo Hashemi and Prof. David Cinabro for their valuable time, suggestions and comments during the preparation of my dissertation.

This would have not been easy without the nice administrative staff in Chemistry Department. I want to thank Melissa Barton, Mary Wood, Diane Kudla, Erin Bachert, Debbie McCreless and Bernie Meisik for all their help throughout my study and Nestor Ocampo for his friendship and technical support with computers. Last but not least, all my relatives, friends, colleague and their families who had helped me in numerous ways in making this journey much smooth and enjoyable.

PREFACE

This dissertation is based closely on the following refereed publications:

Chapter 2:

J. M. Oldham, C. Abeysekera, B. Joalland, L.N. Zack, K. Prozument, G.B. Park I.R. Sims, R.W. Field, and A.G. Suits, A Chirped-Pulse Fourier-Transform Microwave/Pulsed Uniform Supersonic Flow Spectrometer: I. The Low-Temperature Flow System. *J. Chem. Phys.* (2014) **141**, 154202.

C. Abeysekera, B. Joalland, Y. Shi, A. Kamasah, J.M. Oldham, A.G. Suits, A short-pulse high-intensity molecular beam valve based on a piezoelectric stack actuator. *Rev. Sci. Instrum.s* (2014) **85**, 116107.

Chapter 4:

C. Abeysekera, L.N. Zack, G.B. Park, B. Joalland, J.M Oldham, K. Prozument, N.M. Ariyasingha, I.R. Sims, R.W. Field, A.G. Suits, A Chirped-Pulse Fourier-Transform Microwave/Pulsed Uniform Supersonic Flow Spectrometer: II. Performance and applications for reaction dynamics. *J. Chem. Phys*. (2014) **141**, 214203.

Chapter 5:

C. Abeysekera, B. Joalland, N. Ariyasingha, L.N. Zack, I. Sims, R. W. Field, A. G. Suits, Product branching in the low temperature reaction of CN with propyne by chirped-pulse microwave spectroscopy in a uniform supersonic flow. *J. Phys. Chem. Lett*. (2015) **6**, 1599−1604

Table of Contents

LIST OF TABLES

LIST OF FIGURES

CHAPTER 1

Introduction

The pursuit for better understanding of our adjacent surroundings has always been curious enough to drive us towards new explorations. Most common observables in our immediate environments, like heat color, smell, and taste, are a combination of collective elementary chemical steps that can be understood by basic chemical principles. With the beginning of the twentieth century and the development of chemical kinetics and thermodynamics had unlocked new insights into these elementary processes, giving us a better ability to explore and control these reactions. However, thermal rate methods are not adequate to provide solid explanations of discrete events in chemical reactions, as they present averages of many random collisions of atoms, molecules, radicals or ions. Nevertheless, this opened up many avenues for fundamental chemical experiments towards understanding chemical processes and its dynamics.

The curiosity to examine into more intimate details of chemical reactions, and greater interest in the chemical journey rather than just the final designation (creating products) made the field of reaction dynamics attractive to chemical explorers. The field was well recognized in 1986 with Herschbach[1], Lee[2] and Polanyi[3] sharing the Nobel prize in chemistry for their contribution towards understanding the dynamics of elementary reaction processes. Understanding the molecular level information of the underlying dynamics of atom-diatom reactions and photochemical processes is achieved

through the collaborative effort of theory, computation and experiments. Accuracy of theory, efficiency of computing and sensitivity of experiments are the vital elements. Developing more sensitive experimental techniques is always a key priority to extract more information from a chemical system. Widely used, sensitive detection techniques to probe product for physical chemists include, mass-spectrometry[4], H-atom Rydberg tagging[5], resonance enhanced multiphoton ionization (REMPI)[6], laser-induced fluorescence (LIF) spectroscopy[7,8], and ion imaging[9,10]. Although, these techniques are highly sensitive they face serious challenges in correlating signal intensities to the actual number of reaction products. Even relative quantities are seldom determined with confidence and the techniques rarely provide detailed structural information.

Currently in our laboratory we employ state-selected REMPI and "universal" velocity map imaging[11] of the products of photochemical and crossed beam scattering reactions. These methods have provided deep insight into fundamental reaction dynamics. Still, considerable challenge exists in extending the power of these methods to more complex systems. The detection methods used in these studies typically do not provide isomer- and vibrational level-specific information for polyatomic products, so that product energetics or reaction dynamics must be used, when feasible, to draw conclusions about the product isomer identity. For complex systems, the translational energy and angular distributions are often broad and unstructured, so that little detailed information can be extracted. Even when product identity maybe inferred, for complex polyatomic systems these approaches rarely provide reliable product branching information. In general, product vibrational distributions are not readily available for

systems beyond four atoms, and rarely even for that case. Therefore, the need arises for an isomer and conformer specific detection method, which can quantify and spectroscopically characterize, with detailed product branching and vibrational distributions, unstable reaction products and intermediates in ground and excited states.

To address these limitations, a new instrument/method was developed. This dissertation discusses the theory, design, construction and operation of the new apparatus, which combines two unique techniques: chirped-pulse Fourier-transform microwave spectroscopy and pulsed uniform supersonic flows. Combining the broadband microwave capability of the chirped pulse technique with a cold molecular flow system designed to produce high enough densities to initiate bimolecular reactions provides an complementary means for fundamental studies in spectroscopy and reaction dynamics, kinetics, combustion and atmospheric chemistry, and astrochemistry.

Uniform supersonic flow systems are generally used to measure reaction kinetics at ultralow temperatures. It is important to recognize that these flows are entirely distinct from supersonic jet expansions. These flows are capable of generating very large volumes of gas thermalized at constant translational and rotational temperatures of 50 K or below and at uniform pressure. Traditionally, the main drawbacks of theses systems are that they must be run continuously and require extensive pumping, large gas loads and considerable space for operation. In Chapter 2, a detailed description of a new approach to produce a tabletop Pulsed Uniform Supersonic Flow (PUSF) system with modest pumping requirements will be discussed. The key significance of this approach is that it still has the ability to produce similar long uniform and cold (<30 K) pulsed molecular

beam with same high density as the continuous beams, but with fewer pumps and reduced gas consumption.

The development of the Chirped-Pulse Fourier Transform Microwave (CP-FTMW) spectroscopic technique by Brooks Pate and co-workers[12] enabled the shot-to-shot broadband capability for rotational spectroscopy towards a powerful probe in the study of gas phase chemical applications. Its comparable resolution with the conventional FTMW cavity spectrometers is well suited for detection and discrimination among gas-phase species that possess a non-zero electric dipole moment. The spectral coverage provided by the truly broadband (>10 GHz) chirped-pulse Fourier-transform technique suggests possibility of microwave spectroscopy as an essential and nearly universal tool for chemical kinetics and dynamics with additional molecular structural information. Chapter 3 provides a brief introduction to the domain of rotational spectroscopy, and about the CP-FTMW technique.

In the past, the direct microwave detection schemes had been judged inferior to laser-based absorption, fluorescence, and ion-detected schemes due to narrow band capability and less sensitivity. The high spectral acquisition rate of CP-FTMW spectroscopy, coupled with the PUSF will enhance the signal allowing it to be applicable much as laser-based probes. This approach offers additional information on specific conformer and vibrational level population ratios more completely and directly than any existing detection schemes. The merger of these two techniques into one assembly is a new experimental apparatus: Chirped Pulse in /Uniform Flow spectrometer (CPUF). In Chapter 4 the configuration, evaluation and performance of CPUF are demonstrated

along with its potential to detect and characterize products initiated by both photochemical and bimolecular reaction.

The ultimate drive of reaction dynamics is to look at the individual collisions of atoms, molecules, radicals, or ions and characterize the products, their identity, energy and internal state distribution. These experiments are widely performed by crossing two collimated molecular beams usually perpendicular to each other. The scattered products are probed using variety of distinctive detection techniques; in our laboratory universal ion imaging is used. The products velocity and angular distributions are measured, where the product velocity distributions supply useful information on how the total available reaction energy is partitioned into translation, rotation, or internal excitation of the products. The details of the reaction mechanism and information on the lifetime of the collision complex are provided by the product angular distribution. Nevertheless, two crucial aspects of the reaction are missing from the detailed crossed-beam imaging technique. If the resultant product has several possible isomers, the product isomer identity and the branching ratios among them is not revealed. In addition, with reactions having competing multichannel pathways leading to several products, no reliable method exists to compare their relative branching between the direct and indirect channels and among themselves. Chapter 5 is a demonstration of CPUF`s ability and potential to quantitatively determine product branching from a multichannel bimolecular reaction.

Future prospects and new designer chirping schemes developed for CPUF to explore broader chemical applications are discussed in Chapter 6.

CHAPTER 2

Pulsed Uniform Supersonic Flows

2.1 Introduction

Cold molecular beam sources are of considerable importance in spectroscopy and reaction dynamics. A cold source in spectroscopy will result in reduced spectral congestion since lower energy levels of a molecule are preferentially populated. Having increased possible interaction times can also potentially lead to higher spectral resolution. Cold and controlled molecular beams can benefit reaction dynamics studies in two main ways. First, slow molecules have reduced collision energies and provide methods to study quantum effects in molecular scattering. Secondly, molecular beams with narrow and tunable velocity distributions give access to details of scattering events at higher collision energies. The most common and widely used method to produce cold molecular beam source is through pulsed jet expansion. However, there are numerous disadvantages associated with it. This approach in some applications such as with microwave probe as described here. The jet conditions are non-equilibrium environments, in which the temperature varies strongly along the beam for the first several nozzle diameters, and the density varies throughout the expansion, so reactive processes and photochemical systems cannot be cooled and thermalized in any consistent or reliable way. In addition, the total number of sample molecules available in the irradiated volume is necessarily limited, constraining the maximum signal levels possible. To counteract these limitations an alternative is a uniform supersonic flow system. The CRESU technique (a French

acronym for Reaction Kinetics in Uniform Supersonic Flows) was designed to measure reaction kinetics at very low temperatures[13–18]. These flows are distinct from normal supersonic jet expansions in their ability to generate very large volumes of gas thermalized at constant translational and rotational temperatures of 50 K or below at uniform pressure. The key component for this approach is the use of a Laval nozzle.

A Laval nozzle is a convergent-divergent nozzle, which has the ability to accelerate carrier gases to higher Mach numbers in its axial direction, through the conversion of heat energy of the flow into kinetic energy. The initial part of the axisymmetric nozzle is a short convergent section where the flow begins to accelerate from a near zero hydrodynamic velocity residing in a stagnation region. The accelerated gas then encounters the throat region where the diameter of the nozzle is at a minimum; at this point the flow reaches Mach 1. Maintaining a sufficient pressure drop across the nozzle, supersonic flow speeds become possible at the divergent region. Therefore, under Laval expansion the convergent part of the nozzle accelerates to a subsonic flow, while the divergent section accelerates supersonic flow. In order for a uniform acceleration along the nozzle, at least Mach 1 should be maintained at the minimum area.

The original CRESU technique employed a continuous flow system. Although continuous uniform supersonic flow systems offer an advantage over pulsed jet sources, there remain some disadvantages associated with them. A major drawback is that they consume vast quantities of gas and make extraordinary demands on the pumping systems, rendering them too large and expensive for widespread use and precluding their use when expensive or scarce reactants are needed. To overcome these limitations, one could

reduce the Laval nozzle dimensions, with the disadvantage of reducing the molecular cooling capabilities and reactant volumes,[19] or pulse the uniform supersonic expansion, as pioneered by the Smith group at Arizona.[20,21] Advantages of these pulsed systems have been demonstrated for many applications[22–28]. One shortcoming of these designs, however, is that they have all been based on the use of solenoid-actuated valves that deliver limited gas throughput. Because establishing a stable flow requires reaching stable target pressures upstream of the flow, typically ≥ 50 mbar in the stagnation region, small reservoir volumes have been employed and in some cases the valve is fired directly in the nozzle throat. Under these conditions, due to the minimal reservoir volume, the gas passes through the nozzle almost instantaneously and the valves may be held open for comparatively long times (> 10 ms) while a steady state builds throughout the setup. In part because the flow velocity prior to the convergent part of the nozzle is nonzero, the characteristics of the flow after the nozzle are altered. In particular, the flow temperature is higher than would be expected from a continuous flow with the same nozzle design. To date, pulsed uniform supersonic flow (PUSF) systems employing solenoid valves have not demonstrated flow temperatures below about 39 K,[29] with T~70-90 K typically achieved. In an alternative approach developed recently, the reservoir is continuously filled, as it would be for a continuous nozzle, but the transmission of gas through the nozzle is pulsed by use of a high-speed spinning disk or chopper sealed in the divergent side of the Laval nozzle. Although this method reduces gas consumption and offers optimal flow conditions validated at 23 K,[8] it is experimentally challenging to implement and results in only a reduction of a factor of 10 in gas consumption, thus it still requires

substantial pumping.

In this chapter, a new approach is presented to generate pulsed uniform supersonic flows with temperatures as low as 20 K. This method, relying on use of a high-throughput piezoelectric stack valve, offers increased ease of use and flexibility, while reducing the gas load and demands of the pumping system to 0.5-5% relative to the continuous case. The effectiveness of this technique is demonstrated through impact pressure measurements and spectroscopic characterization. These data confirm that a high-density, uniform flow with temperatures and densities around 20-30 K and 10^{16} cm^{-3}, respectively, is achieved in both argon and helium carrier gases.

2.2 Development of a Pulsed Low Temperature Flow system

2.2.1 Vacuum simulations and design consideration

Laval flows suitable for dynamics and kinetics studies typically employ pressures on the order of 40–80 mbar in the stagnation region prior to the nozzle and 0.1–0.6 mbar in the flow region. For example, a typical continuous flow of 35 SLM (standard L min^{-1}) at a pressure of 0.4 mbar in the flow chamber requires a pumping speed of more than 20,000 L s^{-1}. This volume flow rate requirement places enormous demands on the pumping system, thus the typical continuous flow systems employed in kinetics studies use large Roots blowers to handle this gas load. For our purposes, a system operating at 2–10 Hz is acceptable if a stable flow on the order of 1 ms duration can be established. For a 2 ms pulse at 10 Hz, we reduce the volume throughput of the prototype argon flow discussed above to 0.7 SLM. Although this pressure regime (0.1-0.6 mbar) is well

matched to Roots blowers, they have undesirable qualities such as noise, vibration, and a need for regular maintenance. Modern compound turbomolecular pumps based on magnetic levitation present an appealing alternative. They can readily achieve the target volume flow rates at these pressures, as well as being silent and essentially maintenance-free. We have thus chosen a high-throughput compound turbomolecular pump as the primary pumping stage for the flow. In our designs, the stability of pressure conditions over several cycles was also considered. A one-dimensional model of the flow conditions through the chamber suggested that there is rapid convergence to steady-state pressure conditions in the flow chamber, and complete evacuation of the chamber between pulses is unnecessary.

Improvement of the pulsed flow conditions to match the low temperatures obtained by continuous flows suggests two significant changes to the reservoir loading scheme from those used in other pulsed Laval systems. Firstly, a reservoir volume of ~15 cm^3 was chosen to ensure a negligible mean reservoir gas velocity prior to entry into the nozzle. Also, the flow characteristics of the gas through the nozzle must closely approximate those calculated for a specific nozzle design. Secondly, the reservoir must be capable of rapid loading; with the reservoir pressure required to be above the optimal uniform flow immediately after the loading ends. This rapid loading is deemed necessary since there is no barrier to flow through the nozzle, which results in flow beginning as soon as a positive pressure difference occurs between the reservoir and the flow chamber. Rapid loading thus minimizes the consumption of gas that would otherwise be wasted while the reservoir pressure is brought up to the desired value. Slow loading also leads to

greater total gas consumption, because much longer pulses are then required. In ideal circumstances, loading should be complete within a few hundred microseconds, which demands a flow rate through the valve that must for a brief period greatly exceed the continuous flow requirement of 35 SLM. This flow rate is larger than what is typically possible with a conventional solenoid valve. Therefore a piezoelectric stack valve inspired by the work of the Gentry group, which combines high forces and linear displacement, was designed to meet this requirement.

2.2.2 Development of a high throughput piezoelectric stack valve

Valves based upon piezoelectric transducers were developed in the early 1980's as molecular beam sources.[30] The initial designs evolved through contributions from several groups and an optimal design by Proch and Trickl has seen very wide use since then. This design combines a piezoelectric disk actuator with a high-voltage (HV) switch, which has been improved by dual piezo actuators.[31] These valves have the advantage of very fast opening times and translational motion of ~100 μm. However, they still show important shortcomings such as pulse durations typically higher than 50 μs, low repetition rates, and limited gas flows. An alternative approach pioneered by Gerlich and coworkers and refined by Janssen and coworkers[32] employs a cantilever piezo actuator that is capable of very fast opening times and high repetition rates, but the forces are extremely limited and the range of motion is also quite constrained. Disk actuators have typically a maximum pulling force of only 10 N, which limits their ability to open large nozzles at high pressure. Recently, fast acting valves based on magnetic or electromagnetic actuators were developed to overcome these limitations.[33,34] In this

section we discuss the development of a new, robust valve that instead employs high-force piezoelectric stack actuators (PSAs). These actuators can achieve up to 180 μm linear motion of the plunger with pushing and pulling forces up to 4500/500 N, respectively. The smallest PSA used in our laboratory, i.e. the least expensive one (Physik Instrumente, P-212.40) was used for the molecular beam characterization and was still able to demonstrates significant improvement in pulse duration and molecular densities compared to disk translators. Larger PSAs (P-212.80 and P-216.90) could be used for different molecular beam experiments with specific interests.

A schematic of the valve is shown in Figure. 2.1 the segmented approach allows for easy accommodation and switching between different PSAs, making its design versatile for various applications. The PSA must be mounted solely by its back, as any torques on the plunger can damage it. A stainless steel cylinder that is open along half its diameter along its length supports the PSA. This half-cylinder is connected to the micrometer at one end and to the base of the valve at the other. To prevent any torque, a Teflon ring is placed around the stack, forming a snug fit with the inside of the cylinder to restrict all lateral movement. A differential thread micrometer with a non-rotating spindle (Mitutoyo 110-102) is attached to the PSA through a custom made adapter that allows fine adjustments in order to regulate the gas volume delivered through the nozzle orifice. The valve body consists of a cylindrical stagnation chamber of 2.5 cm^3, which embodies the plunger attached to the PSA. A ferrule, mounted on a chamber cap, compresses an o-ring onto the plunger to seal the stagnation chamber. At the tip of the plunger another o-ring seals the chamber when the valve is closed. Note that the base of

the valve is designed to function independently of the used PSA, therefore switching to a higher force PSA exhibiting a longer length would only require modifying the length of the half-cylinder or the adapter. This design also ensures that the actuator avoids any contact with corrosive gases that could reduce its lifetime.

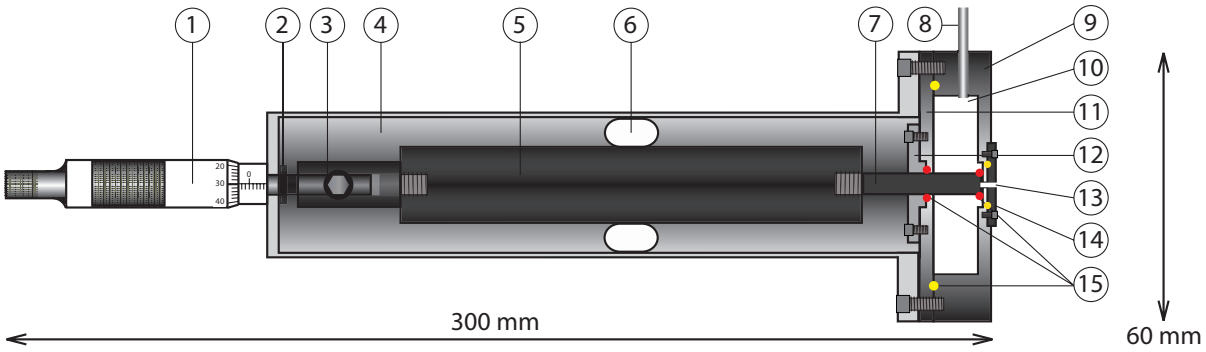

1	micrometer	6	teflon guide	11	chamber cap (SS)
2	nut	7	plunger (SS or Al)	12	ferrule (Al)
3	adapter (Al)	8	gas inlet (SS 1/16″)	13	nozzle (SS 1mm)
4	half-cylinder (SS)	9	valve body (SS)	14	front plate (SS)
5	piezostack actuator	10	stagnation chamber	15	viton/kalrez o-ring

Figure 2.1: Schematic view of the valve assembly. The piezostack actuator is mounted and aligned outside of a stainless steel valve body in a half-cylinder. The valve is sealed by Kalrez o-rings (yellow spots) both at the tip and at half-length of the plunger. Other o-rings are shown in red.

The valve operates through the application of a high-voltage pulse to the actuator. In its closed position, a voltage of +800 V is applied from an HV power supply that delivers an average power of 200 W (Kepco BHK 1000-0.2MG). To open the valve, the actuator is grounded by switching the actuator voltage to 0 V with a fast HV transistor

switch (Behlke HTS 61-03 GSM) combined with a high-capacitance RC circuit (R = 1 Ω, C = 20 μF).

This design was developed both for loading the Laval flow and as a pulsed molecular beam source. We first present demonstration of its performance as a pulsed beam source. For these results, the gas was expanded through a 1 mm orifice. The micrometer head was connected to a rotary motion feedthrough to allow for adjustment of the plunger once the valve was placed into vacuum.

We used the dc slice ion imaging technique[11] to measure the velocity distributions of the pulses. A pulse delay generator controlled the valve and the different ion imaging modules (Berkeley Nucleonics Corp. 575-8C). The molecular beam was skimmed by a 1 mm skimmer (Beam Dynamics) at 4 cm downstream from the nozzle tip along the propagation axis, and ionized 12 cm further downstream by an unfocused F_2 excimer laser (GAM EX-10) generating 10 ns pulses at λ = 157 nm (hν = 7.9 eV). The ions were directed by the electric field of a dc lens assembly to a multichannel plate (MCP) coupled to a phosphor screen (P-47). The MCP back plate was kept grounded and the front one was pulsed at +1500 V, while a voltage of +4500 V was applied to the phosphor screen. The data acquisition was composed of a CCD camera running through the NuAcq-2 software.[35] Note that the laser beam crosses the molecular beam at 45° in our 90° crossed molecular beam apparatus,[36] therefore the irradiated volume is broadened compared to a perpendicular geometry, although we did not add any correction to the results shown.

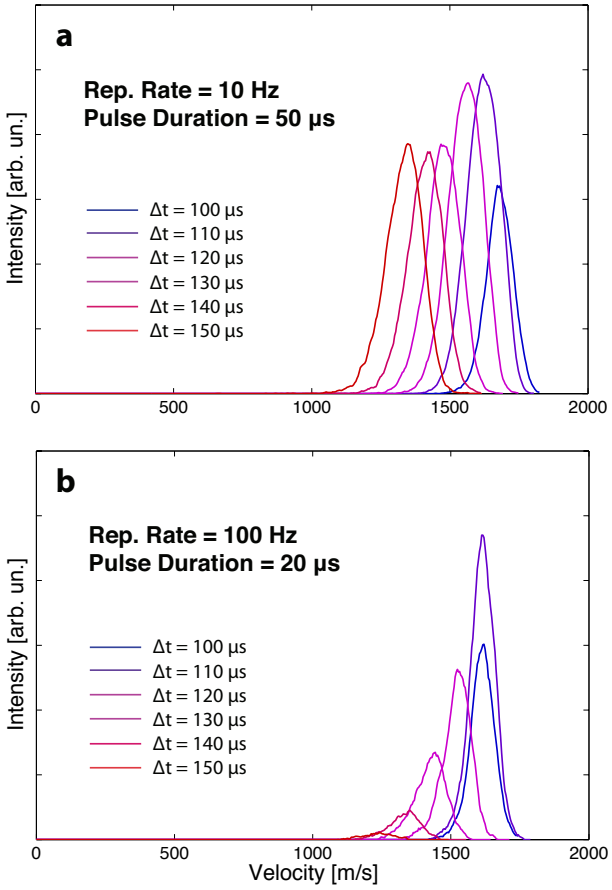

Figure 2.2: Beam profiles at valve/probe delays Δt in the 100-150 µs range for dimers of 2,5-dimethylfuran seeded in He (0.25%). The data were recorded with dc slice ion imaging using an unfocussed F_2 excimer laser (λ = 157 nm, hν = 7.9 eV) with a 35 mm^2 cross-section. (a) Repetition rate of 10 Hz and pulse duration of 50 µs. (b) Repetition rate of 100 Hz and pulse duration of 20 µs.

The data were recorded for dimers of 2,5-dimethylfuran (DMF_2, m/z = 196, $IE_{monomer}$ = 7.9 eV) with DMF diluted at 0.25% in helium. These are readily ionized by a single photon at 157 nm. The stagnation pressure was 6 bar. The beam profiles were measured at valve-opening/VUV-probe delays, Δ*t,* between 100 and 150 µs to cover the entire duration of the gas pulses. These profiles are shown in Figure 2.2 for pulse durations of 50 and 20 µs and for repetition rates of 10 and 100 Hz, respectively. For 50

μs pulse durations, the most probable beam velocity, *v,* decreases linearly with delay time. The total average speed across the entire pulse $\bar{v}$, is equal to 1500 m/s. The total speed ratio, S_{tot}, estimated as $\bar{v}\ /\Delta v$ over the sum of the different Δt distributions with Δv, the full width at half maximum of the spread, is equal to ~ 4 (Table 2.1). The local speed ratios, S_{loc}, show higher values equal to ~ 10 at maximum intensity. The 20 μs pulses recorded at a repetition rate of 100 Hz are overall significantly narrowed, both in local and total irradiation conditions, where S_{loc} and S_{tot} are 16 and 11, respectively. Here, the beam is focused in the early high-speed region of the supersonic expansion, with the pulse tail rapidly vanishing at $\Delta t > 120$ μs. Hence, the sum of the early distributions with $100 < \Delta t < 120$ μs corresponds to more than 80% of the total distribution. The two first local distributions show similar average speeds (1650 m/s), illustrating the net improvement in cooling efficiency while preserving high beam intensity at lower pulse duration. Higher local speed ratios could be obtained by interrogating a smaller local volume with a focused probe.

Table 2.1: Speed ratios S_{loc} and S_{tot} estimated from the velocity distributions shown in Figure 2.2 ($S = \langle v \rangle / \Delta v$). S_{loc} is calculated from the velocity distribution with maximal intensity, and S_{tot} is calculated from the mean velocity of the sum of the different velocity distributions. Δv is estimated as the corresponding full width at half-maximum.

Rep. Rate (Hz)	**Pulse Duration (μs)**	**S_{loc}**	**S_{tot}**
10	50	11	4
100	20	16	11

This robust valve design, based on a high-force piezoelectric actuator, offers an alternative to solenoid and piezoelectric disk valves for producing molecular beams with a greater intensity and shorter pulse duration. Here we show that this valve could be particularly useful in experiments where short pulses with high speed ratios are needed, such as low collision energy experiments with both crossed- and merged-beam configurations[37,38]. One could also easily achieve higher repetition rates by cooling the valve to limit heat dissipation as this type of actuators exhibit resonant frequency of several kHz. This design can also be used to generate pulsed uniform supersonic flows by enlarging the nozzle diameter to allow for repetitively fast loads of the stagnation reservoir prior to the desired Laval expansion. This is described in the following pages.

2.2.3 Assembly of the Pulsed Low Temperature Flow system

A schematic diagram of the experimental apparatus, which satisfies the considerations and restrictions discussed in section 2.2.1, is shown in Figure. 2.3, and is briefly described here prior to a more detailed description below of each of the individual components. The piezoelectric stack valve repetitively fills the reservoir upstream from the Laval nozzle. Two Laval nozzles, designed for uniform flows of different flow velocities and carrier gases (helium and argon), have been fabricated. The carrier gas flows out of the nozzle into the reaction chamber, a cylindrical polycarbonate tube with a volume of 50 L, that is transparent to visible and microwave radiation. Microwave horns on opposite sides of the chamber transmit and receive microwave radiation, as described fully in a following chapter. The chamber is mounted on a home-built translation stage so

that its movement along the propagation axis permits interrogation of the flow at various downstream distances from the nozzle while keeping the antennae positions fixed. Two fast pressure transducers, one located in the reservoir and the other mounted in a Pitot tube downstream of the nozzle, are used to monitor flow pressures so that the required conditions are achieved. Aluminum flanges are mounted on each end of the polycarbonate tube and sealed with o-rings. A turbomolecular pump coupled to a dual stage rotary pump is connected to the downstream end of the chamber.

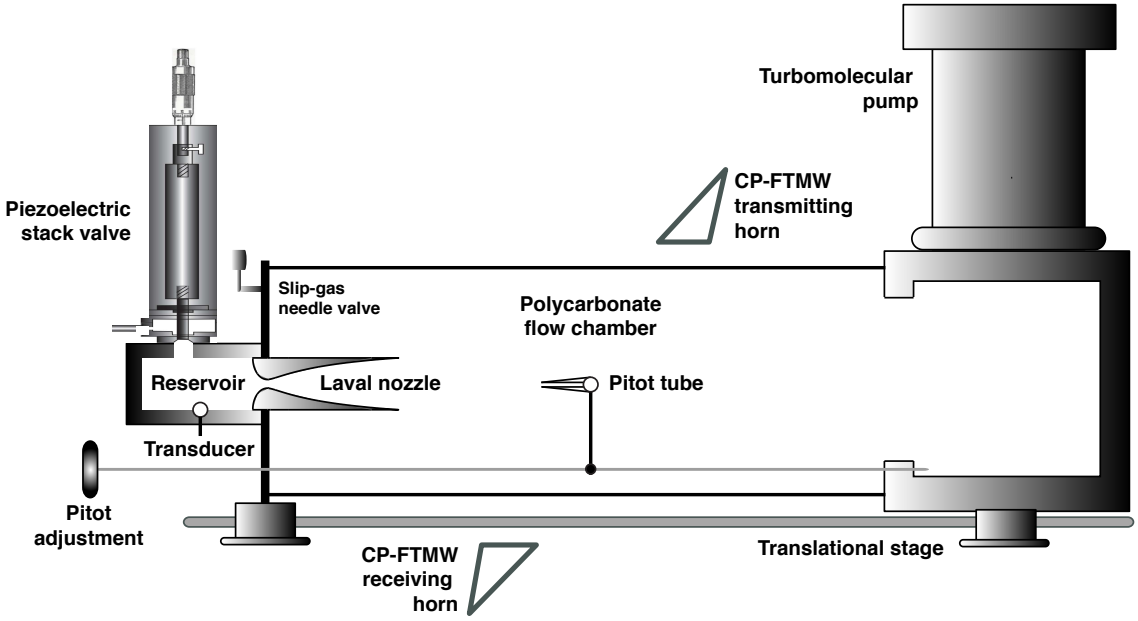

Figure 2.3. The pulsed uniform supersonic flow system. The stacked piezoelectric valve is mounted on a reservoir ("settling chamber") outside of the vacuum chamber. Pressures in the settling and main chambers are monitored by pressure transducers mounted on the reservoir and inside of a Pitot tube, respectively. The vacuum chamber consists of a polycarbonate tube of outside diameter ~ 30 cm which is transparent in the microwave spectral region. The figure is not to scale.

A schematic of a similar piezoelectric stack valve, discussed in section 2.2.2 is shown in Figure. 2.4, the valve employs a larger and more powerful piezoelectric stack actuator (Physik Instrumente, P-212.80). This actuator can achieve up to 120 μm linear motion of the plunger with 2000 N pushing and 300 N pulling, which is fifteen times greater than the disk translators. As a result, large nozzles can easily be opened quickly against very high backing pressures, and the piezo stack can readily be isolated from the gas itself.

The plunger is composed of a 4 mm diameter, 2.5 cm long cylinder that is directly screwed onto the actuator; a groove is cut at the end of the plunger for a Kalrez o-ring that seals off the 2.5 cm^3 stagnation volume of the valve from the reservoir. Alternatively, a T shaped plunger can be used to seal off the nozzle on the outer side of the front plate, thus operating in a normally-closed mode, as these actuators are extended when a potential is applied. We have successfully tested both approaches, although we present here only the results obtained with a linear plunger in a normally-open configuration. Same micrometer head (Mitutoyo 110-102) allows for fine adjustment of the actuator and plunger to maximize the gas flow. The valve is mounted vertically onto a 15 cm^3 cylindrical reservoir, which serves as a settling region prior to flow through the nozzle. When the valve is fully open, gas flows into the reservoir through a cross-section of ~1.5 mm^2. The valve is closed by applying a constant high voltage (+800V) from a HV power supply. The applied voltage is rapidly grounded by a HV fast switch (Behlke HTS-61-03-GSM), which causes the piezoelectric material to contract, thereby opening the valve. The voltage is rapidly switched on again to reclose the valve. Repetition rates of 2 to 10

Hz and pulse widths with various durations are controlled by a pulse delay generator (Berkeley Nucleonics Corporation 575-8C).

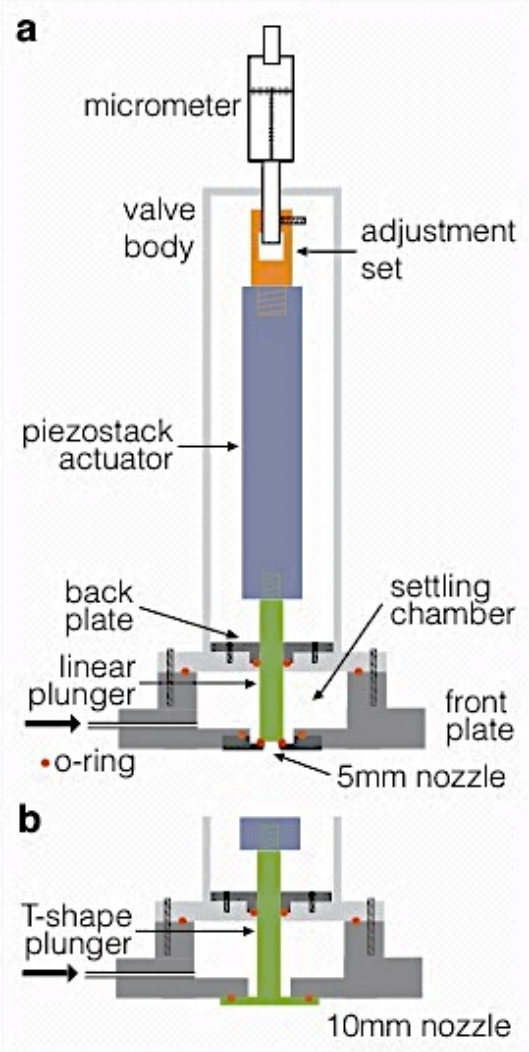

Figure 2.4. Cut-away view of the valve assembly. The piezostack actuator (blue) is mounted in a stainless steel valve body (light grey). The position of the plunger (green), either linear (a) or T-shaped (b), is adjusted by a micrometer. The different o-ring positions are symbolized by red circles. In particular, the plunger is sealed at two positions, i.e. by an o-ring at the nozzle itself, and by another o-ring fixed at the top of the plunger, with its tightness adjusted by varying the pressure exerted by the back plate.

The PUSF system can accommodate one of two in-house machined Laval nozzles that are designed to produce uniform supersonic flows, one for a argon flow, the other for a helium flow. Mach numbers of 5.47 from the argon nozzle and 5.45 from the helium nozzle can be achieved with the generated nozzle profiles. The nozzles are machined from aluminum alloy 2024 with an outer diameter of 74 mm. The throat and exit diameters are respectively 8 and 55 mm for the argon nozzle and 3 and 20 mm for the helium nozzle. The design pressures for the reservoir (P_0) and the flow chamber (P_f), as well as the other design profile parameters, are shown in Table 1.

The pumping scheme consists of an 1100 L s^{-1} (N_2) compound turbomolecular pump (Osaka Vacuum, TG1113MBW-90) backed by a 20 L s^{-1} (N_2) rotary pump (Edwards E2M80). This combination can maintain an operating pressure in the chamber up to 0.6 mbar while the valve is in operation, with repetition rates of 1-10 Hz, and an unloaded pressure on the order of 10^{-6} mbar. The pressure inside the chamber is monitored using a calibrated pressure transducer (MKS Baratron), mounted at the end of the chamber. The flow conditions are monitored by two pressure transducers (Kulite XCEL-100-5A). One transducer is mounted on the reservoir wall and the other inside a Pitot tube, which can be longitudinally and radially adjusted along the flow propagation axis with a rotary-linear motion feedthrough (MDC vacuum). The outputs of the two sensors are amplified by a signal conditioner (Endevco model 126) and monitored on a 100 MHz oscilloscope (Tektronix DPO2014B). After calibration of the transducers with the Baratron pressure gauge located inside the flow chamber, the flow duration, temperature profile, Mach number, and density along the flow axis can be determined

(see Sect. 2.2.4).

Several steps are taken in order to ensure the uniformity of the flow. The vital aspect of Laval nozzle expansion to achieve desired temperature is to have a stationary gas prior to the nozzle. To satisfy this criterion we use a larger cylindrical reservoir in contrast to previous attempts[39]. Even though a larger reservoir is used, the reservoir pressure required is invariant of its volume; amount of gas loaded can be controlled by the pulse widths. By over pressuring the reservoir, the exact pressure conditions are obtained at some latter point of the gas flowing out the reservoir and through the nozzle to give a uniform flow at the designed temperature range from 200-500 microseconds. This method also reduces flow turbulence, a common problem in other pulsed Laval systems. Equalizing the flow pressure with the chamber can minimize boundary layer formation, either by varying the repetition rate of the gas pulse or by loading a slip gas directly into the chamber through a needle valve.

2.2.4 Flow characterization

The performance of both the helium and argon nozzles was characterized by impact pressure measurements (Sect. 2.2.4.A). In doing so, 2D profiles of the flow temperatures and densities were obtained to estimate the isentropic core and boundary layer dimensions. Additionally, the temperature of the helium flow was independently determined via a Boltzmann analysis using the integrated line intensities of several pure rotational transitions of dimethyl ether, CH_3OCH_3, and acetaldehyde, CH_3CHO (Sect.2.2.4.B).

A. Impact pressure measurements

The profiles of the flows of the Ar and He Laval nozzles, based on the impact pressure measurements, are shown in Figure 2.5. The impact pressures were recorded along the flow axis with the Pitot tube initially oriented such that the pressure transducer was located at the nozzle exit, and then in 1 cm downstream increments. In the Ar profile (Figure. 2.5a), the flow is very stable and uniform out to distances of almost 20 cm from the nozzle exit. The impact pressure shows negligible fluctuations over a duration of about 4 ms shortly after the valve opening, staying at ~ 7 mbar. Further evidence that the flow is well collimated and uniform is given by the radial distributions shown at linear distances 1, 8, and 16 cm in Figure 2.5b. In the He profile (Figure. 2.5c), the impact pressure fluctuates moderately from the nozzle exit to a linear distance of around 12 cm, and then begins to decrease. Nonetheless, through the core, the impact pressure remains relatively constant at around 7 mbar. The radial profiles of the helium flow at 0, 4, 8, and 10 cm from the nozzle exit (Figure. 2.5d) are similar to each other, although they reach maximum values at increasingly lower impact pressures, reflecting the tapered profile in Figure 2.5c. These curves do not display the pronounced “flat-top” appearance of the argon radial distribution, and the decrease in impact pressure relative to radial distance seems more gradual. These differences can be attributed to the much smaller inner diameter of the He nozzle.

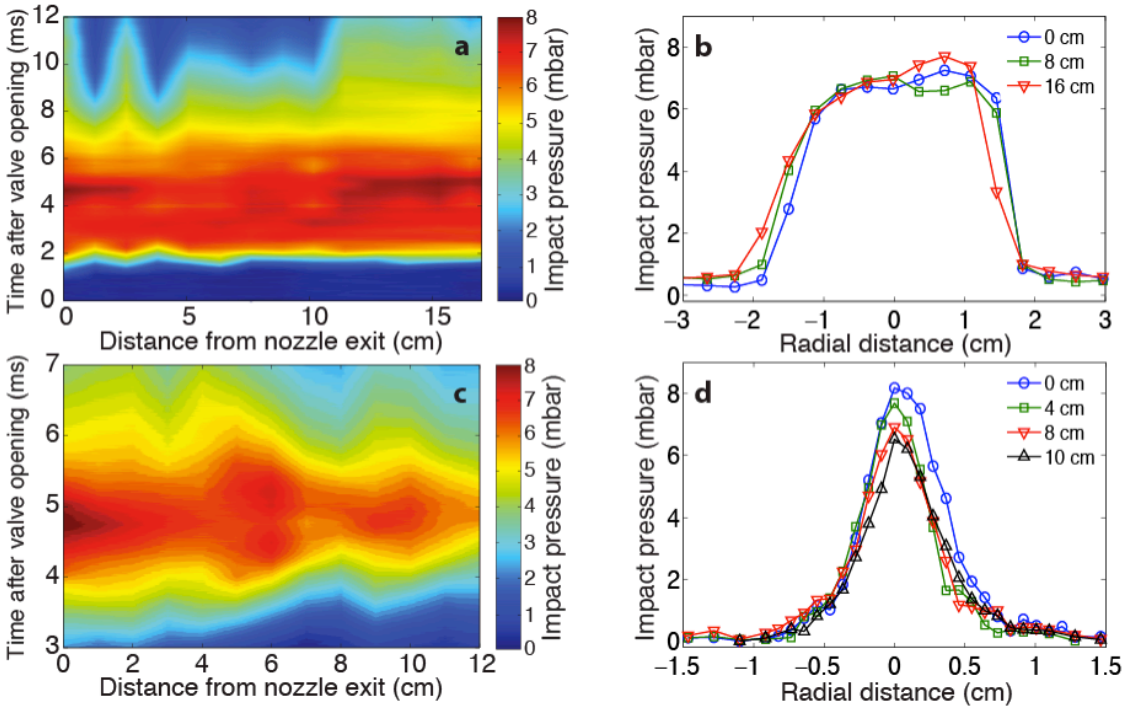

Figure 2.5. (a and c) The impact pressure profiles of Ar and He Laval nozzles, with exit diameters of 55 and 20 mm, respectively, are shown for times up to 12 and 7 ms after the valve is opened, with uniform flow maximum distances of 17 and 12 cm, respectively. (b and d) Radial profiles of the Ar and He flows for several distances between 0 and 16 cm and 0 and 8 cm, respectively, with nearly uniform isentropic core diameters of ~ 3 and ~1 cm, respectively (P_i > 7 bar).

One feature of the pulsed Laval technique that differentiates it from other pulsed supersonic expansion methods is its temperature stability along the propagation axis. Assuming that the flow is isentropic, the Mach number M can be estimated from the Rayleigh formula:

$$\frac{P_i}{P_0} = \left[\frac{(\gamma+1)M^2}{(\gamma-1)M^2+2}\right]^{\frac{\gamma}{(\gamma-1)}} \left[\frac{(\gamma+1)}{(2\gamma M^2-\gamma+1)}\right]^{\frac{1}{(\gamma-1)}} \qquad (2.1)$$

where P_0 and P_i are respectively the reservoir pressure and the impact pressure, and $\gamma = C_p/C_v$ is the ratio of specific heat capacities. With a stagnation chamber held at room temperature, the flow temperature (T_f) and pressure (P_f) are then calculated via

$$\frac{T_0}{T_f} = 1 + \frac{\gamma - 1}{2} M^2 \quad (2.2)$$

and

$$\frac{P_0}{P_f} = \left(\frac{T_0}{T_f}\right)^{\frac{\gamma}{(1-\gamma)}} \quad (2.3)$$

Hence, the Mach number measurements using the isentropic hypothesis allow verification that the experimental flow conditions are in good agreement with the predicted ones, i.e. when a consistent match is achieved for the flow and static chamber pressures. *Once these conditions are reached, one can determine the temperature, pressure, and density at any point of the flow*.

The temperature profiles of the argon and helium beams determined by this method are presented in Figure 2.6. For argon, the temperature shows little variation out to 18 cm, with an average value of T = 26 ± 1 K. For helium, the fluctuations observed in Figure 2.5 are also apparent, but still are quite modest: although the temperature at the nozzle reaches a maximum of ~ 24 K, the temperature stabilizes to ~ 22 K at a distance of 2 cm from the nozzle exit. Notably, at distances between 3 and 7 cm, where the uniform flow is typically probed by the microwave spectrometer, there is less than a ±1 K

variation in temperature. Beyond 10 cm (not shown), a significant and rapid decrease of the impact pressure is observed. The temperatures and densities obtained from these measurements are given in Table 2.2, and show excellent agreement with the design parameters of both nozzles.

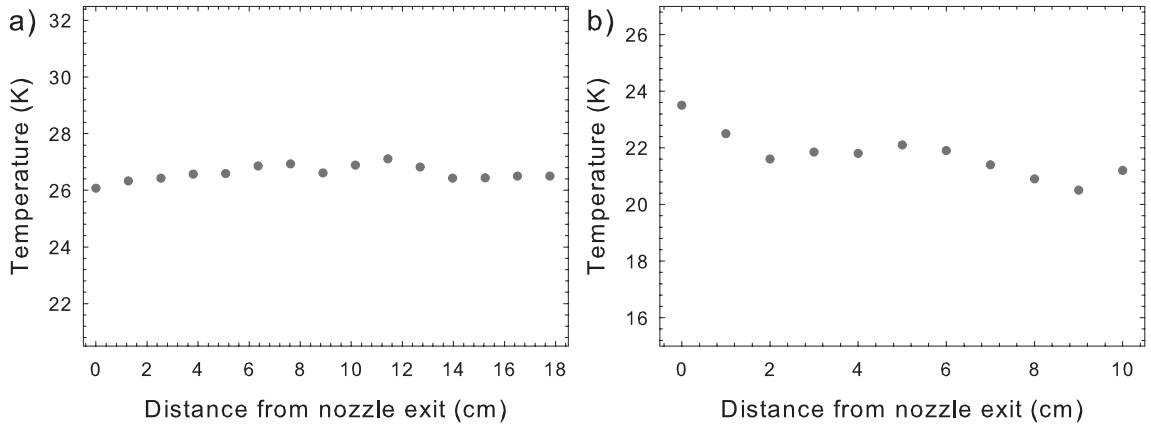

Figure 2.6. a) The argon flow temperature calculated from Pitot tube pressure measurements measured at different linear distances. The temperature (T = 27±1 K) shows very little variation out to distances of 18 cm. b) Pitot measurements of the helium flow indicate a temperature of around T = 22±2 K for distances out to 10 cm. The initial temperature "spike" (T = 23.5 K) at the nozzle exit may be due to turbulence. At distances between 3 and 6 cm, where the microwave transmitting and receiving horns are usually located, the variation in temperature is <1 K.

B. Rotational Temperature

We note that the impact pressure analysis above assumes that the gas in the settling chamber is at room temperature. That this is a valid assumption despite the initial expansion into the chamber is demonstrated in the rotational spectra for the helium case in the following paragraphs. We have not been able to obtain similar spectra in argon and

there are several possible reasons for this. Clustering in argon is a much greater problem than in helium owing to a "chaperone" effect involving dimers. In addition, argon has a much lower thermal conductivity, so that the cooling that accompanies the initial expansion may persist. In this case our impact pressure measurement might significantly overestimate the flow temperature for argon. We plan future experiments with a temperature-variable reservoir to investigate this.

The pure rotational spectra of dimethyl ether, CH_3OCH_3, and acetaldehyde, CH_3CHO, were recorded over the 34-40 GHz range and used to assess the rotational temperature of the helium flow using a Boltzmann analysis. Both molecules are closed-shell asymmetric tops containing either one or two methyl rotors, which cause each $J'(K_a', K_c')$ $J''(K_a'', K_c'')$ rotational transition to split into multiple components. For acetaldehyde, the methyl rotation results in fully-resolvable doublets, denoted A and E. Thus, the analysis for acetaldehyde was based on 12 distinct spectral lines. Dimethyl ether, however, contains two methyl rotors, which produce quartets of blended or partially-blended lines (AA, EE, AE, and EA). Therefore, although 15 spectral features due to CH_3OCH_3 were recorded, lines belonging to the same $J'(K_a', K_c')$ $J''(K_a'', K_c'')$ transition were collapsed and the center frequency taken as the average frequency of the quartet and the total line intensity as the sum of the individual intensities.

The Boltzmann plots were constructed using the following relationship between the integrated line intensities (W) and corresponding lower state energies (E_l):

$$W = \frac{4\pi^{3/2}\omega_0^2 S\mu_i^2 g_l g_I \varepsilon}{c\sqrt{\alpha}} \frac{N_{tot}}{kTQ_{rot}} e^{-E_l/kT_{rot}} \quad (2.4)$$

with k the Boltzmann constant, ω_0 the transition frequency, α the sweep rate and N_{tot}, Q_{rot}, and T_{rot} the column density, partition function, and rotational temperature, respectively. The quantities S, μ_i, and g_I, represent the line strength, dipole moment, and nuclear spin weight. If the logarithm of both sides of Eq. (2.4) is taken and the expression rearranged, then a plot of $\ln(c\sqrt{\alpha}W/4\pi^{3/2}\omega_0^2 S\mu_i^2 g_I g_l \varepsilon)$ vs. E_l/k yields a line, the slope of which is the inverse of the rotational temperature, with an intercept of $\ln(N_{tot}/kTQ_{rot})$.

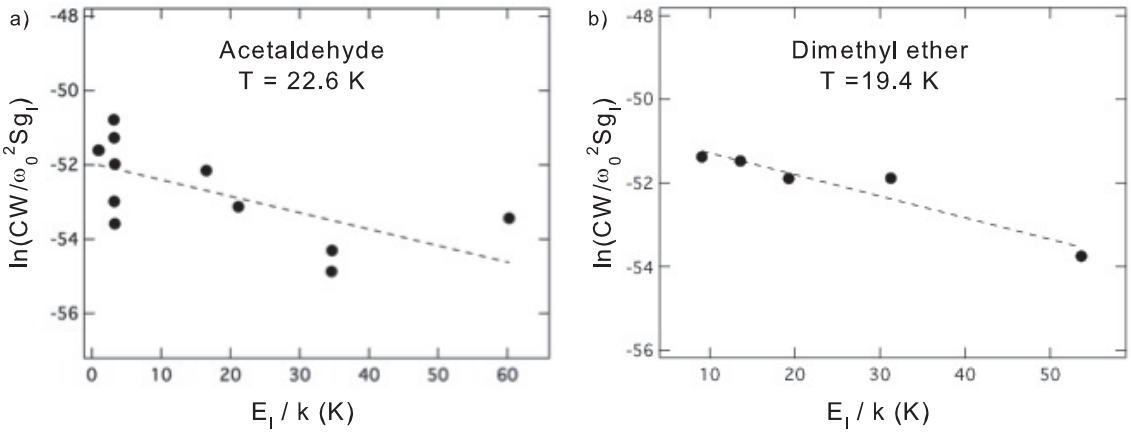

Figure 2.7. Boltzmann plots for acetaldehyde (a) and dimethyl ether (b) in the helium flow. A linear least squares regression (1s) yields rotational temperatures of T_{rot} = 22.6±7 and 19.4±3 K, respectively. To simplify the y-axis label, C is used to represent the constants in Eq. 4.

Figure 2.7 shows Boltzmann plots of CH_3CHO and CH_3OCH_3, based on spectra measured ~4 cm downstream from the nozzle exit. The integrated line intensities were taken as the areas of the peaks, as determined from the Igor Pro (WaveMetrics, Inc., Lake Oswego, OR, USA) multipeak fitting package. The values for S, μ_i, and g_I were taken from the literature.[37,35] From the least-squares fit of these data, temperatures of 19.4±3 and 22.6±7 K were derived for acetaldehyde and dimethyl ether, respectively, in good agreement with the impact pressure measurements.

2.5 Conclusions

The objective of the presented pulsed uniform supersonic flow system was to obtain a collimated, high-density molecular flow at constant temperatures approaching 20 K and with hydrodynamic times of several hundreds of microseconds. We have demonstrated here, both by impact pressure and spectroscopic measurements, that these goals were achieved by using a dedicated high-throughput valve based on a piezoelectric stack actuator with only moderate pumping requirements. This design provides a versatile approach well suited for use with any detection technique. In Chapter 4 this new flow chamber will be combined with CP-FTMW spectroscopic technique to investigate chemical dynamics studies of photolysis and bimolecular reactions.

Table 2.2. Mach numbers, M, target pressures, P_0 and P_f, temperatures, T, and densities, n, of the uniform flows estimated by the flow simulations for the Ar and He Laval nozzles. T_m and n_m are the corresponding values deduced from the impact pressure measurements.

M	Gas	P_0 (mbar)	P_f (mbar)	T (K)	n (10^{16} molecule cm^{-3})	T_m (K)	n_m (10^{16} molecule cm^{-3})	uniform distance (cm)
5.47	Ar	76.5	0.190	26.6	5.23	26 ± 1	4.84	20
5.45	He	69.4	0.183	27.0	4.72	22 ± 2	3.78	10

CHAPTER 3

Chirped-pulse Microwave Spectroscopy

In quantum mechanics, the state of a molecule can be fully described by one complex wavefunction. This total wavefunction can be divided into several components by invoking the Born-Oppenheimer approximation, enabling the individual electronic, vibrational, rotational and nuclear wavefunctions to be considered separately. The chapter will briefly discuss the fundamentals of rotational spectroscopy, and move on to introduce the new chirped pulse detection technique and its potential in the study of reaction dynamics.

3.1 Fundamentals of Rotational Spectroscopy

3.1.1 The Rigid Rotor

The rigid rotor model is used to derive the molecular rotational energy levels for a closed-shell (no unpaired electrons) diatomic molecule. The model assumes that a rigid massless bar connects the two atoms together and rotates perpendicular to its axis. From classical mechanics, the energy of rotation is derived to be $E_{rot} = I\omega^2$, where I is the moment of inertia and ω is the angular velocity. The moment of inertia, I, depends on the mass of the molecule or the mass distribution with respect to mutually perpendicular axes, designated as the principal axes. Therefore, it can be expressed as

$I=\mu R^2$, where μ is the reduced mass of the diatomic molecule and R is fixed distance, generally considered to be the bond length.

From the quantum mechanical aspect, the time-independent Schrodinger equation for a rigid rotor can be written as

$$\frac{J^2}{2\mu R^2}\Psi = E\Psi \quad (3.1)$$

Where J is the rotational angular momentum operator, Ψ is the eigenfunction for rotation (spherical harmonics, $Y_{JM}(\theta,\varphi)$) and E the resultant eigenvalue, which is the rotational energy. Solutions for equation 3.1 are

$$\frac{J^2}{2\mu R^2}Y_{JM}(\theta,\varphi) = \frac{\hbar^2}{2I}J(J+1)Y_{JM}(\theta,\varphi) \quad (3.2)$$

The rotational energy levels for diatomic and linear molecules, can be described via the resultant eigenvalue,

$$E(J) = \frac{\hbar^2}{2I}J(J+1) \quad (3.3)$$

J is considered as the rotational quantum number and the quantity $\frac{\hbar^2}{2I}$ is the molecular rotational constant, B.

The direct relationship between the molecular rotational constant *B* with bond length (R) makes rotational spectroscopy a powerful tool for structure determination. The B value of a molecule can be determined experimentally by measuring the rotational transition frequencies (ν, usually given in units of frequency). The transition frequencies of a closed shell molecule without any nuclear spin is the energy between two sequential rotational levels, or $\nu = 2B(J+1)$. Therefore, as shown is figure 3.1, the

consecutive rotational lines are separated by exactly 2B in frequency space with the energy separations of 2B, 6B, 12B, etc.

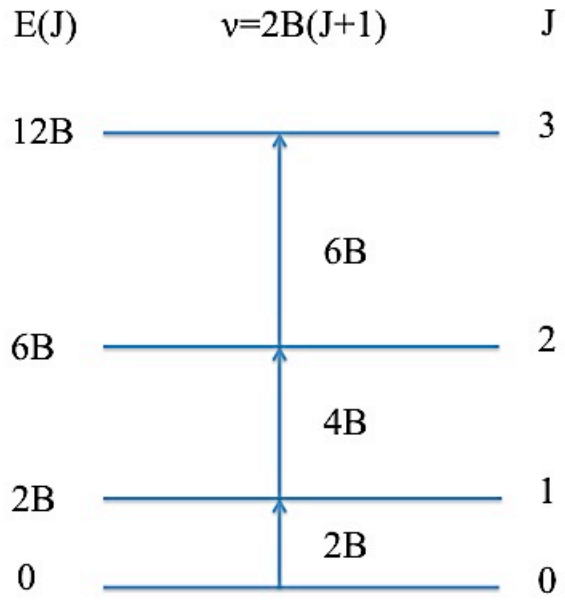

Figure 3.1. Rotational energy level diagram for a closed shell (S = 0) diatomic

3.1.2 Non-Rigid Rotor

In reality, a rigid massless bar does not connect the atoms. Therefore, the bond length slightly increases as the molecule rotates faster and J increases. In order to account for this non-rigid behavior, the rigid rotor energy expressed in Equation 3.3 has to be corrected via a power series expansion. The resultant expression of the rotational energy level expression for a non-rigid rotor is shown below

$$E(J) = BJ(J+1) - DJ^2(J+1)^2 + HJ^3(J+1)^3 + LJ^4(J+1)^3 + MJ^5(J+1)^5 + \ldots \quad (3.4)$$

Where D, H, L and M are all centrifugal distortion constants.

As a consequence of centrifugal distortion effects, the energy separation between two atoms can no longer be approximated as 2*B*. As the molecule rotates faster the bond length increases and the rotational transitions are shifted slightly to lower frequencies. This is well observed through the deviations of the rigid rotor predictions versus the non-rigid rotor predictions and these are magnified with higher *J* values. However, the rotational transition frequencies for the non-rigid rotors can be reliably predicted through the expression:

$$\nu = 2B(J + 1) - 4D(J +1)^3 + \ldots \quad (3.5)$$

The value of *B* depends on the structure, electronic and vibrational state of the molecule. Most pure rotational spectra of molecules are recorded in their ground electronic and vibrational state. However, if the cooling is not efficient some population can be in the excited vibrational state and rotational transitions can be observed within that state. A diatomic molecule has only one vibrational mode; therefore the rotational constant is expected to decrease as the vibrational quantum number increases. The rotational constant of a specific vibrational level can be expressed as B_v, and its vibrational dependence can be expressed as

$$B_v = B_e - \alpha_e(v + 1/2) + \gamma_e(v + 1/2)^2 + \ldots.. \quad (3.6)$$

where α_e and γ_e are the rotational-vibrational expansion constants and B_e is the equilibrium rotational constant, which can be used to determine the equllibrium bond length.

3.1.3 Interactions of Angular Momenta

So far all the derivations were done for closed-shell diatomic/linear molecules in the ground vibrational state of the ground electronic state. The presence of any intramolecular/intermolecular interactions or external fields were neglected. However, in reality many molecules are open-shell (radicals) and are under the influence of numerous magnetic moments, magnetic fields and electric fields, causing complex perturbations and splittings compared to the simple non-rigid rotor rotational energy level. In Figure 3.2 an illustration of various magnetic momenta coupling schemes are shown. **L** is the orbital magnetic moment, **R** is the rotational magnetic moment due to molecular end-over-end rotation, **S** is the spin magnetic moment (due to unpaired electron(s)), and **I** is the nuclear spin magenetic moment (due to nuclei with $I > 0$). L and S are determined through the summation of l and s of the unpaired electron(s), where s = ½ for one electron and l is dependent on the orbital in which the electron resides.

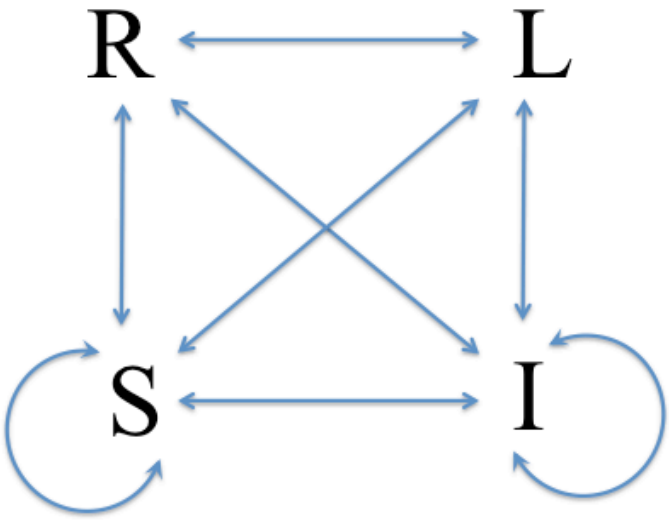

Figure 3.2. Representation of the eight possible magnetic coupling interactions of angular momenta.

The Bohr (electron) magneton is much larger than the nuclear magneton, therefore any coupling involving the electron is expected to be larger. The relative magnitudes of the rotational and nuclear spin angular momenta depends on the rotational contant and the nuclear magnetic moment. Any coupling involving the magnetic moment of the electron is termed as fine structure, while the coupling with nuclear magnetic moment is known as hyperfine stucture.

Table 3.1. Possible Magnetic Angular Momenta Coupling Schemes

Angular Momenta Interactions	**Type of Coupling**
L·**S**	Spin-Orbit
R·**S**	Spin-Rotation
S·**S**	Spin-Spin
I·**S**	Nuclear Spin-Electron Spin (Fermi-contact, Dipolar)
I·**I**	Nuclear Spin-Nuclear Spin
I·**R**	Nuclear Spin-Rotation
I·**L**	Nuclear Spin-Orbit
R·**L**	Lambda Doubling

In addition to the above magnetic angular momenta coupling, the electric hyperfine effects must also be considered. The most common of these is nuclear quadrupole coupling where the quadrupole moment of a nucleus (in cases where $I>1/2$) interacts with an external electric field. This interaction is most apparent at lower rotational levels.

In conclusion, all these potential interactions and coupling will not only perturb and split the rotational energy levels making it more difficult to identify the rotational fingerprint, but also significantly reduce the experimental signal level. Therefore, even

for a simple diatomic molecule much effort has to be taken to to measure , identify and characterize

3.1.4 Classification of molecular rotors

Molecules can be categorized into classes of molecular rotors according to their geometric structures. These structures give rise to unique and beautiful patterns in the rotational spectrum of a given molecule, so if the class is known, the spectrum can be more easily and efficiently identified. In quantum mechanics, the free rotation of the molecule and is quantized, where the rotational energy and its angular momentum are held constant. These are related to the moment of inertia I of the molecule. A molecule will have three moments of inertia termed I_A, I_B and I_C along the three mutually orthogonal axes A, B and C (in the molecular frame) with its origin located at the center of mass of the molecule. Thus, for convenience the molecules are divided in to four different classes based on their relative moments of inertia.

a) **Spherical tops**: $I_A = I_B = I_C$. These molecules generally do not have a permanent dipole moment and thus do not produce pure rotational spectra.

   Example: P_4, CCl_4, CH_4, SF_6

b) **Linear molecules**: $I_A << I_B = I_C$; I_A can be considered as zero. These molecules belong to the $C_{\infty v}$ and $D_{\infty h}$ point groups. Only those in the $C_{\infty v}$ group exhibit pure rotational spectra

   Example: OCS, HCN, and HCCCN

c) **Symmetric Top:** Two equal moments of inertia; three-fold or higher order rotational axis; given in one of two limits

I. **Oblate:** $I_A = I_B < I_C$ saucer or disc-shaped

Example: NH_3, BCl_3, CH_3O

II. **Prolate:** $I_A < I_B = I_C$ rugby football, or cigar shaped

Example: CH_3Cl, CH_3CCH

d) **Asymmetric top:** $I_A \neq I_B \neq I_C$, maximum 2 fold rotational axis.

Example: H_2O, C_2H_3CN

Asymmetric tops are the most common type, and have three mutually orthogonal axes with three different moments of inertia ($I_A < I_B < I_C$). These are typically classified in either the near prolate ($I_A < I_B = I_C$) or near oblate ($I_A = I_B < I_C$) limit of a symmetric top. For symmetric tops, K is the projection of J on the molecular axis, producing two degenerate K components (for K > 0). Figure 3.3 shows a typical asymmetric top rotational energy level diagram for the J = 0, 1, and 2 energy levels. Quantum numbers used to classify asymmetric top energy levels are J_{KaKc}, where J is the total rotational angular momentum. It should be noted that the K quantum number itself is not a "good" quantum number for asymmetric tops, although K_a and K_c are used to indicate the prolate and oblate symmetric top limits, respectively. Asymmetric tops have three unique rotational axes (a, b, and c), and therefore could have three corresponding electric dipole moments: μ_a, μ_b, and μ_c. Each dipole moment corresponds to a different spectroscopic pattern whose allowed transitions follow a certain set of selection rules. The selection rules for *a*-type, *b*-type and *c*-type transitions are as follows: $\Delta J = 0, \pm 1$, $\Delta K_a = 0$ and $\Delta K_c = \pm 1$; $\Delta J = 0, \pm 1$, $\Delta K_a = \pm 1$ and $\Delta K_c = \pm 1$; and $\Delta J = 0, \pm 1$, $\Delta K_a = \pm 1$ and $\Delta K_c = 0$, respectively.

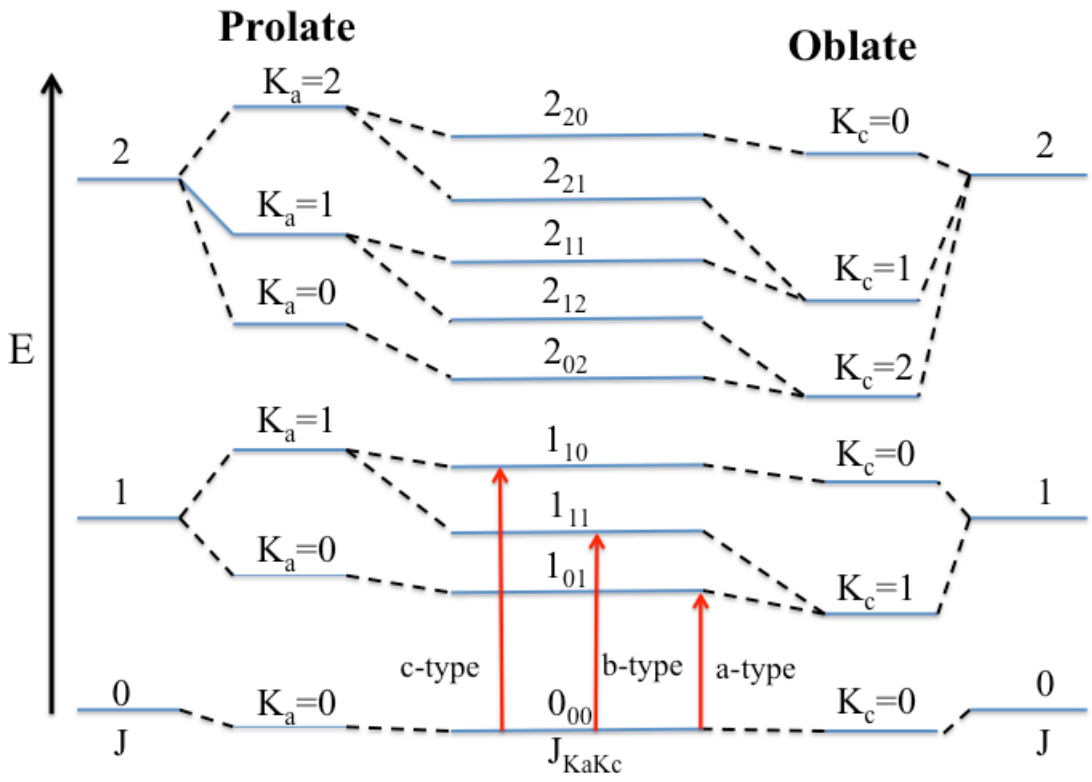

Figure 3.3. Energy level diagram for an asymmetric top. Depending on the electric dipole moments, *a*-type, *b*-type, and/or *c*-type transitions are expected, indicated by the red arrows.

3.2 Chirped pulsed Fourier-Transform micro/millimeter wave spectroscopy

Chirped-pulse Fourier transform microwave (CP-FTMW) spectroscopy, initiated by Brooks Pate and coworkers, is a transformative microwave spectroscopy technique, enabling us to cover a broad spectral region (~10 GHz) in a single chirped pulse with high resolution (~100 kHz) and meaningful relative transition intensities. With its extremely high spectral resolution and the sensitivity of the rotational constants to molecular structure, rotational spectroscopy has the exceptional ability and precision to determine the structures of molecules and radicals. The conventional Balle-Flygare

Fourier transform microwave spectrometer is the most widely used pre-chirped pulse microwave spectrometer. It is essentially a narrow bandwidth instrument, though. The high-Q cavity allows it to achieve the maximal sensitivity, but with the drawback of having to mechanically adjust the cavity in order to maintain the full augmentation of the microwave field while scanning successive spectral intervals of ~1 MHz or less.

CP spectroscopy gives us the ability to retain many of advantages of the traditional narrow-band microwave spectrometer and to definitively assign rotational transitions in molecules and radicals. This allows one to differentiate conformers, identify vibrational states and resolve fine and hyperfine structure while adding broadband capability and reducing acquisition time, making it a ground-breaking tool for physical chemists. This increased *spectral velocity* which we define as number of resolution elements acquired per unit time also has the advantage of reducing sample consumption, and the shot-wise broadband scanning allows for reliable comparisons of line intensities for quantitative studies. These features have been demonstrated through the measurement of the pure rotational spectra of several complex organic molecules, with the goal of obtaining detailed structural information,[40] investigating tunneling and other intramolecular interactions concerning internal rotation,[41–43] or generating data for astrophysical searches,[44] for example. The flexibility of the chirped-pulse (CP) approach has further been enhanced by the extension of its frequency range to the millimeter, submillimeter, and terahertz wavelength regions, and in the implementation of novel data acquisition strategies.[45–47]

3.2.1 Instrumentation

The CP spectrometer consists of three main sections (Figure 3.4). The linear frequency sweep chirp is created at the chirp generation region. The created chirp interacts with the sample at the interaction region and excites all the molecular rotational transition available in the selected frequency range. Finally in the detection region collects the emitted molecular free induction decay (FID) is collected and Fourier transformed it into frequency space to obtain the pure rotational spectrum. Further technical details of these three regions are shown in Figure 3.3 and discussed below.

1. Chirp Generation Region

The main requirement in performing broadband microwave spectroscopy is a source that can produce phase-reproducible linear frequency sweeps over a broad (<10 GHz) frequency region. The sweep durations have to be long enough to polarize the sample molecule but also shorter than the dephasing of the rotational FID. In general, 1 μs pulse duration is chosen for both microwave and millimeter wave spectrometers. The high phase stability of the microwave source is need for the collected molecular FIDs to be averaged in the time domain. Therefore, all the frequency components are phase locked to a 10 MHz Rb oscillator. This ensures that all waves start with the same relative phase in each measurement event. An arbitrary wave generator (AWG), also phase locked to the Rb reference, is used to create the frequency pulse. Due to the limited frequency range of the AWG the chirp must be upconverted to the frequency range of interest. To do so, the AWG signal is mixed through a broadband mixer with the output of a single-frequency local oscillator, externally locked to the Rb standard. As the mixing produces two

sidebands ($\nu_{AWG} \pm \nu_{LO}$), a bandpass filter is used to reject the undesired sideband so that only frequencies of interest are injected into the multiplication circuit. The multiplication circuit consists of a combination of active and/or passive multipliers which upconvert the mixer output and expands the bandwidth to reach the final target frequency and bandwidth. The final frequency is amplified and broadcast to the sample interaction region.

2. Sample Interaction Region

The interaction region of the spectrometer is generally located within a vacuum chamber, with the sample introduced via a pulsed valve. However, static gas chambers can also be used. In pulsed systems, usually a dilute mixture (<5%) of precursor in He, Ar, or Ne is used at nozzle backing pressures around 1 atm. In many cases, high-voltage discharge or laser ablation sources are used to promote reactions or generate radicals. The high-power polarizing pulse is broadcast into the sample using a standard gain horn. The pulse excites all the pure rotational transition of the respective sample within the frequency range. A second gain horn collects the emitted molecular free induction decay and transmits it to the detection region.

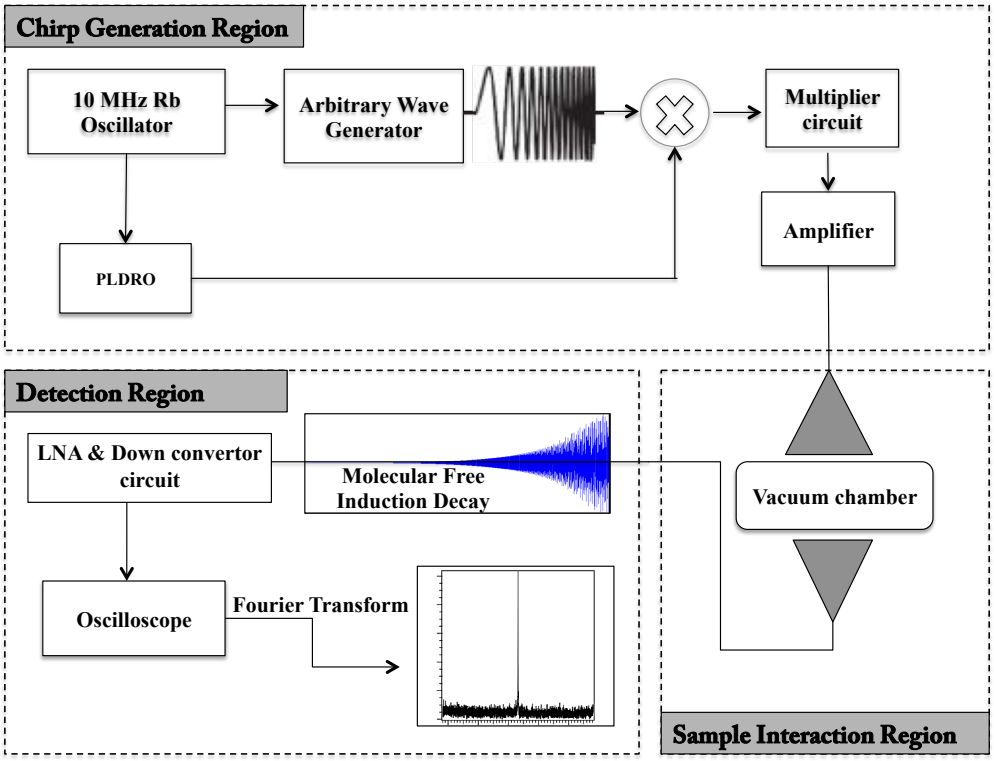

Figure 3.4. Basic componnets of a chirped pulse Fourier transfrom microwave spectrometer

3. Detection Region

Following the sample polarization by the chirped pulse, the emitted broadband molecular emission, or FID, is collected. A low noise amplifier (LNA) is used to amplify the weak molecular FID so that an oscilloscope or digitizer can read it. If a high-power amplifier was used in the upconversion circuit, a combination of a diode and switch are used to protect the LNA; the same TTL pulse as the high-power amplifier triggers the switch. If the oscilloscope used to digitize the broadband FID does not have sufficient bandwidth, the upconverted pulse must be downconverted to match the maximum bandwidth of the oscilloscope. A LO phased locked to the Rb clock is used for the downconversion and mixed with the amplified FID. The downconverted FID signal

passes through a low pass filter that removes spurious local oscillator signals that leak through the mixer and a dc block to remove 1/*f* noise prior to digitization. The signal is digitized and multiple FIDs can be averaged in the time domain. A Fourier transform converts the signal to the frequency domain, producing a pure rotational spectrum of the sample.

3.3 Application to reaction dynamics

The combination of detailed structural information that rotational spectroscopy affords, along with efficient signal acquisition spanning a broad spectral bandwidth, suggests that CP-FTMW offers compelling advantages for the study of reaction dynamics of polyatomic molecules. Indeed, Pate and co-workers have demonstrated that the broadband feature of CP-FTMW spectroscopy can be used to measure the rates of isomerization in laser-excited molecules,[48] and more recently CP-FTMW/mmW has recently been used to probe the products generated from pyrolysis and photolysis reactions.[49,50] Rotational spectroscopy techniques have been used for reaction dynamics and kinetics studies in the past,[51–53] but have not been widely adopted. Traditional techniques, such as laser-induced fluorescence (LIF) or resonant multiphoton ionization (REMPI) methods, are still the preferred approaches for investigating reaction dynamics with extraordinary sensitivity. CP microwave methods, with the broadband advantage and spectral velocity as defined above, represent a tremendous advance, now making it possible to bring the structural specificity of rotational spectroscopy to bear on studies of reaction dynamics and kinetics. This advantage promises a new richness of detail for

investigating the dynamics of polyatomic reactions. For large molecules, quantum-state specific REMPI and LIF schemes are largely unavailable. Non-resonant methods give ambiguous product identification because they produce broad, unstructured spectra. Product isomeric composition is undetermined, and branching ratios are rarely obtained accurately. Thus, one is unable to directly infer isomer- and vibrational level specific information or branching. Synchrotron photoionization has emerged in recent years as a powerful isomer-selective detection strategy that has broad applicability, but it lacks detailed structural information and is only available at synchrotron facilities with somewhat limited access.[54,55] In contrast, rotational spectroscopy can be used to differentiate between isomers, conformers, isotopologues, and vibrational states, even in mixtures. Moreover, the broadband detection scheme readily allows for comparison of relative line intensities of different species to provide accurate branching ratios if the products have a well-defined rotational temperature.[49] In a recent CP study, a signature of roaming dynamics was observed by quantifying branching into several reaction products aided by accurate kinetic modeling.[56]Therefore, it is clear that CP-FTMW spectroscopy has the unique potential to probe intimate details of reaction dynamics.

CHAPTER 4

Chirped Pulse Uniform Flow Spectrometer

4.1 Introduction

To exploit the full potential of CP-FTMW, a cold sample producing sufficiently large population differences for a sensitive spectroscopic detection is required. Molecular sources generally used for CP-FTMW/mmW instruments are based on pulsed free jets based, which provide rotationally cold samples when the gas is expanded into the vacuum chamber. However, as previously discussed, these sources offer non-uniform environments where densities and temperatures can vary over several orders of magnitude throughout the flow. The typical total sample volume that may be interrogated is limited to a few cm^3 at *product* number densities of perhaps 10^{10} cm^{-3}. Moreover, the conditions in free jet expansions do not permit reactions or photochemistry to take place with the necessary rotational cooling under well-defined conditions. To overcome these challenges and provide uniform, well-defined flow conditions at low temperature and high density appropriate for reaction dynamics studies, we have chosen to couple the revolutionary CP-FTMW technique to our novel pulsed uniform supersonic flow system. In contrast to the free jet expansion, these flows can produce large volumes (10 – 100 cm^3) of rotationally thermalized samples at temperatures of 20 K and product densities $>10^{14}$ cm^{-3}, which is ideal for CP-FTMW based detection. The flow system has been discussed detail in Chapter 2 and is integrated into a new CP-FTMW spectrometer

operating in the K_a-band (26 – 40 GHz).[57] We term this combination a Chirped-Pulse-Uniform Flow (CPUF) spectrometer. The system is also used with a mm-Wave spectrometer (60-90 GHz) that is based one developed in the Field group[8,11] but its performance is demonstrated in Chapter 5.

In this chapter a detailed description of the new approach is provided. The K_a-band spectrometer is presented and examples illustrating the new instrument's performance and capabilities are shown. In the first example, the 193 nm photofragmentation of SO_2, yielding SO ($X\ ^3S^-$), demonstrates how the combined system can be used to study photochemistry, detect product vibrational distributions, and track rotational and vibrational relaxation accompanying photochemical processes. The second example shows that bimolecular reaction products produced in the uniform flow can be easily detected with this new method. A discussion of implications and prospects for this new technique is also provided.

4.2 Experimental setup and instrumentation

The new spectrometer consists of two main components as shown in Figure 4.1: a K_a band (26 – 40 GHz)[57] chirped-pulse Fourier-transform microwave setup and a Pulsed Uniform Flow (PUF) system described in detail in Chapter 2, which is capable of producing a high density (~10^{17} cm^{-3}) and large volume of cold (20 – 30 K) molecules.

The CP-FTMW spectrometer consists of an 8 giga-samples/s arbitrary waveform generator (AWG; Tektronix AWG7082C) that produces microwave chirps having a linear frequency sweep up to 4 GHz in ≤ 1 ms. The AWG pulse is upconverted in a broadband mixer (Marki M10418LC) with a phase-locked dielectric resonator oscillator

(PDRO) operating at 8.125 GHz, and the mixer output is amplified by a broadband amplifier (ALC Microwave ALS030283). The frequency band is selected through a bandpass filter and propagated through a combination of active (Marki ADA8512K) and passive (Marki D0840L) frequency doublers to quadruple the linear sweep bandwidth in two stages. The final microwave pulse is amplified using a traveling wave tube (TWT; Applied System Engineering Inc. 187Ka) amplifier to obtain a peak power of 40 W. The pulse is directed through the PUF via a feedhorn mounted outside of the polycarbonate flow chamber and perpendicular to the flow, polarizing the molecules, which then undergo free induction decay (FID). The FID signal is collected with a second feedhorn and passed through a fast switch (Millitech PSH-28-SIAN0) that protects the low noise amplifier (LNA; Miteq JSDWK32) from the high-power microwave pulse. The LNA amplifies the weak FID signal, and the output is downconverted by a broadband mixer (Millitech MXP-28-RFSSL) with a PDRO operating at 16.75GHz, multiplied with an active doubler (Marki ADA1020). The mixer output is sent to a digital oscilloscope (Tektronix DPO70804C) with a 25 giga-samples/s digitization rate and hardware bandwidths up to 8 GHz, where the FIDs from successive polarizing pulses are phase coherently averaged in the time domain, then fast-Fourier-transformed using a Kaiser-Bessel window function to obtain a frequency-domain spectrum. Both PDROs and the AWG are phase locked to a 10 MHz reference from a Rb-disciplined master clock (Stanford Research System FS725) to permit coherent averaging of the FID in the time domain. To reduce the phase drift of the oscillators, the PDROs and mixers are water cooled to 15 $^{\circ}$C.

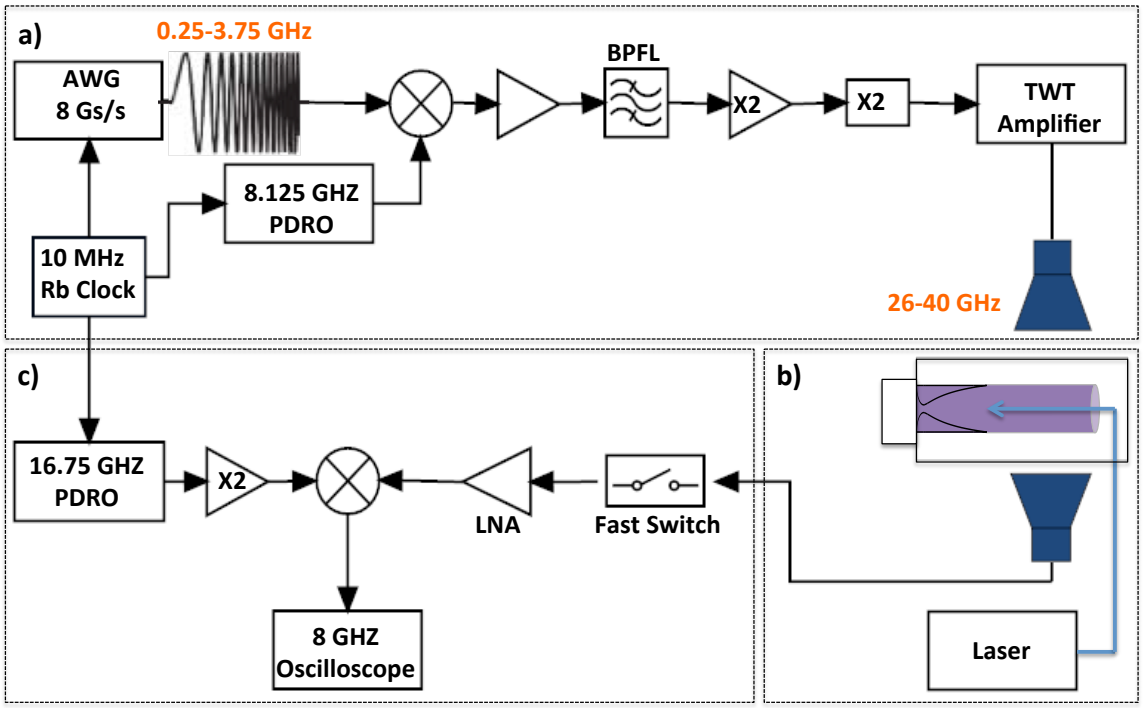

Figure 4.1. The CPUF setup is illustrated in three parts: a) Chirped pulses (0.25 – 3.75 GHz) are produced in an arbitrary waveform generator (AWG) and then mixed with a LO frequency (8.125 GHz) locked to a 10 MHz Rb standard. The resulting frequencies are then multiplied (4x) via a series of active and passive doublers before further amplification by a 40 W traveling wavetube amplifier (TWTA). The microwave radiation is then broadcast through the molecular sample via a feedhorn oriented perpendicular to the molecular axis. Bandpass filters and isolators are inserted into the setup as necessary. b) A piezoelectric stack valve and Laval nozzle are mounted on one end of a polycarbonate vacuum chamber.[57] A quartz window is located on the other end of the chamber to allow radiation from an excimer laser to propagate down the axis of the Laval nozzle, such that the core of the flow is irradiated. c) Molecular emission in the form of free induction decay (FID) is collected by second feedhorn. This signal is downconverted before detection and phase coherently averaged in an oscilloscope, where it is fast Fourier-transformed to produce a frequency-domain spectrum.

The vacuum chamber was constructed from a transparent polycarbonate tube (K-Mac Plastics) with inner diameter, length, and wall thickness of 24, 90, and 1 cm, respectively. This material minimizes reflections from the microwave radiation, decreasing the possibility of creating standing waves. Two aluminum flanges seal the

transparent tube. The Laval nozzle is mounted on one flange, while the other is attached to the turbomolecular pump assembly. The chamber is mounted onto a translation stage, which enables linear movement of the chamber such that different regions of the flow can be probed without disturbing the microwave and antenna setup.

A quartz window is mounted into the chamber attached to the turbomolecular pump. Through this window, the output from an excimer laser, operating at either 193 or 248 nm (GAM Laser, EX200/60), is directed through the vacuum chamber and down the axis of the flow. The laser beam is loosely focused with a biconvex lens (f = 200 cm) to a width of approximately 5 mm at the throat of the Laval nozzle.

The timing for the experiment is controlled by the AWG, which has two main output (marker) channels. The AWG output is routed through two pulse-delay generators (Berkeley Nucleonics Corp. Model #555 and 575), one of which is used to control the delays between the gas pulse and laser relative to the chirp sequence. The other delay generator sets the timings of the TWT amplification and the fast PIN switch. All timing delays are optimized for the system being studied to ensure that reactions occurring in the flow are studied. Typically we record many chirp-FID sequences in each gas pulse.

4.3 Performance and Application

The newly commissioned CPUF spectrometer was initially tested and benchmarked with OCS to evaluate its overall performance. The CPUF results were comparable to those previously published for a K_a-band CP-FTMW spectrometer.[58] Because the CPUF spectrometer has been developed and designed for the purpose of studying chemical reaction dynamics, some well-known systems were chosen to

demonstrate this new spectrometer's capabilities for that application. These examples illustrate the versatility of this instrument and its utility as a complementary method relative to traditional approaches. We first present signal level estimates, and then provide examples to illustrate the performance.

4.3.1 Estimating Signal Levels

The signal detected by the CP-FTMW spectrometer is the electric field of the FID of the polarized molecules. From the expression derived by McGurk et al.[59] for the polarization resulting from adiabatic fast passage, the measured signal, E_{FID}, is given by:

$$E_{FID} \propto \omega\mu^2 E_{pulse} \Delta N \, (\pi/\alpha)^{1/2},$$

where ω is the frequency, μ the transition dipole moment, E_{pulse} the electric field strength of the pulse, ΔN the population difference, and α the linear sweep rate. The spectral resolution of the collected signal depends only on the duration of the collected FID, not on the excitation pulse duration.

A unique consideration of performing CP microwave spectroscopy in flows is the possible attenuation of line intensities in the spectra due to the impact of collisions; this effect is not a concern under free-jet expansions, as the CP probe is employed in the "collision-free" region in that case. Under the conditions prevailing in our helium flow, P = 0.18 Torr and T = 22 K, we estimate a mean free path of l =30 μm and a collision frequency of roughly 11 MHz, implying a mean time between collisions of ~90 ns, shorter than the typical chirp durations in CPUF. Thus, transitions excited early in the pulse are likely to undergo collisions, possibly attenuating the line intensities, while transitions excited later do not display this loss of signal. Shown in Figure 4.2 are several

dimethyl ether transitions in the frequency region 34 – 40 GHz with 1000 and 250 ns chirps swept either down (black trace) or up (red) in frequency. A clear asymmetry in line intensities is apparent in the 1000 ns spectra, but not in the 250 ns spectra. This effect implies that relative line intensities across the swept bandwidth may not necessarily be reliable for the longer chirp. Some compensation for this effect can be obtained, however, by averaging upchirp and downchirp spectra in the frequency domain (Figure 4.2, second and bottom rows, blue traces). Of course, this asymmetry can be overcome by using a chirp duration shorter than the collision time scale, but at the cost of a significant sacrifice in signal strength.

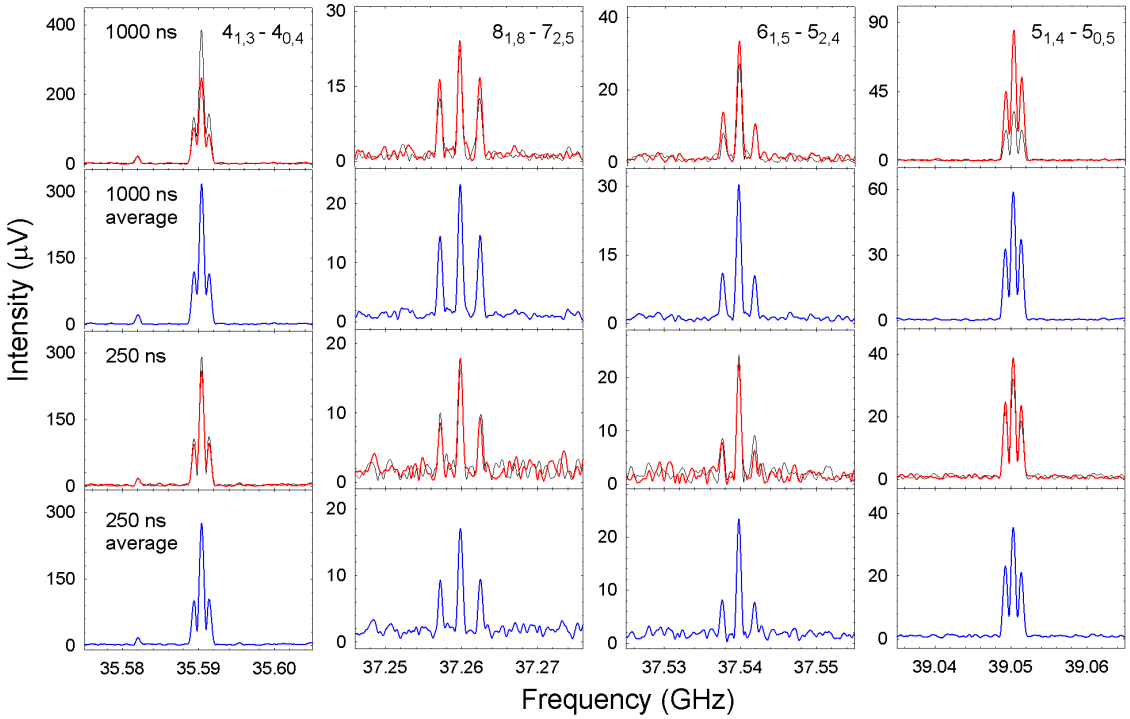

Figure 4.2. Several rotational transitions of dimethyl ether ($J'_{Ka',Kc'} - J''_{Ka'',Kc''}$) over the 34 – 40 GHz frequency range are shown to illustrate the effects of collisional dephasing on signal intensities. The top row of spectra was taken with chirp duration of 1000 ns, and a clear asymmetry exists in the line intensities between up- (red trace) or down-swept (black) frequencies. This asymmetry is less severe in spectra obtained with a 250 ns chirp duration (middle row) or shorter. Averaging up- and down-chirped spectra in can compensate for the dephasing effects, as shown in rows two and four (blue traces) for the 1000 and 250 ns spectra, respectively. Each spectrum is an average of roughly 100000 acquisitions, which took ~5 min of integration time at a pulsed valve repetition rate of 3.3 Hz, with 200 acquisitions collected per gas pulse.

The spectrometer capabilities are illustrated in Figure 4.3 with the closed-shell linear molecule OCS, which has a dipole moment μ = 0.715 D and a rotational constant B = 6081.492 MHz. The spectrum was collected over a 6 GHz frequency range (34 – 40 GHz), with a chirp duration of 1 ms. A sample of 1% OCS in helium was used to

evaluate the sensitivity of the instrument through the detection of the most abundant isotopologue ($^{16}O^{12}C^{32}S$, 93.74%), as well as $OC^{34}S$ (4.158%), $O^{13}CS$ (1.053%) and $OC^{33}S$ (0.740%), with its hyperfine splittings.[58] The signal stability and the signal-to-noise ratio (S/N) were checked by comparing single- and 10000-shot $^{16}O^{12}C^{32}S$ spectra of the J = 3 – 2 rotational transition at 36.488 GHz. This peak showed an increase in S/N by a factor of 85 with a peak intensity of 2.308 mV and line width of 0.6 MHz after 10000 acquisitions. The population difference (ΔN) at 22 K can then be calculated using the partition function of $O^{12}CS$, the sample density (4×10^{14} cm^{-3}), a probe core volume of 5 cm^3 (based on an 8 mm diameter, 10 cm long flow) yielding a rotational level population difference of $\Delta N = 7.6 \times 10^{12}$ molecules in the irradiated volume.

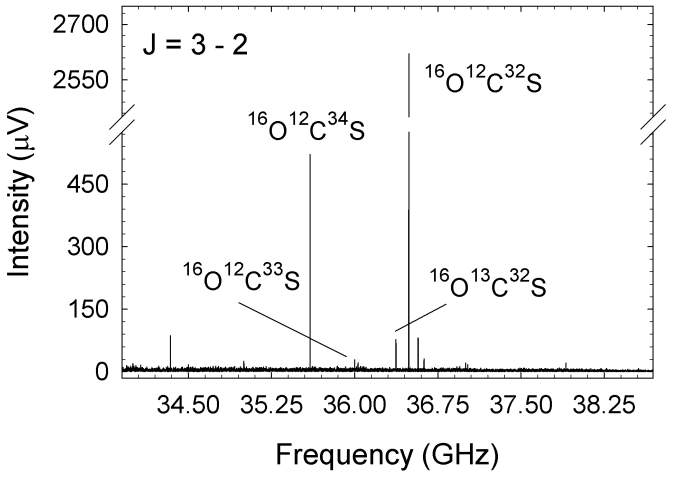

Figure 4.3. A representative broadband spectrum of the isotopologues of OCS ($\tilde{X}\ ^1S^+$) in the J = 3 – 2 transition near 36 GHz is shown. The break in the y-axis allows the full intensity of the main isotopologue, $^{16}O^{12}C^{32}S$, to be shown. The ^{33}S nuclear spin (I = 3/2) splits the weaker $^{16}O^{12}C^{33}S$ line into $2I + 1$ components. The spectrum is an average of ~10000 shots

.

The signal intensity of OCS can be used as a benchmark and basis for comparison to estimate the expected signal levels for photodissociation or bimolecular reactions in the flow. We first estimate these for the reactions we examine below. The flow density of the Laval system with He as the carrier gas is 4×10^{16} cm^{-3}. If the 193 nm photodissociation of SO_2 to yield SO ($X\ ^3\Sigma^-$) is considered, we can estimate ΔN for the product SO as follows. At 193 nm, 10 mJ/pulse corresponds to ~10^{16} photons per pulse. Using the SO_2 absorption cross section (10^{-17} cm^2) and an SO_2 density of 4×10^{14} cm^{-3}, assuming unit quantum yield for dissociation, we produce 4×10^{13} product molecules per cm of path length. For the 10 cm long interaction volume, analogous to OCS, this gives a total of 4×10^{14} molecules in a volume of 5 cm^3, or a density of 8×10^{13} cm^{-3}. Taking into account the Boltzmann factor, we obtain a total population difference $\Delta N = 3 \times 10^{11}$, roughly a factor of twenty smaller than that of OCS. The dipole moment of SO is μ = 1.55 D, so for the $N_J = 1_0 - 0_1$ transition in the $v'' = 0$ vibrational level at 30.001 GHz, a signal level a factor of five lower than that of $O^{12}CS$ can be anticipated. In this case the larger dipole moment and partition function of ~20 compensate for the fraction (~10%) of the molecules undergoing photodissociation. However, one must also account for the relative intensities of the fine structure components when studying open-shell molecules. In the case of SO, the N = 1 – 0 rotational transition splits into three spin components corresponding to the $N_J = 1_0 - 0_1$, $1_2 - 0_1$, and $1_1 - 0_1$ transitions. From the calculated line strengths of each transition, only about 8% of the SO population is expected to be observed in the $N_J = 1_0 - 0_1$, as opposed to 61 and 31% in $N_J = 1_2 - 0_1$ and $1_1 - 0_1$,

respectively. Thus, contributions of all spin components must be considered when calculating the SO signal levels.

For a bimolecular reaction, the product yield can also be estimated as above, with the flow density of 4×10^{16} cm^{-3} at 22 K. For the reaction of the CN radical with acetylene (C_2H_2) to produce cyanoacetylene (HCCCN), 1.5% C_2H_2 and 1% BrCN as a CN precursor were used. The CN concentration can again be estimated using the initial BrCN density of 4×10^{14} cm^{-3} and an absorption cross-section of 10^{-18} cm^2 at 193 nm. Here we use 40 mJ/pulse with 10 cm flow length to give an estimated a total of 1.6×10^{13} CN radicals per cm of path length. Assuming unit reaction efficiency between CN and acetylene, and the 10 cm path length, we estimate that approximately 1.6×10^{14} HCCCN molecules will be produced, corresponding to a density of 3.2×10^{13} cm^{-3}. Given the second order rate constant $k = 4 \times 10^{-10}$ cm^3 $molecules^{-1}s^{-1}$ at 25 K,[60] we anticipate reaction in the flow on a timescale of ~5 μs. The HCCCN product will also react with CN with a rate constant of 1×10^{-10} cm^3 $molecules^{-1}$ s^{-1} at 22 K to give dicyanoacetylene,[60] but simple simulations show that this will not significantly affect the final HCCCN concentration. Considering a dipole moment of $\mu = 3.73$ D for HCCCN and the rotational level population difference $\Delta N = 1.9 \times 10^{12}$ molecules in the irradiated volume, an estimate for the signal level of the J = 4 – 3 rotational transition at 36.392 GHz can be obtained. Thus, the expected signal intensity of HCCCN should be an order of magnitude larger than that of OCS, with the assumed reaction efficiency of 100% is a single product vibrational level were populated.

4.3.2 Photochemistry: SO_2 +hν (193 nm) → O (^3P_J) + SO ($X\,^3\Sigma^-$, v)

The 193 nm photodissociation of SO_2 has been previously studied by several different methods, including velocity map imaging, Fourier-transform infrared spectroscopy, microwave spectroscopy, and laser induced fluorescence spectroscopy.[53,61–66] From those experiments, it was concluded that this reaction occurs via excitation from the ground $\tilde{X}\,^1A_1$ state to the $\tilde{C}\,^1B_2$ state followed by dissociation. However, the $\tilde{C}$ state correlates to singlet fragments, SO ($a\,^1\Delta$) and O (^{1}D), rather than the observed triplets, SO ($X\,^3\Sigma^-$) and O (^{3}P), so other pathways must participate. The dominant process is thought to be internal conversion arising when mixing occurs between the quasibound continuum of the $\tilde{X}$ ground state with vibronic levels in the $\tilde{C}$ state, but dissociation via a triplet surface could also result from the crossing of the $\tilde{C}$ state by repulsive $2^3A'$ or $3^1A'$ states.[61,62,64,67] These conclusions were drawn, in part, from the observation of inverted vibrational distributions in the SO fragment, where >50% of the population is in the v″ = 2 vibrational level rather than the ground v″ = 0 state (Table 1).[61,63,64,68]

Table 4.1. Nascent vibrational distributions of SO ($X^3\Sigma^-$) from the 193-nm photodissociation of SO_2.

	Population (%)			
v″	REMPI + VMI[a]	LIF[b]	IR[c]	CPUF[d]
0	9	2	—	20
1	23	20	20	21
2	56	83	70	58
3	6	0	—	—
4	6	—	—	—
5	—	—	< 10	—

[a] Ref. [61]
[b] Ref. [63]; SO $A\,^3\Pi \rightarrow X\,^3\Sigma^-$ transition probed from 255 – 295 nm.
[c] Ref. [68]; tunable infrared diode-laser spectroscopy
[d] This work; vibrational distribution 25 μs after the laser was fired

The CPUF spectrometer was used to probe the nascent vibrational distribution of SO following photodissociation of SO_2. The SO_2 (Sigma Aldrich, 99.9%) was seeded at 0.5% in the helium flow and dissociated using an ArF excimer laser. To monitor the appearance of the product, the "fast-frame" capability of the oscilloscope was used,[45,49] described in detail in Chapter 6. Here successive spectra were obtained at 5 μs intervals following an initial 10 μs delay between the laser trigger and the first chirped pulse excitation. Ten frames (i.e. spectra) obtained in this fashion, each an average of roughly 6500 acquisitions, are shown in Figure 4.4. The spectra are stacked such that the top and bottom frames show the spectra collected at 20 and 65 μs after the laser is fired, respectively. Each frame shows the $N_J = 1_0 - 0_1$ pure rotational transition of SO in the $v'' = 2$, 1, and 0 vibrational levels near 30 GHz; other fine structure components of the $N = 1 - 0$ transition lie outside of the spectrometer's immediate frequency range. A small Zeeman splitting caused by the interaction with the Earth's magnetic field is visible on some of the lines as well.

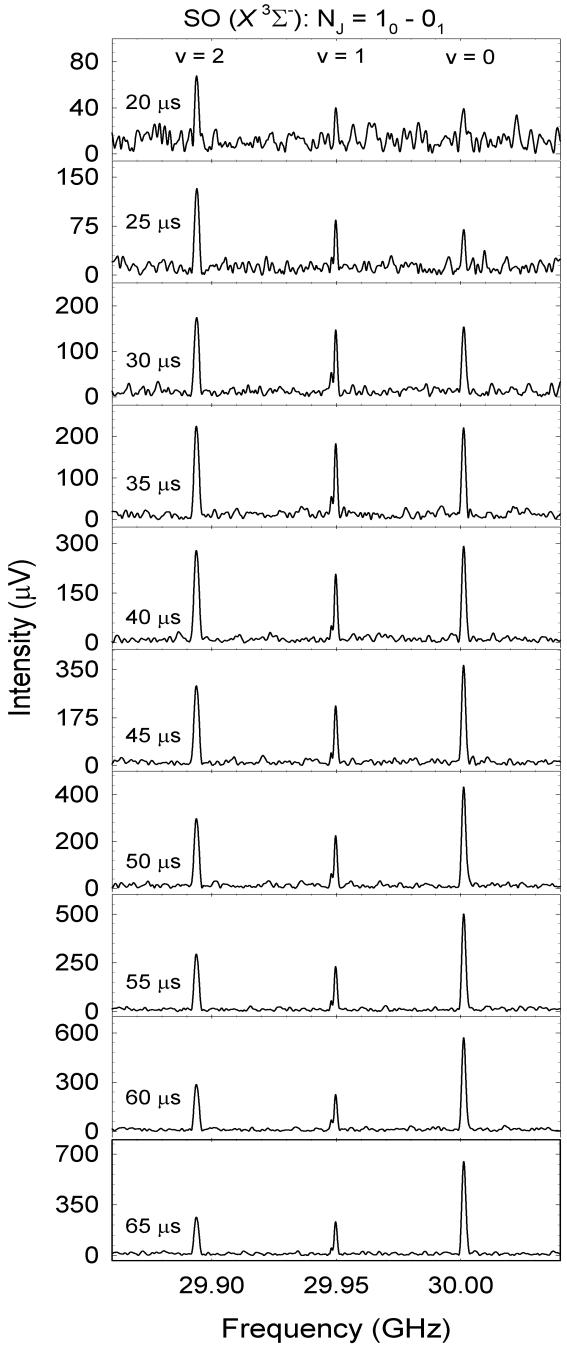

Figure 4.4. SO_2 was irradiated with 193 nm radiation to produce SO ($X^3\Sigma^-$) in its v″ = 0, 1, and 2 vibrational states. Shown here are spectra of the SO $N_J = 1_0 - 0_1$ rotational transition to illustrate the vibrational cooling of this photofragment over a 65 ms time frame. Times shown on the spectra are the time of the chirp after the firing of the laser. Initially, most of the SO population is in the v″ = 2 level, consistent with the nascent distribution determined from imaging studies, followed by fast relaxation to the v″ = 0 level. Each spectrum is an average of 6500 acquisitions.

The v″ = 2 level clearly dominates when the SO product first appears (see also Table 4.1), consistent with previous studies, but rapid vibrational quenching to the v″ = 0 state follows. Figure 4.5, which shows the populations of each vibrational state at different time points, illustrates this effect as well. It should be mentioned, however, that measurement of higher rotational states could also provide valuable insight, as it has been noted that there is a shift in population toward higher rotational levels in lower vibrational levels.[65,68,69] The very rapid vibrational relaxation observed here is likely owing to the near resonance of the SO fundamental (1149 cm^{-1}) with the SO_2 symmetric stretch (1151 cm^{-1}), possibly giving rise to very efficient v-v energy transfer.[18]

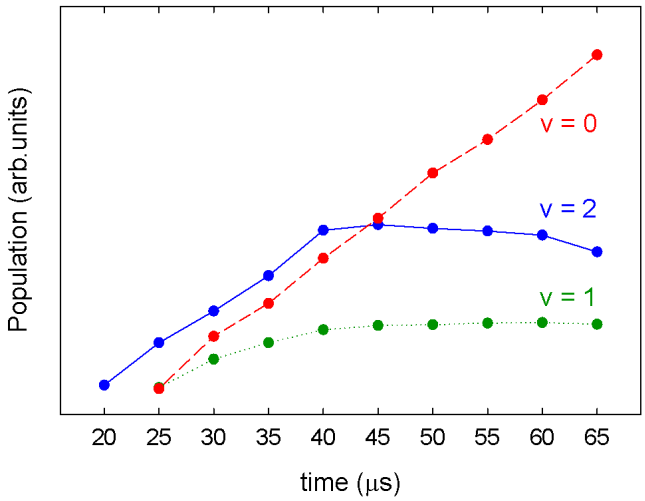

Figure 4.5. The populations of the v″ = 2, 1, and 0 vibrational levels of SO ($X\ ^3\Sigma^-$) are shown over time. Initially, only SO in the v″ = 2 state is present (t = 20 μs); S/N was not high enough to get reliable v″ = 1 and 0 populations at this time point. SO in the v″ = 1 state remains fairly constant over 65 μs, while v″ = 0 shows a large increase over time, due to fast vibrational cooling and possible v-v effects.

A more in-depth study could investigate the competition between rotational and vibrational cooling of SO fragments or probe vibration-vibration interactions between parent and daughter species, however that is beyond the scope of this demonstration. Nonetheless, this work shows that the CPUF spectrometer can be used to monitor nascent vibrational distributions and track vibrational and rotational relaxation kinetics.

4.3.3 Bimolecular Reactions: $CN + C_2H_2 \rightarrow HCCCN + H$

A distinct advantage of using a Pulsed Uniform Flow (PUF) system as the molecular source for this spectrometer is that it provides a high-density molecular flow at constant pressure and uniform low temperature. This feature offers the capability to initiate bimolecular reactions in the flow with a large enough number of product molecules in the probed volume, and with collisions to thermalize the molecules to uniform low rotational temperature quickly, so that CP microwave spectroscopy may be effectively employed as a probe. At the same time, it becomes possible to monitor the kinetics of these reactions, as we saw above for vibrational relaxation kinetics in SO. This combined system of broadband rotational spectroscopy in a PUF offers complementary capabilities when compared to the crossed-molecular beam approach to reaction dynamics studies. It allows for investigation of all the product channels for polyatomic molecules that possess an electric dipole moment and have rotational transitions within a desired frequency window in a single spectrum, so accurate product vibrational branching ratios can be measured. Further, microwave spectroscopy can reveal detailed isomeric identity and structural information. It does not offer differential cross sections or translational energy distributions, but for larger and more complex systems, these

differential measurements generally lack detail and offer somewhat limited insight. It is important to note, though, that these are necessarily not single-collision conditions, so competing reactions and alternative chemistry must always be borne in mind in interpreting the results.

There has been much speculation about the formation pathways of cyanopolyynes due to their importance in astrochemistry. Detection of this class of molecules in a wide variety of astrophysical environments[70–73] has led to the proposal that ion-molecule and dissociative recombination mechanisms or neutral-neutral reactions might be responsible for their presence in interstellar gas.[74] Low temperature CRESU kinetics measurements support the latter by showing that a neutral-neutral reaction between cyanogen, CN, and an acetylenic chain, such as C_2H_2 in the simplest case, could be very facile.[60] Such a reaction would proceed via an attack by the CN radical on a p orbital of C_2H_2 to create a C_2H_2CN complex, followed by a bond rupture to produce HCCCN and H, with these products lying at 90 kJ mol^{-1} lower enthalpy than the reactants.

To demonstrate the capabilities of the instrument to study bimolecular reactions, the CN + C_2H_2 reaction was investigated in the CPUF instrument. A mixture containing 1.5% C_2H_2 and 1% BrCN seeded in He (with 5% H_2 added to promote rotational cooling) was introduced into the chamber. Irradiation by a 40 mJ/pulse at 193 nm photodissociated the BrCN to produce CN radicals. Only the molecular product, HC_3N, was expected in the spectrum; neither of the reactants was observable because of lack of permanent dipole moment (C_2H_2) or having rotational transitions in a frequency window not accessible by our spectrometer (CN). Spectra of the J = 4 – 3 pure rotational transition of HCCCN in its

vibrational ground state, produced from the reaction of C_2H_2 + CN, are shown in Figure 4.6. Here spectra collected at successive 10 μs intervals up to 110 μs following the laser trigger show that HCCCN appears roughly 40 μs after the laser fires. The inset in Figure 4.6 tracks the time dependence of HCCCN, and shows an onset at 40 μs and modest increase to about 70 μs, after which there is a sharper increase before decaying after 90 μs. The apparent delay in HCCCN's initial appearance is likely due to the need for rotational cooling, similar to that seen in the SO_2 photochemistry study, while the more abrupt rise at 70 μs likely represents reactions that occur at the much higher densities present in the throat of the nozzle. This is confirmed by an estimate of the flow velocity

of 1500 m s^{-1} and the distance of the throat to the center of the horns of 12 cm, implying arrival of products from the high density region 80 μs after photolysis.

Rate constants have been measured for other reactions involving CN and hydrocarbons such as C_2H_6, C_2H_4 and C_2H_2 using the CRESU apparatus at 25 K under uniform flow conditions.[60] Using these rate constants for CPUF conditions, the product formation time scales are expected to be on the order of tens of microseconds, making them suitable targets for CPUF. Moreover, reactions involving related carbon chain systems may yield multiple products with significant dipole moments, enabling measurement of product branching ratios.

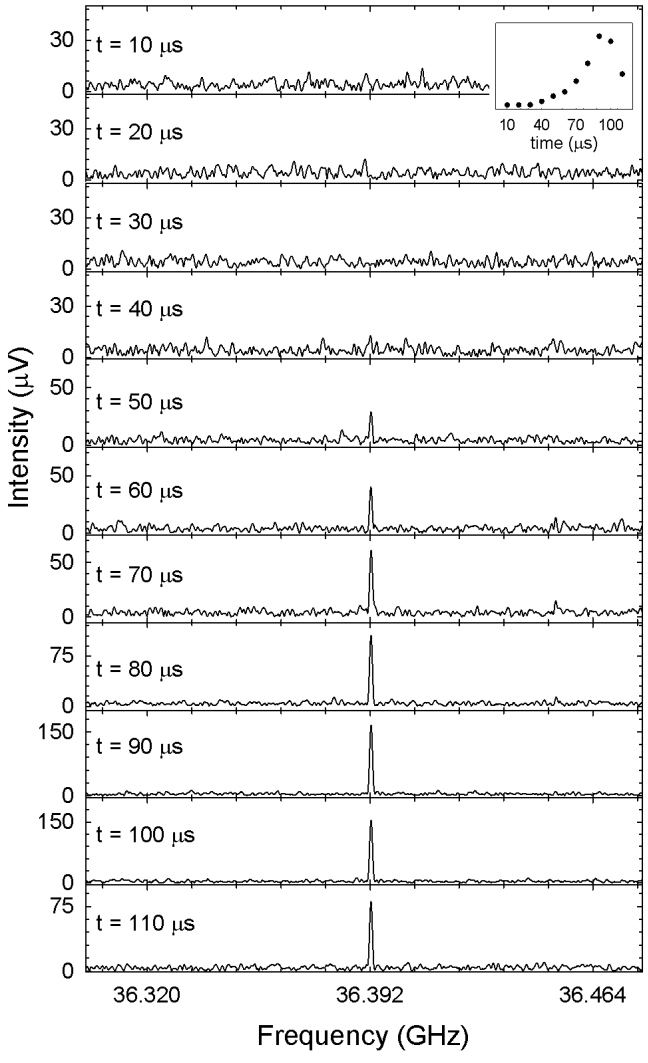

Figure 4.6. Spectra illustrating the time evolution of the J = 4 – 3 rotational transition of HCCCN ($\tilde{X}\ ^1\Sigma^+$), generated via the bimolecular reaction of the CN ($X\ ^2\Sigma^+$) radical and C_2H_2 ($\tilde{X}\ ^1\Sigma_g^+$), are displayed. The CN radical was produced by irradiation of BrCN with a 193 nm laser. HCCCN appears approximately 40 – 50 μs after the laser is fired. The inset shows the integrated intensity of the HCCCN line at each time point, with the peak intensity occurring at ~90 μs. Each spectrum is an average of 22000 acquisitions

4.4 Conclusions and Outlook

A new K_a-band chirped pulse Fourier-transform microwave spectrometer has been constructed for the purpose of investigating molecular reaction dynamics and kinetics. This spectrometer uses a high-throughput piezoelectric stack valve and a Laval nozzle to generate well-collimated high-density cold flows, such that photochemistry and bimolecular reactions can be initiated and the products thermalized with large volumes at high density. The spectral velocity advantage of the chirped pulse microwave technique allows for the efficient simultaneous measurement of several spectral lines with reliable intensity ratios, making it possible to establish accurate branching ratios if many species are present. To demonstrate the spectrometer's capabilities, two well-known systems were chosen for study, the 193 nm photodissociation of SO_2 and the reaction between C_2H_2 and CN. These examples show the power of this instrument for studies of photochemistry and bimolecular reactions. This new technique should be complementary to traditional techniques for studying reaction dynamics, especially for systems involving small polyatomic molecules.

The main challenge with this new method is the generation of sufficient reaction products to obtain adequate signal intensities. Increasing the reactant concentration could aid in this goal, however this will also lead to more clustering or quenching in the flow, effectively attenuating the signal. Two other avenues to increased signal are greater photolysis laser power, which is readily achieved, and larger nozzles for larger flow volumes, which can also be implemented fairly easily. In Chapter 2 we have demonstrated larger flows of longer duration with an argon nozzle, but it appears that

clustering in an argon flow inhibits achievement of adequate concentrations. A helium/neon nozzle is planned to be developed that may represent an optimum compromise for density, volume, and collision frequency.

Despite these challenges, the promise of CPUF is considerable. Photochemistry with complex and competing product branching represents an important initial direction. Further bimolecular reactions between the cyano radical and various hydrocarbons have been studied from both experimental and theoretical perspectives, but questions still remain regarding product branching ratios.[75–77] These reactions are attractive targets for CPUF because, in many cases, the microwave spectra of the products are already known and the relevant species have large electric dipole moments. This is well demonstrated in Chapter 5. Other systems targeted for future CPUF investigations are Criegee intermediates and QOOH products or reactions of the methylidyne radical (CH) with small hydrocarbons. Just as with the Criegee compounds, the ability to cool and trap molecules as transient intermediates holds promise for new insights into the role of such species in reaction dynamics. CPUF is an ideal instrument with which to pursue such studies.

CHAPTER 5

Quantitative product branching for multichannel reactions with CPUF: The low temperature reaction of CN + CH_3CCH

5.1 Introduction

The interplay between fundamental laboratory investigations, theoretical advances, and chemical modeling has led to tremendous progress over the past decade in understanding complex gas-phase environments, from cold interstellar clouds to combustion systems[78,79]. Measured or calculated reaction rates for thousands of elementary reactions are incorporated into models of chemistry under extreme conditions to identify key pathways that control reaction outcomes. However, nearly all kinetics studies report the observed rate of *reactant disappearance*, with product identity and branching largely unknown. This limitation arises from considerable experimental challenges inherent in the quantitative detection of the full range of products of a given reaction, particularly for large polyatomic systems. Recent advances have relied upon tunable synchrotron photoionization or low-energy electron impact ionization to achieve selective product detection in dynamics, kinetics, and flame studies.[4,80–82] These pioneering studies have demonstrated a general capability for isomer-specific product branching determination in flame studies, kinetics and crossed-beam scattering, highlighting the importance of such information for accurate kinetic modeling.

Challenges remain; however, as these studies require fitting of composite, often incompletely resolved spectra to infer branching, and clear product signatures are often lacking.

As an alternative approach to address these challenges the Chirped-Pulse in Uniform Flow (CPUF) spectrometer, introduced in Chapter 4 was employed. The unique advantage of having a pulsed uniform flow system as its molecular source enables the capability to initiate bimolecular reactions in the flow with a large enough number of product molecules in the probed volume. Having enough collisions to thermalize the molecules to uniform low rotational temperature quickly makes the reaction products to be easily accessed by the spectrometer. An additional advantage thru broadband capability is the ability to detect multiple products initiating form both the direct and indirect channels of a complex bimolecular reaction and most of them to be detected in one frequency window enabling a more precise estimation of product branching between channels and among products.

One class of reactions well suited to demonstrate the new technique involves the cyano radical owing to the large dipole moments of the products, and given its importance in combustion and astrochemistry. In combustion, both the CN radical and HCN have been detected as intermediates or products from the burning of hydrocarbons in the presence of nitrogen. These species can then play a key role in NO_x formation/destruction mechanisms and in nitrile incorporation in soot formation processes. In the interstellar medium (ISM), more than 30 species that contain a CN group have been detected, from small metal cyanides in circumstellar envelopes to large

(> 6 atoms) organic species in dense molecular clouds.[71,73,83–86] Within the solar system, Saturn's moon Titan is enveloped by a yellowish haze that is attributed to nitrile- and hydrocarbon-rich aerosol haze layers.[87–90] However, despite the ubiquity of this class of molecules in the ISM and in combustion systems, the formation mechanisms are still poorly understood. Nonetheless, some insight has been gained from gas-phase kinetic measurements for reactions between the CN radical and several hydrocarbons at temperatures down to 13 K.[8,14,15,17,91,92] Other investigations have been carried out using crossed-molecular beam methods to characterize the reaction dynamics and identify the reaction products for this class of reaction.[93,94] Despite this effort, the determination of detailed product branching remains challenging.

In this Chapter a detailed study of the reaction of the cyano radical with propyne using the CPUF technique is presented. Line intensities from rotational spectra have been used to determine the product branching from each of the accessible reaction pathways:

Direct Abstraction

$$CN + CH_3CCH \rightarrow HCN + CH_2CCH \qquad 5.1$$

CN addition/methyl elimination

$$CN + CH_3CCH \rightarrow CH_3 + HCCCN \qquad 5.2$$

CN addition/H elimination

$$CN + CH_3CCH \rightarrow H + CH_3CCCN \qquad 5.3$$

$$CN + CH_3CCH \rightarrow H + CH_2CCHCN \qquad 5.4$$

With support of ab initio and statistical calculations, these measurements reveal the underlying dynamics of this reaction, thus providing important insights for the modeling

of complex gas-phase environments.

5.2 Experimental

The CPUF spectrometer used for this experiment shown is Figure 5.1, it consists of an 8 gigasamples/s arbitrary waveform generator (AWG; Tektronix AWG7082C), which is used to produce a linear frequency sweep, and a phase-locked dielectric resonator oscillator (PDRO) at 8.125 GHz to upconvert the AWG pulse via a broadband mixer (Marki M10418LC). The mixer output is amplified with a broadband amplifier (ALC Microwave ALS030283), the desired band is selected through a bandpass filter and propagated through a 8× multiplication stage to obtain the final frequency of 60-90 GHz with an output power of ~100 mW. Typical chirp duration was ~1 μs with FID collection for 1-2 μs. The laser and gas pulse were operated at 3.5 Hz.

The final frequencies were transmitted via a feedhorn into the high-density polycarbonate uniform flow chamber where the bimolecular reaction is initiated. The free induction decay (FID) of the polarized sample is collected through the detection feed horn, amplified with a low noise amplifier (LNA; Miteq AMF-4D-00100800-18-13P), downconverted, and sent to a digital oscilloscope (Tektronix DPO70804C) for time-domain averaging and signal processing.

In order to achieve a uniform mixture throughout the scans, two mass flow controllers (Bronkhorst EL-Flow) were used. Pure He gas (600 sccm) was passed over solid cyanogen bromide (BrCN; Sigma Aldrich, 97%) at room temperature with a backing pressure of 3 bar. The output was mixed with a 9 sccm flow of pure methylacetylene (Sigma Aldrich, 99%) to obtain a 1.5% mixture of CH_3CCH in

BrCN/He. Total density in the flow was ~3.8×10^{16} cm^{-3}. An excimer laser (GAM Laser, EX200/60) with 60 mJ/pulse of 193 nm (loosely focused to a fluence of ~100 mJ/cm^2) was used to photodissociate BrCN and produce the CN radical at an estimated density of 5×10^{13} cm^3. Additional details are provided in our previous publication.[7]

Computational:

Electronic structure calculations were performed at the CBS-QB3 level of theory, which extrapolate the energetics at the complete basis limit in order to obtain an accuracy of ~5 kJ mol^{-1} after zero-point energy correction. This composite method involves geometry optimization and vibrational frequency calculation at the B3LYP/6-311G(2d,d,p) level; the same vibrational frequencies were used to compute the partition functions of the different minima and saddle points in the Rice–Ramsperger–Kassel–Marcus (RRKM)[95–97] calculations of energy-dependent rate constants for all individual unimolecular steps. These rate constants were estimated at an internal energy fixed by the reactant asymptote and we assumed that the available energy was converted to internal vibrational energy

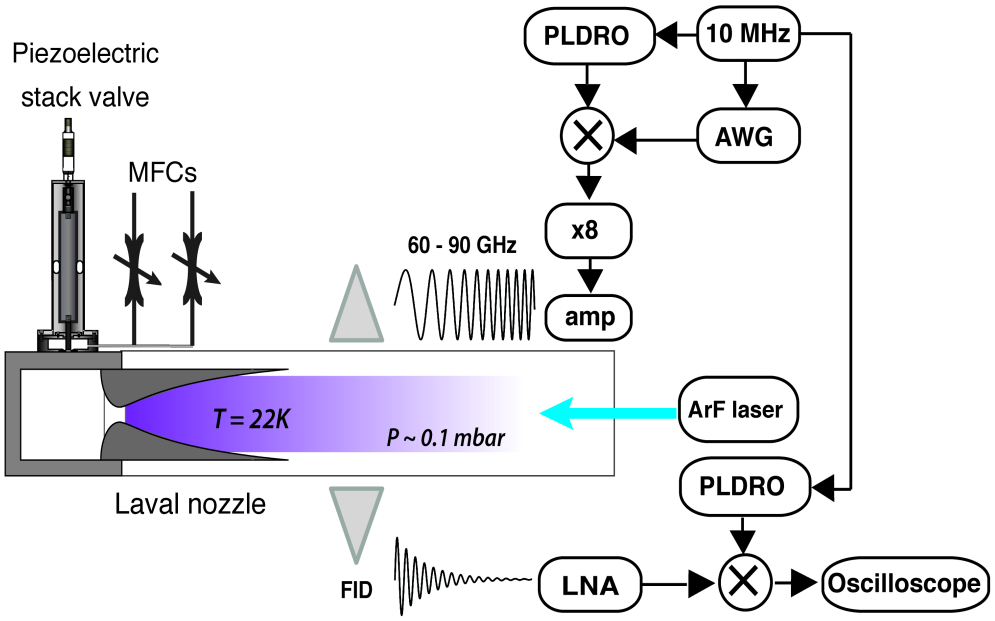

Figure 5.1. A schematic for CPUF is shown. Linearly chirped pulses (0.25 – 3.75 GHz) are produced in an arbitrary waveform generator (AWG) and then mixed with a PLDRO (frequency 8.125 GHz) locked to a 10 MHz Rb standard. The resulting frequencies are then multiplied, amplified, and broadcast onto the flow via a feedhorn that is oriented perpendicular to the flow axis. Bandpass filters and isolators are inserted into the setup as necessary. The pulsed uniform flow source consists of a piezoelectric stack valve[98], connected to mass flow controllers (MFC), and a Laval nozzle mounted on one end of a polycarbonate vacuum chamber.[57] A quartz window is located on the other end of the chamber to allow radiation from an ArF excimer laser to propagate down the axis of the Laval nozzle, such that the core of the flow is irradiated. The resultant molecular emission from the core is collected as free induction decay (FID) by a second feedhorn, amplified through a low noise amplifier (LNA), downconverted before detection, and phase-coherently averaged in an oscilloscope, where it is fast Fourier-transformed to produce a frequency-domain spectrum

5.3 Results and discussion

To guide the spectroscopic investigation, the ground–state potential energy CN + propyne surface (Figure 5.2) was modeled at the CBS-QB3 level of theory. First there is a direct barrierless abstraction path to form HCN and propargyl radical that is exoergic by 149 kJ/mol. We also find two barrierless C1 *cis/trans* addition complexes, bound by over 230 kJ/mol and separated by a 22.5 kJ mol^{-1} isomerization barrier, largely consistent with the previous theoretical work.[77,99] In addition, a barrierless C2 addition complex, 18.5 kJ mol^{-1} higher in energy than the *trans*-C1 complex, is also present. There is an isomerization barrier of ~100 kJ/mol separating the C1 and C2 complexes, which is considerably lower than any exit pathway, thus equilibration between these complexes prior to dissociation is very likely at these low collision energies. The lowest energy exit pathway from the addition complexes leads over TS_{5b} to methyl elimination and cyanoacetylene formation. The C1 complexes can pass over TS_{6b}, slightly higher than TS_{5b}, to yield H + cyanomethylacetylene, or at yet slightly higher energy, they may pass over TS_{7b} to give H + cyanoallene. Another possibility for the C1 complexes is to pass over a 195 kJ mol^{-1} H migration barrier TS_4 to form the HmigC1 complex. This H migrated complex has the lowest exit barrier, 158.8 kJ $mol^{-1}$and it yields the methyl elimination product. Thus, the potential energy surface suggests that the reaction products listed in Eqs. 5.1–5.4 are appropriate targets for a spectroscopic investigation. Rice–Ramsperger–Kassel–Marcus (RRKM) calculations of energy-dependent rate constants for all individual unimolecular steps were also performed.

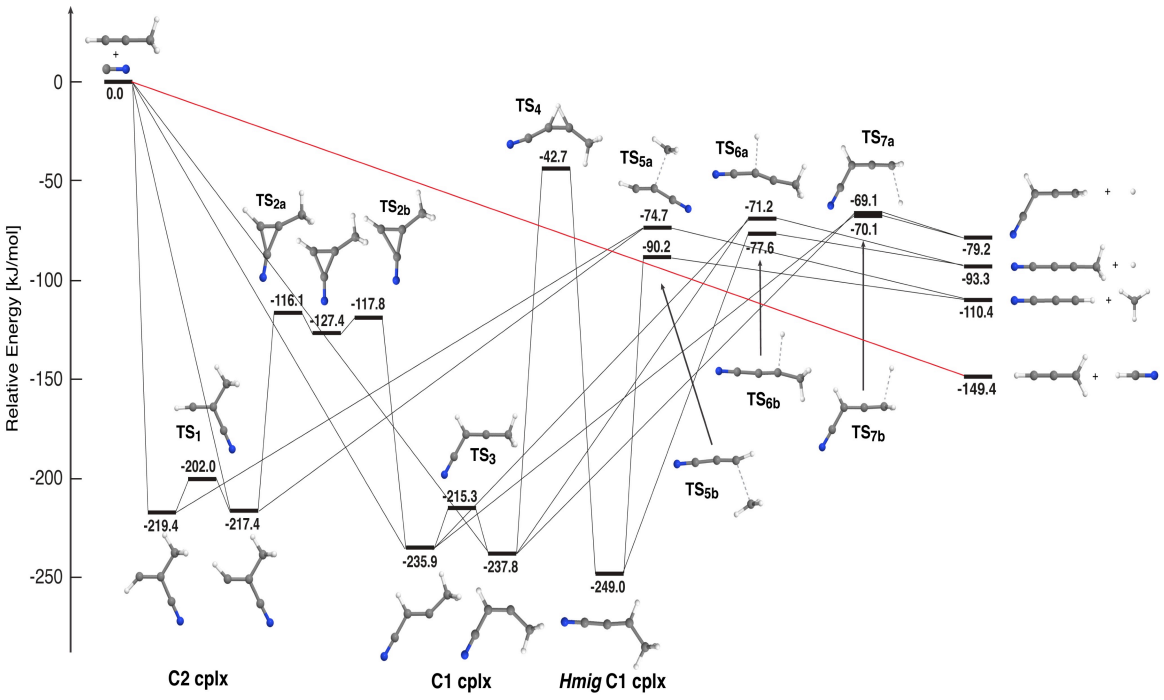

Figure 5.2. Key stationary points on the potential energy surface for the CN + CH_3CCH reaction, calculated at CBS-QB3 level of theory.

The ~22K flow[8] consists of 0.5% BrCN and 1.5 % propyne in helium, and the reaction is initiated by 193nm photodissociation of BrCN. Successive spectra were obtained at 10μs intervals following the laser trigger and the first chirped pulse excitation.[100] Twelve frames (i.e. 12 independent spectra) were obtained in this fashion for each gas pulse, with each frame averaged for roughly 62500 acquisitions. All bimolecular reaction products began to appear approximately 50 μs after the laser trigger, and show a slow rise followed by a more abrupt rise at 80-90 μs (see Figures 5.4-5.7), which is consistent with our previous observations in Chapter 4. The delay in the initial appearance is likely owing to rotational cooling of the CN prior to reaction, as it is known to be formed vibrationally cold but rotationally hot from 193 nm photolysis of

BrCN.[101,102] Rotational and vibrational thermalization of the products may also contribute to this delay. The average of the 8th and 9th frames were used to determine the branching reported here. We note that the rise at later times may include some contribution from reaction occurring in the nozzle throat that may not have reached the 22 K flow temperature, but this is not likely to impact the measured branching. The disappearance of the products at longer times is owing to the passage of the reacting sample out of the probe region.

Figure 5.3 shows spectra recorded over two frequency regions. The top spectrum (Figure. 5.3a) was collected using segmented macrochirps, (50 MHz bandwidth each) over a total 1.5 GHz range. These different chirping schemes implemented with CPUF will be discussed in the next Chapter in details. In this fashion, the strongest transitions of the indirect-channel products could be probed: HCCCN (J=9-8 transition at 81.881 GHz), CH_3CCCN ($J_K=20_0 – 19_0$ at 82.627 GHz) and CH_2CCHCN ($J_{Ka,Kc}=16_{0,16}$-$15_{0,15}$ at 81.674 GHz). HCCCN and CH_3CCCN were clearly detected, however CH_2CCHCN was not. Additional spectral lines are present, most of which are attributable to the BrCN precursor. Figure 5.3b shows a broad 86.63–88.73 GHz scan, covering the $J_{Ka,Kc} =17_{0,17}$-$16_{0,16}$ transition of CH_2CCHCN at 86.668 GHz, the $J_K =21_0–20_0$ transition of CH_3CCCN at 86.750 GHz, and the J=1-0 transition of HCN at 88.631 GHz. Again, CH_2CCHCN was not observed, although both CH_3CCCN and the direct product HCN were observed, which allows comparison between the direct and indirect reaction pathways. Time sequence spectra of HCN, HCCN, CH_3CCCN ($J_K=20_0 – 19_0$) and ($J_K=21_0 – 20_0$) with the integrated kinetic traces are given are shown in Figure 5.4 -5.7 respectively.

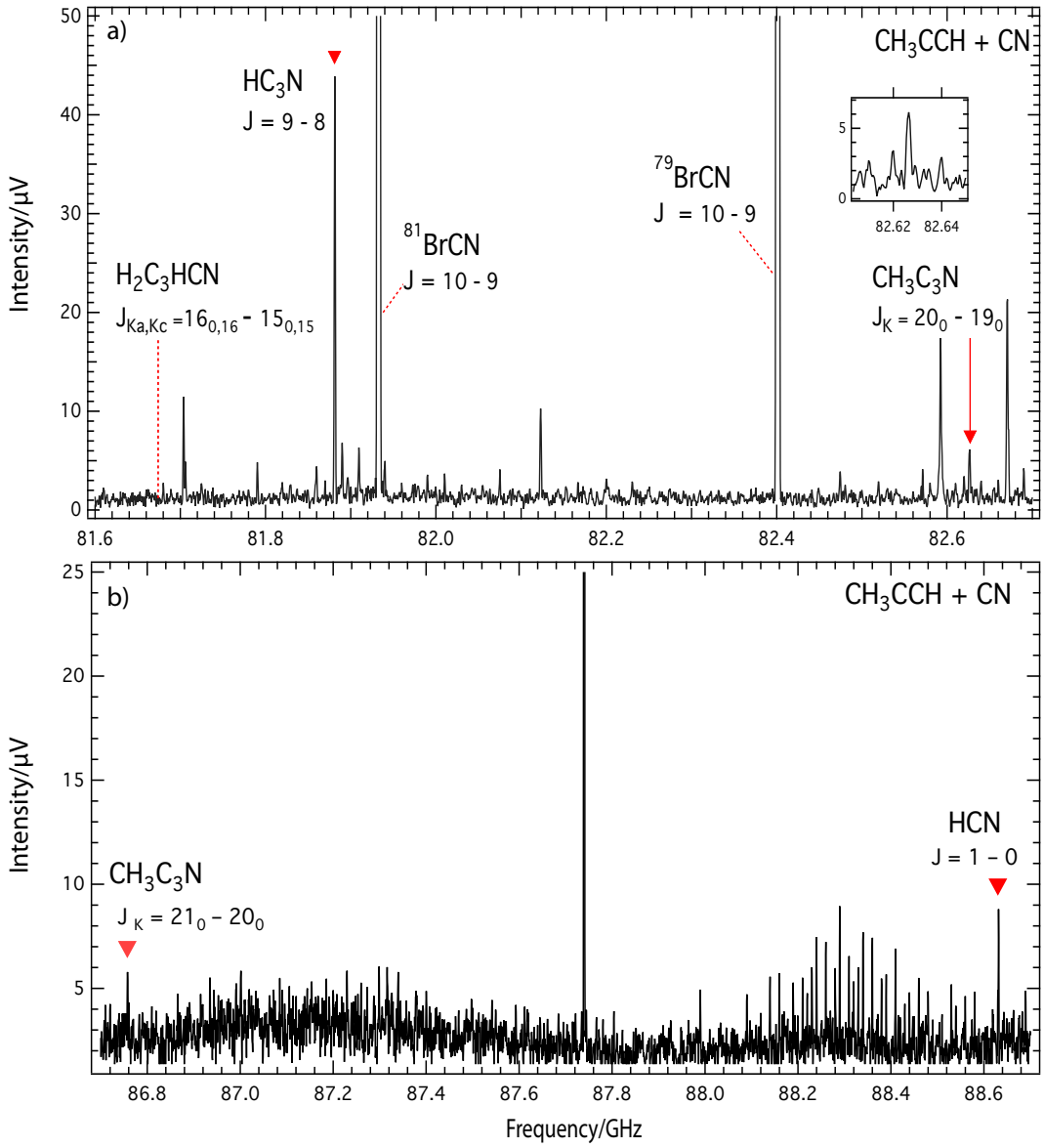

Figure 5.3. Chirped-pulse Fourier transform microwave spectra for reaction products of the CN + propyne reaction. A) a segmented macrochirp scan that targets transitions of HCCCN, CH_2CCHCN and CH_3CCCN; J=9-8 transition at 81.881 GHz, $J_{Ka,Kc}=16_{0,16}$-$15_{0,15}$ at 81.674 GHz and $J_K=20_0 - 19_0$ at 82.627 GHz. The inset shows the K=0,1,2,3 transitions of CH_3CCCN. B) A broad scan from 86.63-88.73 GHz that targets the $J_{Ka,Kc}=17_{0,17}$-$16_{0,16}$ transition of CH_2CCHCN at 86.668 GHz, the $J_K=21_0$–20_0 transition of CH_3CCCN at 86.750 GHz, and the J=1-0 transition of HCN at 88.631 GHz. Each spectrum is averaged for 125000 laser shots.

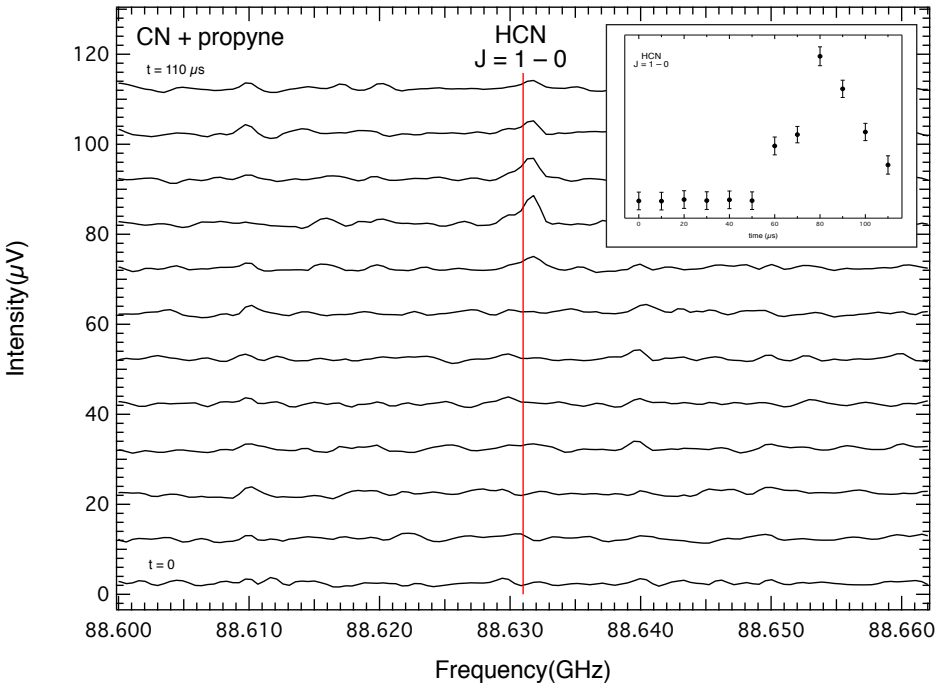

Figure 5.4. Time series and integrated kinetic traces for HCN product

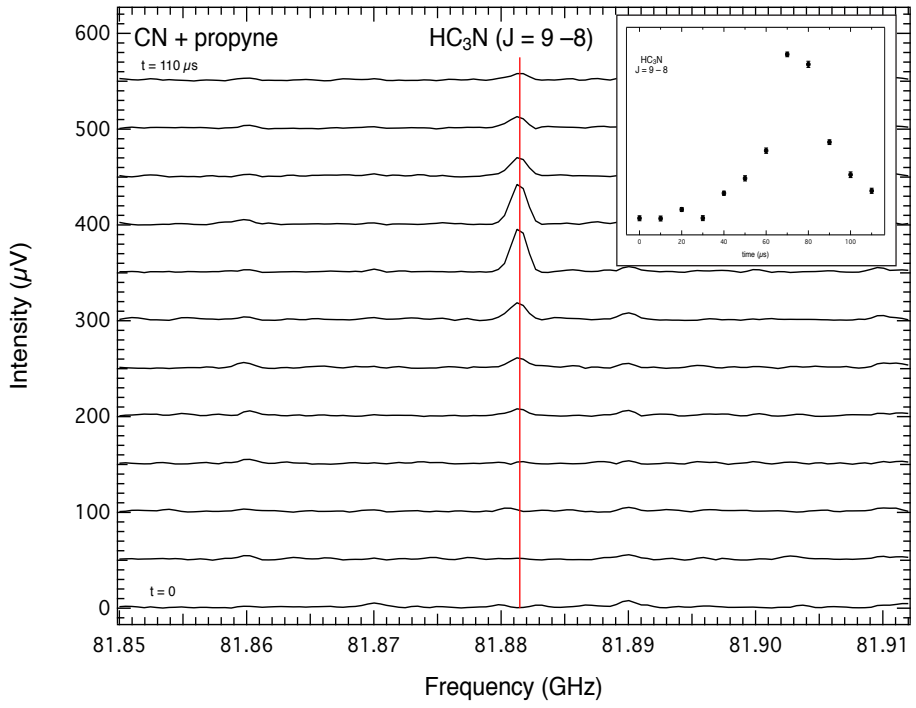

Figure 5.5. Time series and integrated kinetic traces for HCCCN product

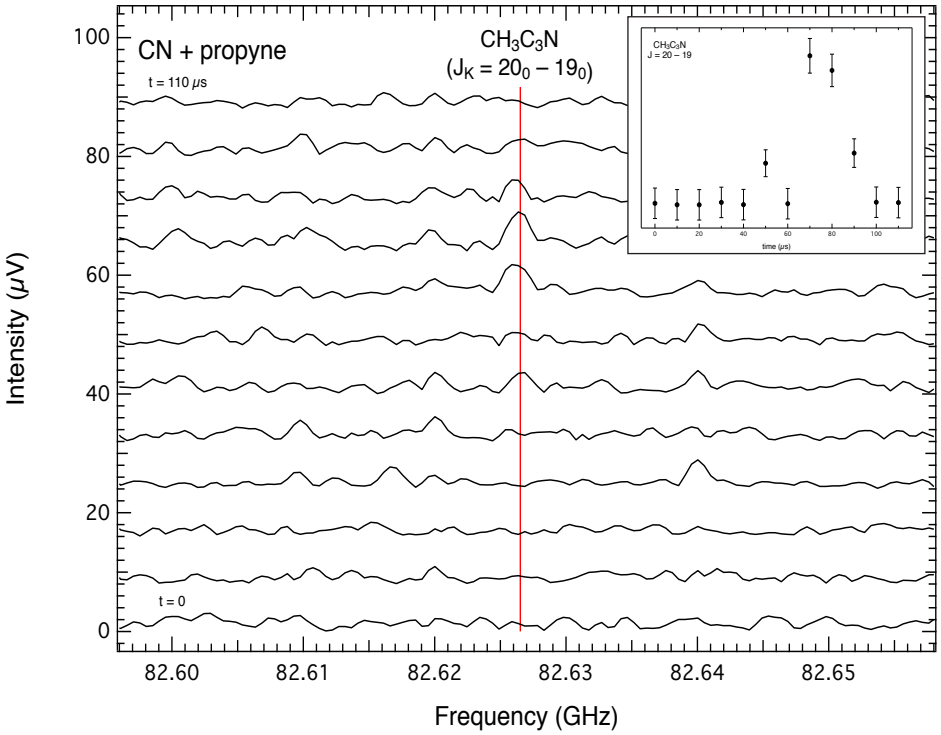

Figure 5.6. Time series and integrated kinetic traces for CH3CCCN product on $J_K(20_0\text{-}19_0)$ transition

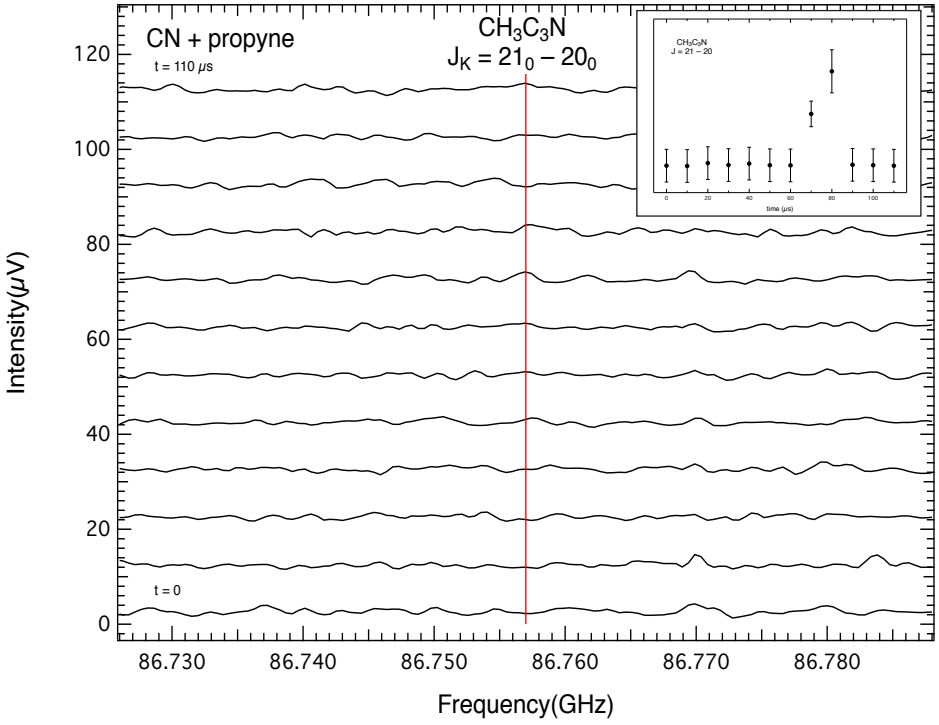

Figure 5.7. Time series and integrated kinetic traces for CH3CCCN product on $J_K(21_0\text{-}20_0)$ transition

We have considered the possibility that primary product of the CN + CH_3CCH reaction goes on to react further. However, all possible secondary reactions are too slow to contribute on the timescale of the experiment, so this interference is deemed unlikely. Control experiments were also performed and all signals were found to require the two reactants and the photolysis laser. We also performed a scan over the HCN region with allene substituted for propyne. No HCN was seen. Given the fact that propyne and allene show the same photochemistry at 193nm[103] but allene has a fourfold larger absorption cross section, this result strongly suggests that propyne photochemistry does not contribute to the observed HCN signals.

Relative product populations (branching) can be calculated using the relationship between the integrated line intensities (W) and column densities (N_{tot})

$$W = \frac{4\pi^{3/2}\omega_0^2 S\mu_i^2 g_I g_K \varepsilon}{c\sqrt{\alpha}} \frac{N_{tot}}{kT_{rot}Q_{rot}} e^{-E_l/kT_{rot}} \qquad (5.1)$$

with k the Boltzmann constant, ω_0 the transition frequency, a the sweep rate, and Q_{rot} and T_{rot} the partition function and rotational temperature, respectively. The quantities S, μ_i, g_I, and g_K represent the line strength, dipole moment, nuclear spin weight, and K degeneracy.[104] Fractional abundances relative to CH_3CCCN were calculated for each product using their respective integrated line intensities. For CH_2CCHCN, an *upper limit* to its abundance could be obtained from the noise level of the spectrum. Although the spectra shown in Figure. 5.3 were collected separately; the presence of CH_3CCCN in both spectra enabled scaling of the two scans. Thus, quantitative branching ratios could be determined between the direct (HCN) and indirect (HCCCN, CH_3CCCN) reaction pathways. Error bars (2σ) on the branching were based on the uncertainty in the spectral

line widths and intensities for each species, determined from Gaussian fits of each line. No other sources of error were assumed.

Experimental and calculated branching ratios for this reaction are shown in Table 5.1. The CPUF results include the HCCCN and CH_3CCCN products arising from indirect addition/elimination reactions and the HCN product from direct H abstraction. The RRKM results are only applicable to branching between the various addition-elimination channels (i.e. indirect pathways), thus they have been adjusted accordingly to account for the measured branching into the direct channel.

Table 5.1: Product branching (%) for the reaction of CN with CH_3CCH at 22 K with 2σ uncertainty in the last digit. RRKM calculations for the product branching in the addition/elimination reactions starting from either C1 or C2 addition complexes

		Addition-elimination			Direct Abstraction
		HCCCN	CH_3CCCN	CH_2CCHCN	HCN
CPUF		66(4)	22(6)	0(8)	12(5)
RRKM	C1 cplx	48	33	7	-
	C2 cplx	65	19	4	-

Experimental results show the branching between the direct and indirect channels to be roughly 12% to 88%. The fairly small branching to the direct reaction is perhaps not surprising despite the exoergicity given the low collision energy and the strong electrophilic interaction of CN with the propyne π system. The indirect addition/elimination pathway produces three possible products: HCCCN by CH_3 elimination and CH_3CCCN and CH_2CCHCN from H elimination, with experimentally

determined branching of 66%, 22%, and an upper bound of 8%, respectively. RRKM calculations initiated at the C1 and C2 minima support this result, with 48 or 65% into HCCCN and 33 or 19% into CH_3CCCN, respectively. These values are also consistent with the fact that that HCCCN is the lowest-energy product in this pathway and can be produced from either the HmigC1 or C2 complex. Both CH_3CCCN and CH_2CCHCN can also arise from either C1 adducts, but not from C2. From either C1 complex the pathway leading to CH_3CCCN formation has a lower exit barrier, making it the more favorable of the H elimination products.

These results can also be compared to previous crossed molecular beam (CMB) studies conducted at collision energy of 27 kJ mol^{-1}.[77,99,105] The CMB studies only reported detection of the H elimination products, and based upon selective deuterium labeling, nearly equal branching to the two H loss products was inferred. This estimate required some assumptions about product detection efficiencies, and also neglects the isotope dependence of the decomposition, which may well be important for H elimination. In general, these CMB investigations suffer from kinematic constraints that favor detection of products with small center-of-mass recoil velocities. As such, the CMB studies were unable to detect the CH_3 elimination product, HCCCN, or the direct reaction to HCN.

The good agreement between the theoretical and observed product branching underscores the ability of CPUF to obtain reliable branching among competing channels and their products. CPUF can provide detailed product branching with unambiguous, isomer-specific product detection, adding a powerful new tool to the reaction dynamics

repertoire for polyatomic systems that includes CMB methods with electron impact detection as well as synchrotron-based VUV photoionization.

CHAPTER 6

New Directions for CPUF

6.1 Designer Chirps

Chirped-pulse spectroscopy techniques have evolved substantially from their preliminary introduction by Pate and coworkers[12]. Advancement in communication technology and digital electronics has opened the door for new methods that reduce the data acquisition time of experiments, while still increasing the signal-to-noise ratio (S/N). The FastFrame™ technology available in newer Tektronix oscilloscopes enables the collection of multiple FIDs from a single gas pulse. This enables averaging multiple FIDs in the time domain to a "summary frame", which can be individually Fourier transformed, thereby significantly reducing the data acquisition time[45]. The other benefit is the ability to record each FID in sequence and Fourier transform each frame independently[106]. The latter would require substantial computing power of the oscilloscope, but it is ideal to study an evolution of a species population sequentially. In addition to multiple repetition of the same chirp, a sequence of chirps centered at different center frequencies and bandwidths (multi-chirp)[107] can be produced in a single gas pulse. This method is useful in looking at species that have weak signals but, known transition frequencies. A combination of a broadband chirp with individual chirps targeting transitions of desired species will aid in obtaining higher S/N spectra of several chosen species with meaningful relative intensities that can be converted into their relative concentrations.

The development of CPUF as a new tool for reaction dynamic is faced with the major challenge of detecting reaction products and intermediates initiated from photolysis and bimolecular reactions. It would be ideal to have multiple chirps followed by long FID collections for photolysis products with multiple laser shots per gas pulse. But, due to the limited repetition rates of lasers, new approaches had to be implemented to reduce the data acquisition time and improve signal quality for reaction dynamics and kinetics investigations in CPUF. This section discusses various chirp approaches used in CPUF experiments. As general settings for all of the methods discussed below, the Arbitrary Waveform Generator (AWG) is set to a sequential mode with a defined frame (chirp+FID) length held (~10μs). The oscilloscope FastFrame™ event duration is matched with the AWG frame length for data synchronization. A pulse delay generator controls the delays between the gas pulse and the laser relative to the chirp sequence.

6.1.1 Sequential Chirps

This method shown in Figure 6.1 is similar to the standard FastFrame™ technique discussed earlier. The first chirp is in time with the laser ($\Delta t=0$) and multiple similar chirps are sequentially produced with 10μs intervals for the same gas pulse. The delay between the chirps depends mainly on the FID collection time for each event. This method enables us to collect time evolution spectra of a product or reaction intermediate following initiation from a photolysis or a bimolecular reaction.

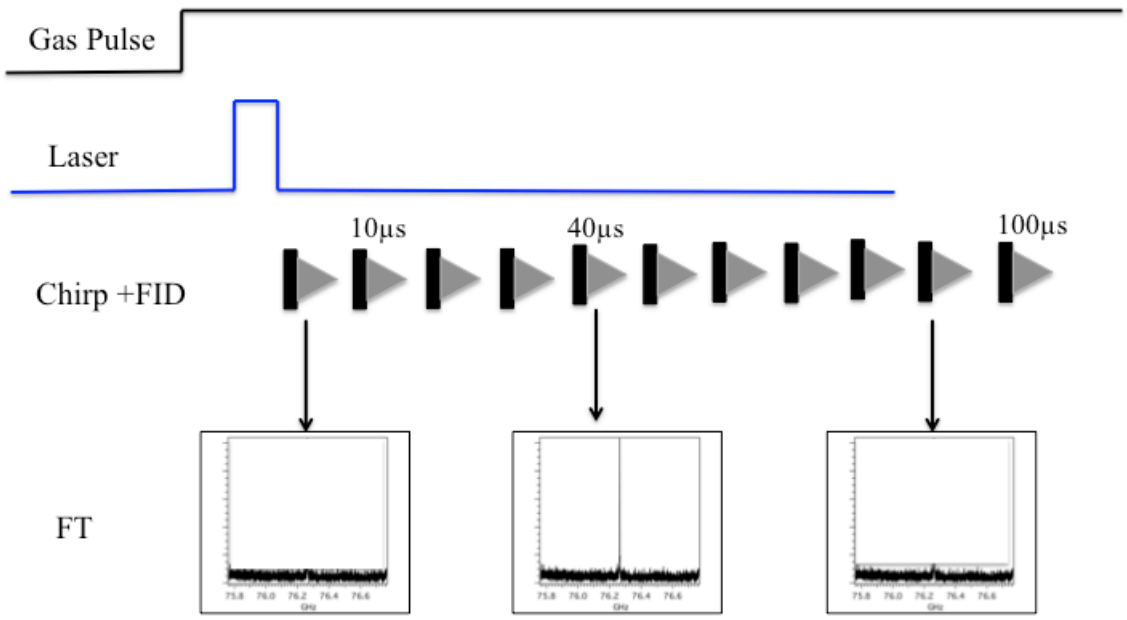

Figure 6.1 Timing sequence for a sequential chirp setup. Multiple FIDs are collected at 10µs intervals after the laser per single gas pulse.

The use of sequential chirps was briefly discussed in chapter 4. The approach was chosen to acquire data for both the 193 nm photolysis of SO_2 and the bimolecular reaction between $CN+C_2H_2$. CPUF mainly benefits for this approach as it provides a validation for reactions initiating and thermally equilibrating under uniform flow conditions.

The sequential chirp approach was employed to investigate the excited vibrational modes of HC_3N produced by the 193nm photodissociation of vinyl cyanide and the bimolecular reaction between $CN+C_2H_2$. In both Figures 6.2 and 6.3 it is clearly evident that HC_3N is produced in the uniform flow and is similar to previous observations in Chapter 4. This demonstrates the potential of CPUF to be a unique detection scheme to detect both ground and mode-specific vibrational excitation in molecules.

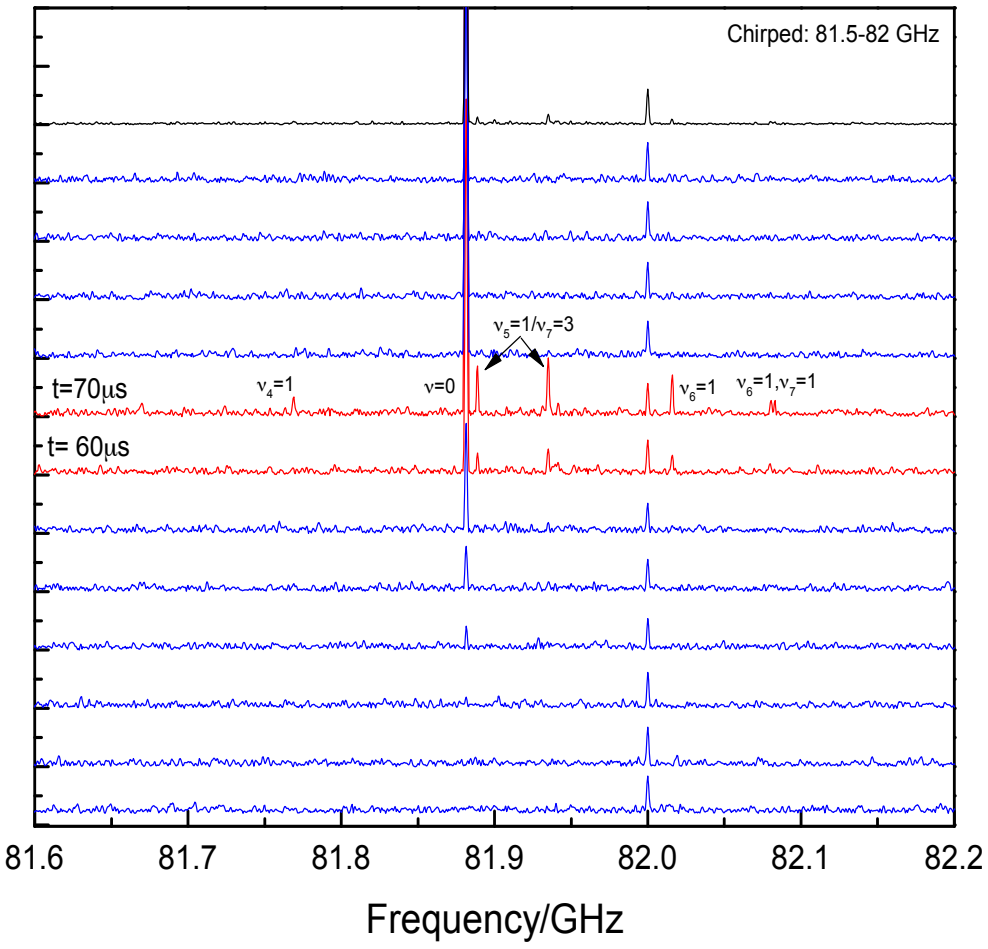

Figure 6.2. Vibrationally excited HC_3N produced through the 193 nm photodissociation of C_2H_3CN

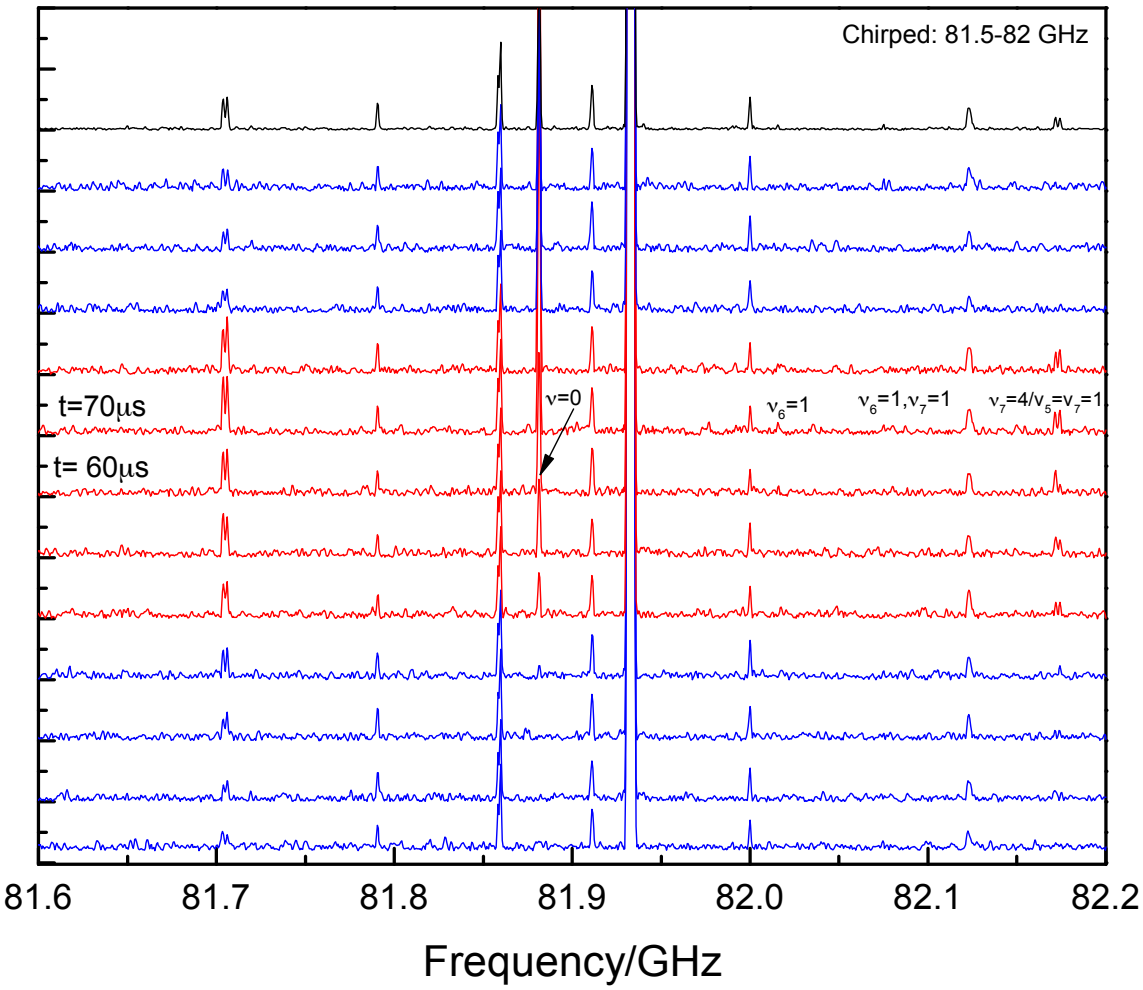

Figure 6.3.Vibrationally excited HC_3N produced through the bimolecular reaction of $CN+C_2H_2$

6.1.2 Sequential Multichirps

As shown in Figure 6.4 sequential multichirping is similar to the multi-chirp approach discussed earlier. Chirps centered at different central frequencies and bandwidths are chirped at different time intervals from the laser in the same gas pulse. This enables one to target products at desired times after the reaction is initiated. Therefore, instead of using broadband chirps in repetition this method permits use of narrow band chirps with more power concentrated on a particular transition frequency of a known product at a given time after the laser is triggered. The number of chirps for a particular transition can be arbitrary.

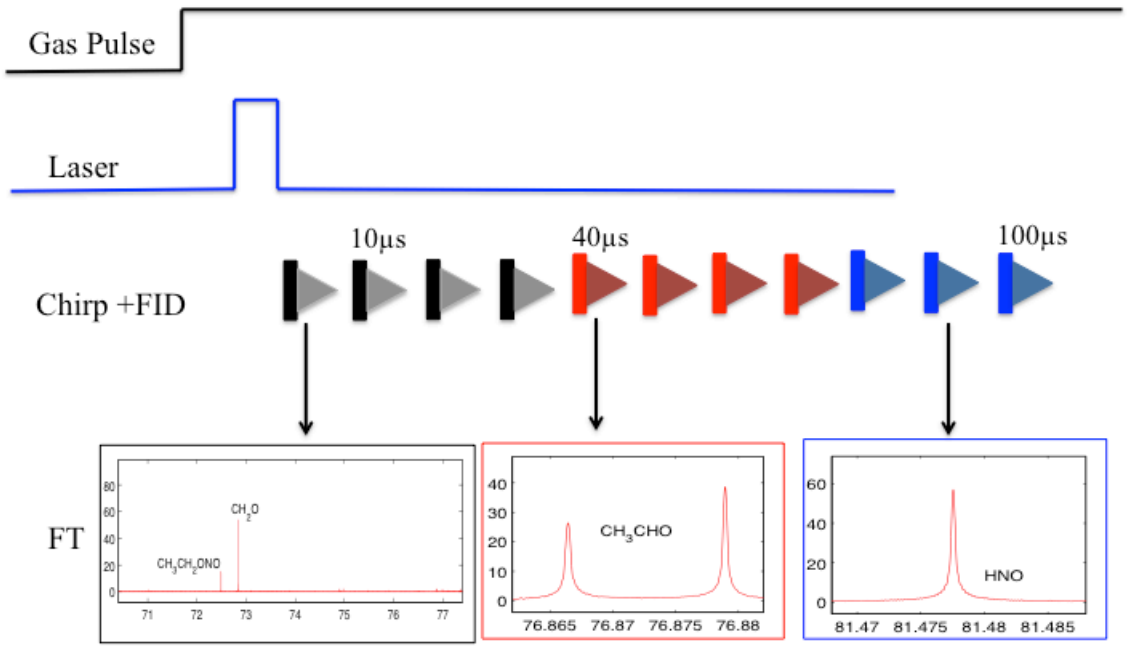

Figure 6.4 Timing sequence for a sequential multichirp setup. Multiple FIDs of multiple chirps are collected at different time intervals after the laser per single gas pulse.

6.1.3 Segmented Multichirps

This method shown in Figure 6.5 enables segmental excitation of individual transitions using narrowbands chirps in a single event (frame). Therefore, in a single gas pulse it will enable us to look into complete time evolution of several different reaction products initiated by the laser in one window sequentially. As narrowband chirps are used to drive each individual transition, the signal quality will be much higher than the broadband sequential chirp method discussed above. Thus it serves as an ideal approach for reaction dynamic and kinetics investigations to explore multiple products initiating from complex reaction. A key aspect of this approach is that the segmented chirps should not overlap with each other in frequency domain.

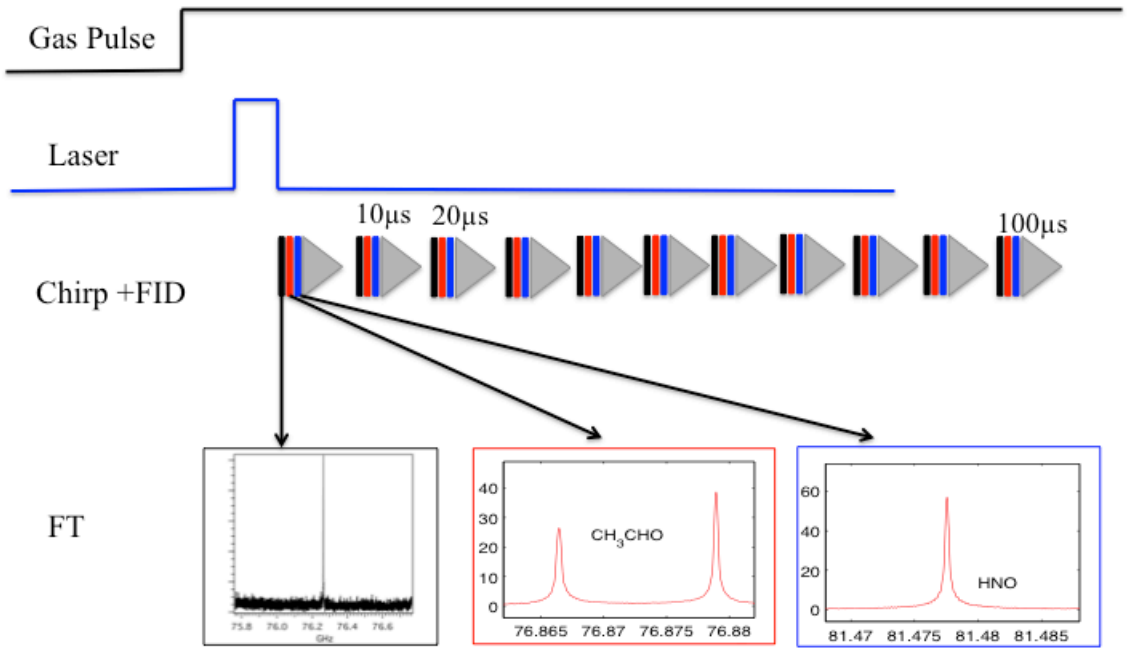

Figure 6.5 Timing sequence for a segmented multichirp setup. Multiple FIDs of multiple chirps are collected at 10µs intervals after the laser per single gas pulse.

6.1.4 Segmented coherent macrochirps

As shown is in Figure 6.6, similar to segmented multichirp approach, distinct transition frequencies are targeted by each narrow multichirp in a single frame for the same gas pulse. The difference in this method is the employment of a macrochirp. A macrochirp is a combination of shorter (~100ns) multichirps coherently spaced among each respective frequency multichirp (red-red, blue-blue). Similar to segmented mutichirp method this could be used inline with the sequential mode to collect time evolution spectra of products initiated from the laser.

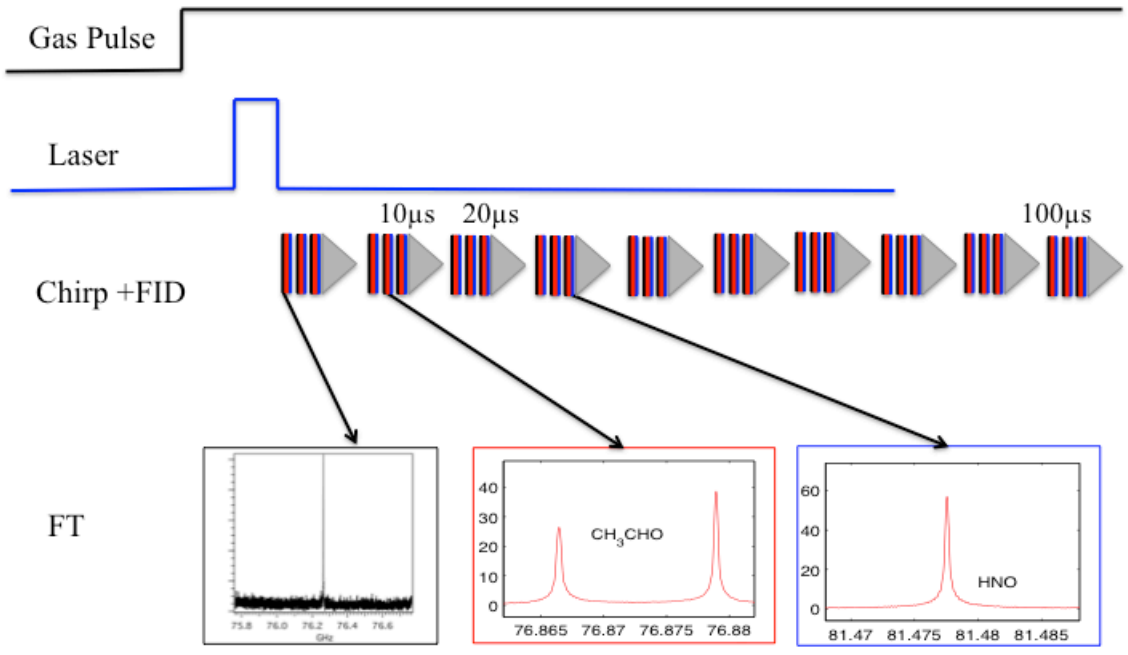

Figure 6.6 Timing sequence for a segmented macrochirp setup. Macrochirps are a combination of multichirp coherently spaced among each frequency chirp.

As discussed in Chapter 4 due to the high operating pressure the collision frequency is much higher in CPUF[108]. Therefore, asymmetry in line intensities are observed for longer chirps depending on how the frequency region is swept, upward or downward. A key advantage of this method is as each frequency multichirp is made to be coherent with each other, we observe a S/N increase with the number of multichirp sets used to construct the macrochirps. Therefore, this is useful to eliminate the line asymmetries by using shorter chirps, while still retaining better signal quality. The elimination of line asymmetry and improvement in signal quality is demonstrated in Figure 6.4 for two rotational transitions of Methylformate (J_{KaKc}= 7_{17}-6_{16} and J_{KaKc}=7_{07}-6_{06}). This method was implemented in Chapter 5 for the CN + CH_3CCH reaction. However coherence can be maintained only for narrow chirps with fairly short delays between them. Furthermore, the gaps between chirps inevitably yield modulations in the FT at particular frequencies. This can be monitored by examining the FT of the chirp itself.

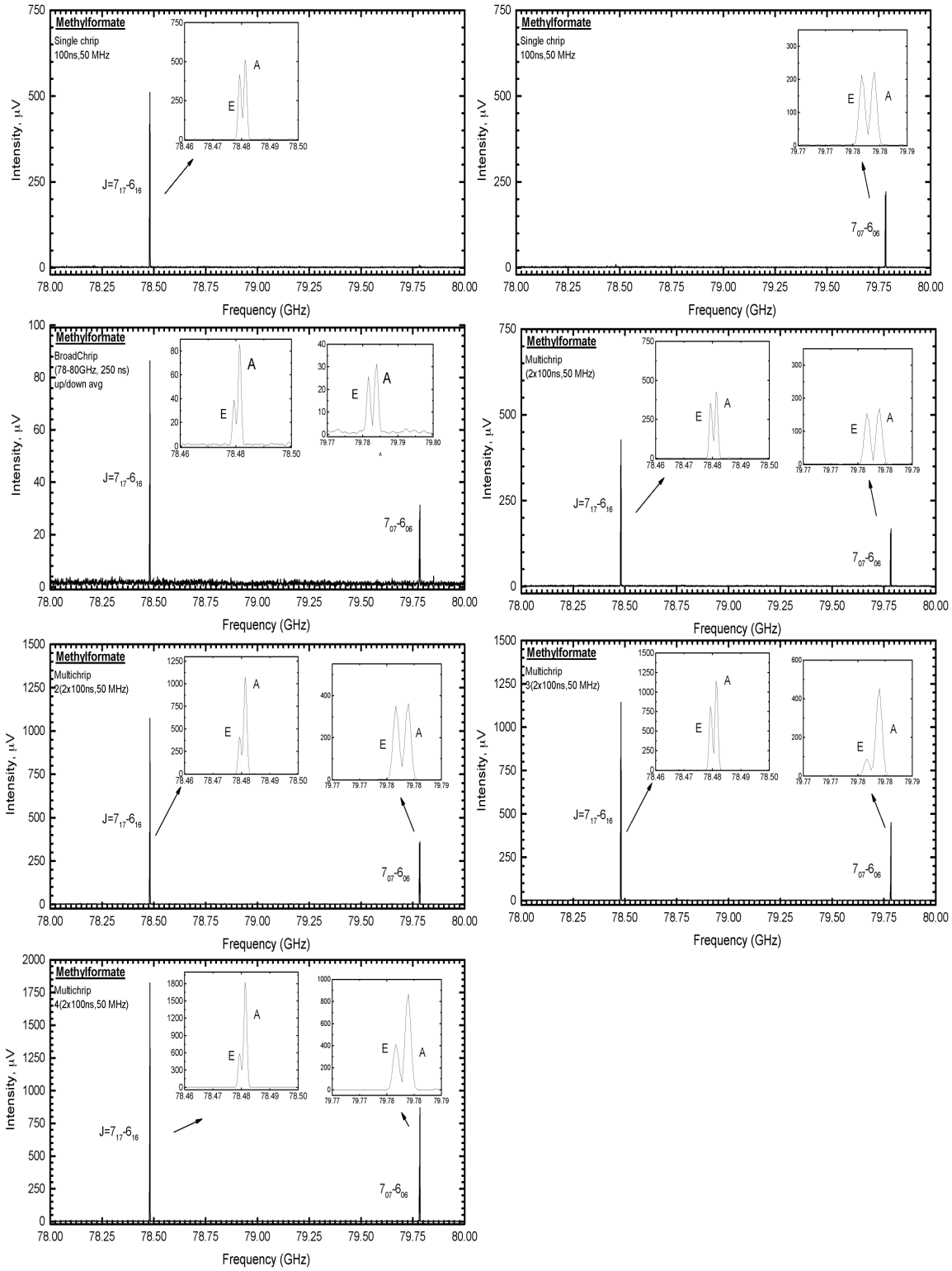

Figure 6.7. The rotation transitions of Methylformate (J_{KaKc}= 7_{17}-6_{16} and J_{KaKc}=7_{07}-6_{06}) studied using the segmented macrochirp approach with differing the number of multichirps.

6.2 Chirped Pulse Microwave spectroscopy with Infrared Multiphoton Dissociation

Infrared Multiphoton Dissociation (IRMPD) is a widely used technique in the study of nascent photofragments originating from dissociation of small molecules in the ground electronic state.[109] IRMPD mainly follows the lowest energy pathways, resembling the products formed from thermal decomposition. With the introduction of powerful TEA-CO_2 lasers, it has evolved to become a useful tool for studying unimolecular dissociation. Due to the rapid absorption of many infrared photons leading to the dissociation near threshold it is well suited for studies of competing processes like radical formation, isomerization and formation of cyclic transition states[110]. By combining IRMPD with CP-FTMW spectroscopy we can explore multidimensional potential energy surfaces on the ground electronic state and aid in interpreting the distribution of final products involved in multiple pathways. The potential of this combination is demonstrated in a preliminary IRMPD study done on the dissociation of Methylnitrite (CH_3ONO). In this case we used a free jet expansion rather than the uniform flow.

HNO, CH_2O and CH_3O are products of the IRMPD methyl nitrite that were observed using the chirped-pulse millimeter-wave (CPmmW) spectrometer. Methyl nitrite, CH_3ONO, was mixed with Ar and expanded supersonically from a pulsed valve into the vacuum chamber. A TEA-CO_2 laser was focused near the orifice of the pulsed valve allowing the dissociation products to experience cooling collisions within the initial stage of supersonic expansion. This is important because the CPmmW signal is

proportional to the population difference, ΔN, between the rotational levels of the mm-wave transition, in this case $J = 1$ and $J = 0$.

The methoxy product is the result of radical elimination

$$CH_3ONO \rightarrow CH_3O + NO \quad (1)$$

The HNO and formaldehyde products,

$$CH_3ONO \rightarrow CH_2O + HNO \quad (2)$$

are likely to form via the roaming mechanism[111].

The IRMPD signal dependence on the fluence of the CO_2 laser was studied for different products. Our preliminary results show in Figure 6.8, that there are approximately equal amounts of methoxy and formaldehyde is being formed. However, the concentration of HNO exceeds, by roughly a factor of 3, the concentration of formaldehyde.

Further investigation is required to eliminate the possibility of bimolecular reaction in the systems. Nevertheless, this demonstrates the potential of this combination to investigate reaction dynamics and evidence of roaming reactions

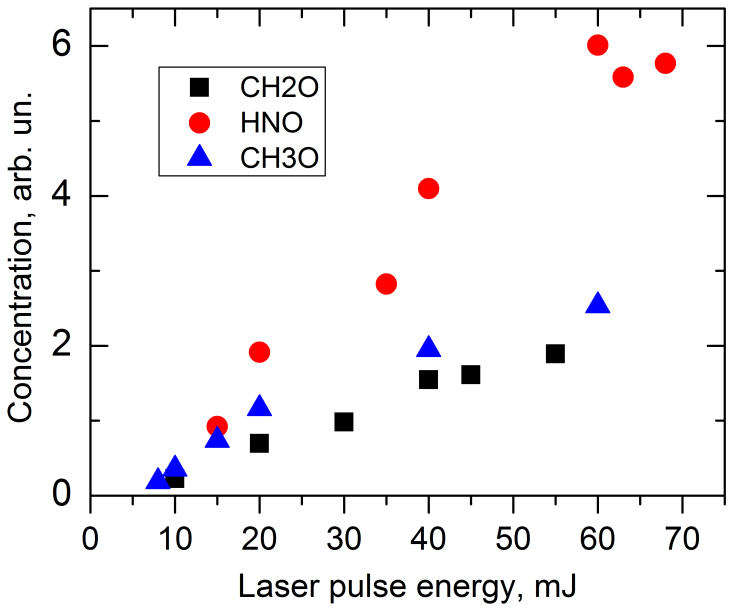

Figure 6.8. The CPmmW signal dependence with the fluence of the CO_2 laser

6.3 Outlook

The promises for CPUF as a powerful tool for studying reaction dynamics has been well established through out this dissertation. Its ability to investigate complex photochemical systems and initiate bimolecular reaction in a known thermally equilibrated environment opens many avenues for future chemical explorers. The ability of CPUF to produce and detect excited states of molecules is demonstrated in previous chapters. The possibility to cool and trap molecules as transient intermediates under uniform flow condition holds promise for new insights into the role of such species in reaction dynamics.

Along the way CPUF has also proven its potential for isomer and conformer specific kinetic investigations. Utilizing its ability to detect and observe the time evolution of

products starting form precursors through reaction intermediates with additional detail of dynamic and kinetic information will be an ideal future application for CPUF. Investigating the future possibilities of new Laval nozzles with different carrier gases and exploiting the continuous advancement in the microwave and millimeter wave components will opening new possibilities for CPUF. The facility to gain access to new frequency regions will broaden the scope of detection and gain access into more complex chemical systems. The recent triumph of chiral detection through rotational spectroscopy[112–114], multidimensional CP spectroscopy[115] and many successful implementations of CP-Radiowave,[116,117] IR and optical double resonance[118] schemes are confirming the enormous potential for CPUF to grow in future

APPENDIX

AIP PUBLISHING LLC LICENSE
TERMS AND CONDITIONS

Jun 02, 2015

All payments must be made in full to CCC. For payment instructions, please see information listed at the bottom of this form.

License Number	3640910765661
Order Date	Jun 02, 2015
Publisher	AIP Publishing LLC
Publication	Journal of Chemical Physics
Article Title	A chirped-pulse Fourier-transform microwave/pulsed uniform flow spectrometer. II. Performance and applications for reaction dynamics
Author	Chamara Abeysekera,Lindsay N. Zack,G. Barratt Park, et al.
Online Publication Date	Dec 5, 2014
Volume number	141
Issue number	21
Type of Use	Thesis/Dissertation
Requestor type	Author (original article)
Format	Print and electronic
Portion	Figure/Table
Number of figures/tables	7
Title of your thesis / dissertation	CHIRPED-PULSE FOURIER TRANSFORM MICROWAVE SPECTROSCOPY IN PULSED UNIFORM SUPERSONIC FLOWS
Expected completion date	Jul 2015
Estimated size (number of pages)	150
Total	0.00 USD
Terms and Conditions	

AIP Publishing LLC -- Terms and Conditions: Permissions Uses

AIP Publishing LLC ("AIPP"") hereby grants to you the non-exclusive right and license to use and/or distribute the Material according to the use specified in your order, on a one-time basis, for the specified term, with a maximum distribution equal to the number that you have ordered. Any links or other content accompanying the Material are not the subject of this license.

1. You agree to include the following copyright and permission notice with the reproduction of the Material:"Reprinted with permission from [FULL CITATION]. Copyright [PUBLICATION YEAR], AIP Publishing LLC." For an article, the copyright and permission notice must be printed on the first page of the article or book chapter. For photographs, covers, or tables, the copyright and permission notice may appear with the Material, in a footnote, or in the reference list.
2. If you have licensed reuse of a figure, photograph, cover, or table, it is your responsibility to ensure that the material is original to AIPP and does not contain the copyright of another entity, and that the copyright notice of the figure, photograph, cover, or table does not indicate that it was reprinted by AIPP, with permission, from another source. Under no circumstances does AIPP, purport or intend to grant permission to reuse material to which it does not hold copyright.
3. You may not alter or modify the Material in any manner. You may translate the Material

AIP PUBLISHING LLC LICENSE
TERMS AND CONDITIONS

Jun 02, 2015

All payments must be made in full to CCC. For payment instructions, please see information listed at the bottom of this form.

License Number	3640910865678
Order Date	Jun 02, 2015
Publisher	AIP Publishing LLC
Publication	Journal of Chemical Physics
Article Title	A chirped-pulse Fourier-transform microwave/pulsed uniform flow spectrometer. I. The low-temperature flow system
Author	James M. Oldham,Chamara Abeysekera,Baptiste Joalland, et al.
Online Publication Date	Oct 20, 2014
Volume number	141
Issue number	15
Type of Use	Thesis/Dissertation
Requestor type	Author (original article)
Format	Print and electronic
Portion	Excerpt (> 800 words)
Will you be translating?	No
Title of your thesis / dissertation	CHIRPED-PULSE FOURIER TRANSFORM MICROWAVE SPECTROSCOPY IN PULSED UNIFORM SUPERSONIC FLOWS
Expected completion date	Jul 2015
Estimated size (number of pages)	150
Total	0.00 USD

Terms and Conditions

AIP Publishing LLC -- Terms and Conditions: Permissions Uses

AIP Publishing LLC ("AIPP"") hereby grants to you the non-exclusive right and license to use and/or distribute the Material according to the use specified in your order, on a one-time basis, for the specified term, with a maximum distribution equal to the number that you have ordered. Any links or other content accompanying the Material are not the subject of this license.

1. You agree to include the following copyright and permission notice with the reproduction of the Material:"Reprinted with permission from [FULL CITATION]. Copyright [PUBLICATION YEAR], AIP Publishing LLC." For an article, the copyright and permission notice must be printed on the first page of the article or book chapter. For photographs, covers, or tables, the copyright and permission notice may appear with the Material, in a footnote, or in the reference list.
2. If you have licensed reuse of a figure, photograph, cover, or table, it is your responsibility to ensure that the material is original to AIPP and does not contain the copyright of another entity, and that the copyright notice of the figure, photograph, cover, or table does not indicate that it was reprinted by AIPP, with permission, from another source. Under no circumstances does AIPP, purport or intend to grant permission to reuse material to which it does not hold copyright.
3. You may not alter or modify the Material in any manner. You may translate the Material into another language only if you have licensed translation rights. You may not use the

AIP PUBLISHING LLC LICENSE
TERMS AND CONDITIONS

Jun 02, 2015

All payments must be made in full to CCC. For payment instructions, please see information listed at the bottom of this form.

License Number	3640911273096
Order Date	Jun 02, 2015
Publisher	AIP Publishing LLC
Publication	Review of Scientific Instruments
Article Title	Note: A short-pulse high-intensity molecular beam valve based on a piezoelectric stack actuator
Author	Chamara Abeysekera,Baptiste Joalland,Yuanyuan Shi, et al.
Online Publication Date	Nov 26, 2014
Volume number	85
Issue number	11
Type of Use	Thesis/Dissertation
Requestor type	Author (original article)
Format	Print and electronic
Portion	Figure/Table
Number of figures/tables	3
Title of your thesis / dissertation	CHIRPED-PULSE FOURIER TRANSFORM MICROWAVE SPECTROSCOPY IN PULSED UNIFORM SUPERSONIC FLOWS
Expected completion date	Jul 2015
Estimated size (number of pages)	150
Total	0.00 USD
Terms and Conditions	

AIP Publishing LLC -- Terms and Conditions: Permissions Uses

AIP Publishing LLC ("AIPP"") hereby grants to you the non-exclusive right and license to use and/or distribute the Material according to the use specified in your order, on a one-time basis, for the specified term, with a maximum distribution equal to the number that you have ordered. Any links or other content accompanying the Material are not the subject of this license.

1. You agree to include the following copyright and permission notice with the reproduction of the Material:"Reprinted with permission from [FULL CITATION]. Copyright [PUBLICATION YEAR], AIP Publishing LLC." For an article, the copyright and permission notice must be printed on the first page of the article or book chapter. For photographs, covers, or tables, the copyright and permission notice may appear with the Material, in a footnote, or in the reference list.
2. If you have licensed reuse of a figure, photograph, cover, or table, it is your responsibility to ensure that the material is original to AIPP and does not contain the copyright of another entity, and that the copyright notice of the figure, photograph, cover, or table does not indicate that it was reprinted by AIPP, with permission, from another source. Under no circumstances does AIPP, purport or intend to grant permission to reuse material to which it does not hold copyright.
3. You may not alter or modify the Material in any manner. You may translate the Material into another language only if you have licensed translation rights. You may not use the

BIBLIOGRAPHY

(1) Herschbach, D. R. Molecular Dynamics of Elementary Chemical Reactions(Nobel Lecture). *Angew. Chemie Int. Ed. English* **1987**, *26* (12), 1221–1243.

(2) Yuan; Lee, T. Molecular Beam Studies of Elementary Chemical Processes. *Angew. Chemie Int. Ed. English* **1987**, *26*, 939–951.

(3) Polanyi, J. C. Some Concepts in Reaction Dynamics. *Science* **1987**, *236* (4802), 680–690.

(4) Casavecchia, P.; Leonori, F.; Balucani, N.; Petrucci, R.; Capozza, G.; Segoloni, E. Probing the Dynamics of Polyatomic Multichannel Elementary Reactions by Crossed Molecular Beam Experiments with Soft Electron-Ionization Mass Spectrometric Detection. *Phys. Chem. Chem. Phys.* **2009**, *11* (1), 46–65.

(5) Yang, X. Probing State-to-State Reaction Dynamics Using H-Atom Rydberg Tagging Time-of-Flight Spectroscopy. *Phys. Chem. Chem. Phys.* **2011**, *13* (18), 8112–8121.

(6) Murray, C.; Orr-Ewing, A. J. The Dynamics of Chlorine-Atom Reactions with Polyatomic Organic Molecules. *Int. Rev. Phys. Chem.* **2004**, *23* (3), 435–482.

(7) Zare, R. N. My Life with LIF: A Personal Account of Developing Laser-Induced Fluorescence. *Annu. Rev. Anal. Chem.* **2012**, *5* (1), 1–14.

(8) Cheikh Sid Ely, S.; Morales, S. B.; Guillemin, J. C.; Klippenstein, S. J.; Sims, I. R. Low Temperature Rate Coefficients for the Reaction CN + HC_3N. *J. Phys. Chem. A* **2013**, *117* (46), 12155–12164.

(9) Chandler, D. W.; Houston, P. L. Two-Dimensional Imaging of State-Selected Photodissociation Products Detected by Multiphoton Ionization. *J. Chem. Phys.* **1987**, *87* (2), 1445.

(10) Eppink, A. T. J. B.; Parker, D. H. Velocity Map Imaging of Ions and Electrons Using Electrostatic Lenses: Application in Photoelectron and Photofragment Ion Imaging of Molecular Oxygen. *Rev. Sci. Instrum.* **1997**, *68* (9), 3477–3484.

(11) Townsend, D.; Minitti, M. P.; Suits, A. G. Direct Current Slice Imaging. *Rev. Sci. Instrum.* **2003**, *74* (4), 2530–2539.

(12) Brown, G. G.; Dian, B. C.; Douglass, K. O.; Geyer, S. M.; Shipman, S. T.; Pate, B. H. A Broadband Fourier Transform Microwave Spectrometer Based on Chirped Pulse Excitation. *Rev. Sci. Instrum.* **2008**, *79* (5), 53103.

(13) Rowe, B. R.; Dupeyrat, G.; Marquette, J. B.; Gaucherel, P. Study of the Reactions $N_2+2N_2 \rightarrow N_4+N_2$ and $O_2+2O_2 \rightarrow O_4+O_2$ from 20 to 160 K by the CRESU Technique. *J. Chem. Phys.* **1984**, *80* (10), 4915.

(14) Sims, I. R.; Queffelec, J. L.; Travers, D.; Rowe, B. R.; Herbert, L. B.; Karthäuser, J.; Smith, I. W. M. Rate Constants for the Reactions of CN with Hydrocarbons at Low and Ultra-Low Temperatures. *Chem. Phys. Lett.* **1993**, *211* (4-5), 461–468.

(15) Rowe, B. R.; Parent, D. C. Techniques for the Study of Reaction Kinetics at Low Temperatures Application to the Atmospheric Chemistry of Titan. *Planet. Sp. Sci* **1995**, *43*, 105 – l 14.

(16) Smith, I. W. M.; Sage, A. M.; Donahue, N. M.; Herbst, E.; Quan, D. The Temperature-Dependence of Rapid Low Temperature Reactions: Experiment, Understanding and Prediction. *Faraday Discuss.* **2006**, *133*, 137–156.

(17) Sims, I. R.; Queffelec, J. L.; Defrance, A.; Rebrion-Rowe, C.; Travers, D.; Bocherel, P.; Rowe, B. R.; Smith, I. W. M. Ultralow Temperature Kinetics of Neutral–neutral Reactions. The Technique and Results for the Reactions CN+O_2 down to 13 K and CN+NH_3 down to 25 K. *J. Chem. Phys.* **1994**, *100* (6), 4229.

(18) Sims, I.; Queffelec, J. L.; Defrance, A.; Rebrion-Rowe, C.; Travers, D.; Rowe, B.; Smith, I. Ultra-Low Temperature Kinetics of Neutral-Neutral Reactions: The Reaction CN + O_2 down to 26 K. *J. Chem. Phys.* **1992**, *97*, 8798–8800.

(19) Daranlot, J.; Jorfi, M.; Xie, C.; Bergeat, A.; Costes, M.; Caubet, P.; Xie, D.; Guo, H.; Honvault, P.; Hickson, K. M. Revealing Atom-Radical Reactivity at Low Temperature through the N + OH Reaction. *Science* **2011**, *334*, 1538–1541.

(20) Atkinson, D. B.; Smith, M. a. Design and Characterization of Pulsed Uniform Supersonic Expansions for Chemical Applications. *Rev. Sci. Instrum.* **1995**, *66* (9), 4434.

(21) Atkinson, D. B.; Smith, M. A. Radical-Molecule Kinetics in Pulsed Uniform Supersonic Flows: Termolecular Association of OH + NO between 90 and 220 K. *J. Phys. Chem.* **1994**, *98* (23), 5797–5800.

(22) Van Marter, T.; Heaven, M. C. I ($^2P_{1/2}$) + O_2: Studies of Low-Temperature Electronic Energy Transfer and Nuclear Spin-State Changing Collisions. *J. Chem. Phys.* **1998**, *109*, 9266–9271.

(23) Lee, S.; Leone, S. R. Rate Coefficients for the Reaction of C_2H with O_2 at 90 K and 120 K Using a Pulsed Laval Nozzle Apparatus. *Chem. Phys. Lett.* **2000**, *329*, 443–449.

(24) Spangenberg, T.; Köhler, S.; Hansmann, B.; Wachsmuth, U.; Abel, B.; Smith, M. A. Low-Temperature Reactions of OH Radicals with Propene and Isoprene in Pulsed Laval Nozzle Expansions. *J. Phys. Chem. A* **2004**, *108*, 7527–7534.

(25) Lee, S.; Hoobler, R. J.; Leone, S. R. A Pulsed Laval Nozzle Apparatus with Laser Ionization Mass Spectroscopy for Direct Measurements of Rate Coefficients at Low Temperatures with Condensable Gases. *Rev. Sci. Instrum.* **2000**, *71*, 1816–1823.

(26) Marcy, T. P.; Díaz, R. R.; Heard, D.; Leone, S. R.; Harding, L. B.; Klippenstein, S. J. Theoretical and Experimental Investigation of the Dynamics of the Production of CO from the CH_3 + O and CD_3 + O Reactions. *J. Phys. Chem. A* **2001**, *105*, 8361–8369.

(27) Van Marter, T.; Heaven, M. C.; Plummer, D. Measurement of the Rate Constant for the Quenching of I ($^2P_{1/2}$) by O_2X at 150 K. *Chem. Phys. Lett.* **1996**, *260*, 201–207.

(28) Hansmann, B.; Abel, B. Kinetics in Cold Laval Nozzle Expansions: From Atmospheric Chemistry to Oxidation of Biomolecules in the Gas Phase. *Chemphyschem* **2007**, *8*, 343–356.

(29) Sánchez-González, R.; Srinivasan, R.; Hofferth, J.; Kim, D. Y.; Tindall, A. J.; W. Bowersox, R. D.; North, S. W. Repetitively Pulsed Hypersonic Flow Apparatus for Diagnostic Development. *AIAA J.* **2012**, *50* (3), 691–697.

(30) Gentry, W. R.; Giese, C. F. Ten-Microsecond Pulsed Molecular Beam Source and a Fast Ionization Detector. *Rev. Sci. Instrum.* **1978**, *49* (5), 595.

(31) Proch, D.; Trickl, T. A High-Intensity Multi-Purpose Piezoelectric Pulsed Molecular Beam Source. *Rev. Sci. Instrum.* **1989**, *60* (4), 713.

(32) Irimia, D.; Dobrikov, D.; Kortekaas, R.; Voet, H.; Van Den Ende, D. a.; Groen, W. a.; Janssen, M. H. M. A Short Pulse (7 μs FWHM) and High Repetition Rate (dc-5kHz) Cantilever Piezovalve for Pulsed Atomic and Molecular Beams. *Rev. Sci. Instrum.* **2009**, *80* (11).

(33) Luria, K.; Lavie, N.; Even, U. Dielectric Barrier Discharge Source for Supersonic Beams. *Rev. Sci. Instrum.* **2009**, *80* (10).

(34) Yan, B.; Claus, P. F. H.; Van Oorschot, B. G. M.; Gerritsen, L.; Eppink, a. T. J. B.; Van De Meerakker, S. Y. T.; Parker, D. H. A New High Intensity and Short-Pulse Molecular Beam Valve. *Rev. Sci. Instrum.* **2013**, *84* (2).

(35) Li, W.; Chambreau, S. D.; Lahankar, S. A.; Suits, A. G. Megapixel Ion Imaging with Standard Video. *Rev. Sci. Instrum.* **2005**, *76* (6).

(36) Ahmed, M.; Peterka, D. S.; Suits, A. G. Crossed-Beam Reaction of $O(^1D)+D_2 \rightarrow OD+D$ by Velocity Map Imaging. *Chem. Phys. Lett.* **1999**, *301* (3-4), 372–378.

(37) Henson, A. B.; Gersten, S.; Shagam, Y.; Narevicius, J.; Narevicius, E. Observation of Resonances in Penning Ionization Reactions at Sub-Kelvin Temperatures in Merged Beams. *Science* **2012**, *338*, 234–238.

(38) Shagam, Y.; Narevicius, E. Sub-Kelvin Collision Temperatures in Merged Neutral Beams by Correlation in Phase-Space. *J. Phys. Chem. C* **2013**, *117* (43), 22454–22461.

(39) Atkinson, D. B.; Smith, M. A. Design and Characterization of Pulsed Uniform Supersonic Expansions for Chemical Applications. *Rev. Sci. Instrum.* **1995**, *66* (9), 4434.

(40) Neill, J. L.; Shipman, S. T.; Alvarez-Valtierra, L.; Lesarri, A.; Kisiel, Z.; Pate, B. H. Rotational Spectroscopy of Iodobenzene and Iodobenzene–neon with a Direct Digital 2–8 GHz Chirped-Pulse Fourier Transform Microwave Spectrometer. *J. Mol. Spectrosc.* **2011**, *269* (1), 21–29.

(41) Nguyen, H. V. L.; Kleiner, I.; Shipman, S. T.; Mae, Y.; Hirose, K.; Hatanaka, S.; Kobayashi, K. Extension of the Measurement, Assignment, and Fit of the Rotational Spectrum of the Two-Top Molecule Methyl Acetate. *J. Mol. Spectrosc.* **2014**, *299*, 17–21.

(42) Reinhold, B.; Finneran, I. A.; Shipman, S. T. Room Temperature Chirped-Pulse Fourier Transform Microwave Spectroscopy of Anisole. *J. Mol. Spectrosc.* **2011**, *270* (2), 89–97.

(43) Finneran, I. A.; Shipman, S. T.; Widicus, S. L. Rotational Spectroscopy of 2-Methylfuran from 8.7 to 960 GHz. *J. Mol. Spectrosc.* **2012**, *280*, 27–33.

(44) Kroll, J. A.; Shipman, S. T.; Widicus Weaver, S. L. The Rotational Spectrum of Methyl Ethyl Ketone in Its Ground Vibrational State. *J. Mol. Spectrosc.* **2014**, *295*, 52–57.

(45) Steber, A. L.; Harris, B. J.; Neill, J. L.; Pate, B. H. An Arbitrary Waveform Generator Based Chirped Pulse Fourier Transform Spectrometer Operating from 260 to 295 GHz. *J. Mol. Spectrosc.* **2012**, *280*, 3–10.

(46) Park, G. B.; Steeves, A. H.; Kuyanov-Prozument, K.; Neill, J. L.; Field, R. W. Design and Evaluation of a Pulsed-Jet Chirped-Pulse Millimeter-Wave Spectrometer for the 70-102 GHz Region. *J. Chem. Phys.* **2011**, *135* (2), 024202.

(47) Gerecht, E.; Douglass, K. O.; Plusquellic, D. F. Chirped-Pulse Terahertz Spectroscopy for Broadband Trace Gas Sensing. *Opt. Express* **2011**, *19* (9), 8973–8984.

(48) Dian, B. C.; Brown, G. G.; Douglass, K. O.; Pate, B. H. Measuring Picosecond Isomerization Kinetics via Broadband Microwave Spectroscopy. *Science* **2008**, *320* (5878), 924–928.

(49) Prozument, K.; Barratt Park, G.; Shaver, R. G.; Vasiliou, A. K.; Oldham, J. M.; David, D. E.; Muenter, J. S.; Stanton, J. F.; Suits, A. G.; Barney Ellison, G.; Field, R. W. Chirped-Pulse Millimeter-Wave Spectroscopy for Dynamics and Kinetics Studies of Pyrolysis Reactions. *Phys. Chem. Chem. Phys.* **2014**.

(50) Kidwell, N. M.; Vaquero-Vara, V.; Ormond, T. K.; Buckingham, G. T.; Zhang, D.; Mehta-Hurt, D. N.; McCaslin, L.; Nimlos, M. R.; Daily, J. W.; Dian, B. C.; Stanton, J. F.; Ellison, G. B.; Zwier, T. S. Chirped-Pulse Fourier Transform

Microwave Spectroscopy Coupled with a Flash Pyrolysis Microreactor: Structural Determination of the Reactive Intermediate Cyclopentadienone. *J. Phys. Chem. Lett.* **2014**, *5*, 2201–2207.

(51) Yoshida, N.; Saito, S. Application of Microwave Spectroscopy to Kinetic Study of the Reaction of Carbonyl Sulfide with Atomic Oxygen. *Bull. Chem. Soc. Jpn.* **1978**, *51* (6), 1635–1638.

(52) Endo, Y.; Tsuchiya, S.; Yamada, C.; Hirota, E.; Koda, S. Microwave Kinetic Spectroscopy of Reaction Intermediates: O+ethylene Reaction at Low Pressure. *J. Chem. Phys.* **1986**, *85* (1986), 4446.

(53) Koda, S.; Endo, Y.; Tsuchiya, S.; Hirota, E. Branching Ratios in Atomic Oxygen (3P) Reactions of Terminal Olefins Studied by Kinetic Microwave Absorption Spectroscopy. *J. Phys. Chem.* **1991**, *95* (3), 1241–1244.

(54) Suits, A. G. Chemical Applications of Synchrotron Radiation- Part I: Dynamics and VUV Spectroscopy; Part II: X-Ray Applications. **2002**, 3–54.

(55) Leone, S. R.; Ahmed, M.; Wilson, K. R. Chemical Dynamics, Molecular Energetics, and Kinetics at the Synchrotron. *Phys. Chem. Chem. Phys.* **2010**, *12* (25), 6564–6578.

(56) Prozument, K.; Suleimanov, Y. V.; Buesser, B.; Oldham, J. M.; Green, W. H.; Suits, A. G.; Field, R. W. A Signature of Roaming Dynamics in the Thermal Decomposition of Ethyl Nitrite: Chirped-Pulse Rotational Spectroscopy and Kinetic Modeling. *J. Phys. Chem. Lett.* **2014**, 3641–3648.

(57) Oldham, J. M.; Abeysekera, C.; Joalland, B.; Zack, L. N.; Prozument, K.; Sims, I. R.; Park, G. B.; Field, R. W.; Suits, A. G. A Chirped-Pulse Fourier-Transform Microwave/pulsed Uniform Flow Spectrometer. I. The Low-Temperature Flow System. *J. Chem. Phys.* **2014**, *141*, 154202.

(58) Zaleski, D. P.; Neill, J. L.; Muckle, M. T.; Seifert, N. a.; Brandon Carroll, P.; Widicus Weaver, S. L.; Pate, B. H. A Ka-Band Chirped-Pulse Fourier Transform Microwave Spectrometer. *J. Mol. Spectrosc.* **2012**, *280*, 68–76.

(59) McGurk, J. C.; Schmalz, T. G.; Flygare, W. H. Fast Passage in Rotational Spectroscopy: Theory and Experiment. *J. Chem. Phys.* **1974**, *60* (11), 4181.

(60) Sims, I. R.; Queffelec, J.-L.; Travers, D.; Rowe, B. R.; Herbert, L. B.; Karthäuser, J.; Smith, I. W. Rate Constants for the Reactions of CN with Hydrocarbons at Low and Ultra-Low Temperatures. *Chem. Phys. Lett.* **1993**, *211*, 461–468.

(61) Brouard, M.; Cireasa, R.; Clark, A. P.; Preston, T. J.; Vallance, C.; Groenenboom, G. C.; Vasyutinskii, O. S. O(^3P_J) Alignment from the Photodissociation of SO_2 at 193 Nm. *J. Phys. Chem. A* **2004**, *108*, 7965–7976.

(62) Cosofret, B. R.; Dylewski, S. M.; Houston, P. L. Changes in the Vibrational Population of SO ($X^3\Sigma^-$) from the Photodissociation of SO_2 between 202 and 207 Nm. *J. Phys. Chem. A* **2000**, *104*, 10240–10246.

(63) Chen, X.; Asmar, F.; Wang, H.; Weiner, B. R. Nascent SO($X^3\Sigma^-$) Vibrational Distributions from the Photodissociation of SO_2, $SOCl_2$, and $(CH_3)_2SO$ at 193 nm. *J. Phys. Chem.* **1991**, *95* (2), 6415–6417.

(64) Katagiri, H.; Sako, T.; Hishikawa, A.; Yazaki, T.; Onda, K.; Yamanouchi, K.; Yoshino, K. Experimental and Theoretical Exploration of Photodissociation of SO_2 via the C^1B_2 State: Identification of the Dissociation Pathway. *J. Mol. Struct.* **1997**, *413-414*, 589–614.

(65) Becker, S.; Braatz, C.; Lindner, J.; Tiemann, E. Investigation of the Predissociation of SO_2: State Selective Detection of the SO and O Fragments. *Chem. Phys.* **1995**, *196* (1-2), 275–291.

(66) Hansen, N.; Andresen, U.; Dreizler, H.; Grabow, J.-U.; Mäder, H.; Temps, F. Fourier Transform Microwave Observation of SO ($X^3\Sigma^-$, v=0-2)Produced by 193 Nm Photodissociation of SO_2 in a Pulsed Supersonic Jet Expansion. *Chem. Phys. Lett.* **1998**, *289*, 311–318.

(67) Ma, J.; Wilhelm, M. J.; Smith, J. M.; Dai, H.-L. Photolysis (193 nm) of SO_2: Nascent Product Energy Distribution Examined through IR Emission. *J. Phys. Chem. A* **2012**, *116* (1), 166–173.

(68) Kanamori, H.; Butler, J. E.; Kawaguchi, K.; Yamada, C.; Hirota, E. Spin Polarization in SO Photochemically Generated from SO2. *J. Chem. Phys.* **1985**, *83* (2), 611.

(69) Braatz, C.; Tiemann, E. State-to-State Dissociation of SO_2 in C^1B_2: Rotational Distributions of the Fragment SO. *Chem. Phys.* **1998**, *229*, 93–105.

(70) Pardo, J. R.; Cernicharo, J.; Goicoechea, J. R.; Guélin, M.; Asensio Ramos, A. MOLECULAR LINE SURVEY OF CRL 618 FROM 80 TO 276 GHz AND COMPLETE MODE. *Astrophys. J.* **2007**, *661* (May 20), 250–261.

(71) Winnewisser, G.; Walmsley, C. M. The Detection of HC_5N and HC_7N in IRC+10216. *Astron. Astrophys.* **1978**, *70*, L37–L39.

(72) Bell, M. B.; Feldman, P. A.; Travers, M. J.; McCarthy, M. C.; Gottlieb, C. A.; Thaddeus, P. Detection of $HC_{11}N$ in the Cold Dust Cloud TMC-1. *Astrophys. J.* **1997**, *483*, L61–L64.

(73) Broten, N. W.; Oka, T.; Avery, L. W.; MacLeod, J. M.; Kroto, H. W. The Detection of HC_9N in Interstellar Space. *Astrophys. J.* **1978**, *223*, L105–L107.

(74) Osamura, Y.; Fukuzawa, K.; Terzieva, R.; Herbst, E. A Molecular Orbital Study of the $HC_3NH^+ + e^-$ Dissociative Recombination and Its Role in the Production of Cyanoacetylene Isomers in Interstellar Clouds. *Astrophys. J.* **1999**, *519*, 697–704.

(75) Bennett, C. J.; Morales, S. B.; Le Picard, S. D.; Canosa, A.; Sims, I. R.; Shih, Y. H.; Chang, A. H. H.; Gu, X.; Zhang, F.; Kaiser, R. I. A Chemical Dynamics, Kinetics, and Theoretical Study on the Reaction of the Cyano Radical (CN; $X^2\Sigma^+$) with Phenylacetylene (C_6H_5CCH; X^1A^1). *Phys. Chem. Chem. Phys.* **2010**, *12*, 8737–8749.

(76) Huang, L. C. L.; Lee, Y. T.; Kaiser, R. I. Crossed Beam Reaction of the Cyanogen Radical, $CN(X^2\Sigma^+)$, with Acetylene, $C_2H_2(X^1\Sigma_g^+)$: Observation of Cyanoacetylene, $HCCCN(X^1\Sigma^+)$. *J. Chem. Phys.* **1999**, *110* (15), 7119.

(77) Balucani, N.; Asvany, O.; Huange, L. C. L.; Lee, Y. T.; Kaiser, R. I.; Osamura, Y.; Bettinger, H. F. Formation of Nitriles in the Interstellar Medium via Reactions of Cyano Radicals, CN ($X^2\Sigma^+$), with Unsaturated Hydrocarbons. *Astrophys. J.* **2000**, *545*, 892–906.

(78) Tielens, A. The Molecular Universe. *Rev. Mod. Phys.* **2013**, *85* (3), 1021.

(79) Wakelam, V.; Smith, I. W. M.; Herbst, E.; Troe, J.; Geppert, W.; Linnartz, H.; Öberg, K.; Roueff, E.; Agúndez, M.; Pernot, P. Reaction Networks for Interstellar Chemical Modelling: Improvements and Challenges. *Space Sci. Rev.* **2010**, *156* (1-4), 13–72.

(80) Suits, A. G. Photodissociation and Reaction Dynamics Studies Using Third-Generation Synchrotron Radiation. *Chem. Appl. Synchrotron Radiation-Part I Dyn. VUV Spectrosc. Part II X-Ray Appl. Ser. Adv. Ser. Phys. Chem. ISBN 9789812775757. World Sci. Publ. Co. Pte. Ltd., Ed. by Tsun-Kong Sham, vol* **2002**, *12*, 3–54.

(81) Trevitt, A. J.; Soorkia, S.; Savee, J. D.; Selby, T. S.; Osborn, D. L.; Taatjes, C. A.; Leone, S. R. Branching Fractions of the CN+ C_3H_6 Reaction Using Synchrotron Photoionization Mass Spectrometry: Evidence for the 3-Cyanopropene Product. *J. Phys. Chem. A* **2011**, *115* (46), 13467–13473.

(82) Hansen, N.; Miller, J. A.; Westmoreland, P. R.; Kasper, T.; Kohse-Höinghaus, K.; Wang, J.; Cool, T. A. Isomer-Specific Combustion Chemistry in Allene and Propyne Flames. *Combust. Flame* **2009**, *156* (11), 2153–2164.

(83) Jamal, A.; Mebel, A. M. Theoretical Investigation of the Mechanism and Product Branching Ratios of the Reactions of Cyano Radical with 1-and 2-Butyne and 1, 2-Butadiene. *J. Phys. Chem. A* **2013**, *117* (4), 741–755.

(84) Avery, L. W.; Broten, N. W.; MacLeod, J. M.; Oka, T.; Kroto, H. W. Detection of the Heavy Interstellar Molecule Cyanodiacetylene. *Astrophys. J.* **1976**, *205*, L173–L175.

(85) Belloche, A.; Garrod, R. T.; Müller, H. S. P.; Menten, K. M. Detection of a Branched Alkyl Molecule in the Interstellar Medium: Iso-Propyl Cyanide. *Science (80).* **2014**, *345* (6204), 1584–1587.

(86) Turner, B. E. Detection of Interstellar Cyanoacetylene. *Astrophys. J.* **1971**, *163*, L35–L39.

(87) Biennier, L.; Carles, S.; Cordier, D.; Guillemin, J.-C.; Le Picard, S. D.; Faure, A. Low Temperature Reaction Kinetics of CN+HC_3N and Implications for the Growth of Anions in Titan's Atmosphere. *Icarus* **2014**, *227*, 123–131.

(88) Cordiner, M. A.; Nixon, C. A.; Teanby, N. A.; Irwin, P. G. J.; Serigano, J.; Charnley, S. B.; Milam, S. N.; Mumma, M. J.; Lis, D. C.; Villanueva, G. ALMA Measurements of the HNC and HC_3N Distributions in Titan's Atmosphere. *Astrophys. J. Lett.* **2014**, *795* (2), L30.

(89) Cordiner, M. A.; Palmer, M. Y.; Nixon, C. A.; Irwin, P. G. J.; Teanby, N. A.; Charnley, S. B.; Mumma, M. J.; Kisiel, Z.; Serigano, J.; Kuan, Y.-J. Ethyl Cyanide on Titan: Spectroscopic Detection and Mapping Using ALMA. *arXiv:1410.5325* **2014**.

(90) Loison, J. C.; Hébrard, E.; Dobrijevic, M.; Hickson, K. M.; Caralp, F.; Hue, V.; Gronoff, G.; Venot, O.; Bénilan, Y. The Neutral Photochemistry of Nitriles, Amines and Imines in the Atmosphere of Titan. *Icarus* **2015**, *247*, 218–247.

(91) Carty, D.; Page, V. Le; Sims, I. R.; Smith, I. W. M. Low Temperature Rate Coe Cients for the Reactions of CN and C_2H Radicals with Allene $CH_2=C=CH_2$ and Methyl Acetylene (CH_3CCH). *Chem. Phys. Lett.* **2001**, *344* (August), 310–316.

(92) Morales, S. B.; Le Picard, S. D.; Canosa, A.; Sims, I. R. Experimental Measurements of Low Temperature Rate Coefficients for Neutral-Neutral Reactions of Interest for Atmospheric Chemistry of Titan, Pluto, and Triton: Reactions of the CN Radical. *Faraday Discuss. Chem. Soc.* **2010**, *147*, 155–171.

(93) Kaiser, R. I. Experimental Investigation on the Formation of Carbon-Bearing Molecules in the Interstellar Medium via Neutral-Neutral Reactions. *Chem. Rev.* **2002**, *102* (5), 1309–1358.

(94) Kaiser, R. I.; Balucani, N. The Formation of Nitriles in Hydrocarbon-Rich Atmospheres of Planets and Their Satellites: Laboratory Investigations by the Crossed Molecular Beam Technique. *Acc. Chem. Res.* **2001**, *34* (9), 699–706.

(95) Rice, O. K.; Ramsperger, H. C. THEORIES OF UNIMOLECULAR GAS REACTIONS AT LOW PRESSURES. *J. Am. Chem. Soc.* **1931**, *53* (3), 1929–1932.

(96) Marcus, R. Unimolecular Dissociations and Free Radical Recombination Reactions. *J. Chem. Phys.* **1952**, *20* (3), 359.

(97) Kassel, L. S. Studies in Homogeneous Gas Reactions. I. *J. Phys. Chem.* **1928**, *32* (2), 225–242.

(98) Abeysekera, C.; Joalland, B.; Shi, Y.; Kamasah, A.; Oldham, J. M.; Suits, A. G. Note: A Short-Pulse High-Intensity Molecular Beam Valve Based on a Piezoelectric Stack Actuator. *Rev. Sci. Instrum.* **2014**, *85* (11), 116107.

(99) Balucani, N.; Asvany, O.; Kaiser, R.-I.; Osamura, Y. Formation of Three C4H3N Isomers from the Reaction of CN ($X^2\Sigma^+$) with Allene, H_2CCCH_2 (X^1A^1), and Methylacetylene, CH_3CCH (X^1A^1): A Combined Crossed Beam and Ab Initio Study. *J. Phys. Chem. A* **2002**, *106* (17), 4301–4311.

(100) Steber, A. L.; Harris, B. J.; Neill, J. L.; Pate, B. H. An Arbitrary Waveform Generator Based Chirped Pulse Fourier Transform Spectrometer Operating from 260 to 295GHz. *J. Mol. Spectrosc.* **2012**, *280*, 3–10.

(101) Haipern, J. B.; Jackson, W. M. Partitioning of Excess Energy in the Photolysis of Cyanogen Chloride and Cyanogen Bromlde at 193 nm. *J. Phys. Chem* **1982**, *4794* (9), 3528–3533.

(102) Division, L. C. Photodissociation of C_2N_2, CICN, and BrCN in a Pulsed Molecular Beam. *J. Phys. Chem* **1984**, *88*, 3419–3425.

(103) Robinson, J. C.; Sveum, N. E.; Goncher, S. J.; Neumark, D. M. Photofragment Translational Spectroscopy of Allene, Propyne, and Propyne-d3 at 193 Nm. *Mol. Phys.* **2005**, *103* (13), 1765–1783.

(104) Müller, H. S. P.; Schlöder, F.; Stutzki, J.; Winnewisser, G. The Cologne Database for Molecular Spectroscopy, CDMS: A Useful Tool for Astronomers and Spectroscopists. *J. Mol. Struct.* **2005**, *742* (1-3), 215–227.

(105) Huang, C. H.; Kaiser, R. I.; Chang, A. H. H. Theoretical Study on the Reaction of Ground State Cyano Radical with Propylene in Titan's Atmosphere. *J. Phys. Chem. A* **2009**, *113*, 12675–12685.

(106) Neill, J. L.; Harris, B. J.; Steber, A. L.; Douglass, K. O.; Plusquellic, D. F.; Pate, B. H. Segmented Chirped-Pulse Fourier Transform Submillimeter Spectroscopy for Broadband Gas Analysis. **2013**, *21* (17), 19743–19749.

(107) Prozument, K.; Park, G. B.; Shaver, R. G.; Vasiliou, A. K.; Oldham, J. M.; David, D. E.; Muenter, J. S.; Stanton, J. F.; Suits, A. G.; Ellison, G. B.; Field, R. W. Chirped-Pulse Millimeter-Wave Spectroscopy for Dynamics and Kinetics Studies of Pyrolysis Reactions. *Phys. Chem. Chem. Phys.* **2014**, *16* (30), 15739–15751.

(108) Park, G. B.; Field, R. W. Edge Effects in Chirped-Pulse Fourier Transform Microwave Spectra. *J. Mol. Spectrosc.* **2015**, *312*, 54–57.

(109) Isenor, N. R. Dissociation and Breakdown of Molecular Gases by Pulsed CO_2 Laser Radiation. *Appl. Phys. Lett.* **1971**, *18* (6), 224.

(110) Dey, A.; Fernando, R.; Abeysekera, C.; Homayoon, Z.; Bowman, J. M.; Suits, A. G. Photodissociation Dynamics of Nitromethane and Methyl Nitrite by Infrared Multiphoton Dissociation Imaging with Quasiclassical Trajectory Calculations: Signatures of the Roaming Pathway. *J. Chem. Phys.* **2014**, *140* (5), 054305.

(111) Zhu, R. S.; Raghunath, P.; Lin, M. C.; Nguyen, M. T.; Le, H. T.; Hajgató, B.; Veszprémi, T.; Lin, M. C. Effect of Roaming Transition States upon Product Branching in the Thermal Decomposition of CH_3NO_2. *J. Phys. Chem. A* **2013**, *117* (21), 4286–4291.

(112) Patterson, D.; Schnell, M.; Doyle, J. M. Enantiomer-Specific Detection of Chiral Molecules via Microwave Spectroscopy. *Nature* **2013**, *497* (7450), 475–477.

(113) Lobsiger, S.; Perez, C.; Evangelisti, L.; Lehmann, K. K.; Pate, B. H. Molecular Structure and Chirality Detection by Fourier Transform Microwave Spectroscopy. *J. Phys. Chem. Lett.* **2015**, *6* (1), 196–200.

(114) Medcraft, C.; Wolf, R.; Schnell, M. High-Resolution Spectroscopy of the Chiral Metal Complex [CpRe(CH_3)(CO)(NO)]: A Potential Candidate for Probing Parity Violation. *Angew. Chemie Int. Ed.* **2014**, *53* (43), 11656–11659.

(115) Wilcox, D. S.; Hotopp, K. M.; Dian, B. C. Two-Dimensional Chirped-Pulse Fourier Transform Microwave Spectroscopy. *J. Phys. Chem. A* **2011**, *115* (32), 8895–8905.

(116) Schmitz, D.; Alvin Shubert, V.; Betz, T.; Schnell, M. Multi-Resonance Effects within a Single Chirp in Broadband Rotational Spectroscopy: The Rapid Adiabatic Passage Regime for Benzonitrile. *J. Mol. Spectrosc.* **2012**, *280* (1), 77–84.

(117) Schmitz, D.; Shubert, V. A.; Patterson, D.; Krin, A.; Schnell, M. Phase Dependence of Double-Resonance Experiments in Rotational Spectroscopy. *J. Phys. Chem. Lett.* **2015**, 1493–1498.

(118) Park, G. B.; Womack, C. C.; Whitehill, A. R.; Jiang, J.; Ono, S.; Field, R. W. Millimeter-Wave Optical Double Resonance Schemes for Rapid Assignment of Perturbed Spectra, with Applications to the $\tilde{C}^1B_2$ State of SO_2. *J. Chem. Phys.* **2015**, *142* (14), 144201.

ABSTRACT

CHIRPED-PULSE FOURIER TRANSFORM MICROWAVE SPECTROSCOPY IN PULSED UNIFORM SUPERSONIC FLOWS

by

CHAMARA S.W. ABEYSEKERA

August 2015

Advisor: Arthur G. Suits

Major: Chemistry (Physical)

Degree: Doctor of Philosophy

This dissertation is focused on the development of a new experimental apparatus that combines two powerful techniques: Chirped-Pulse Fourier-Transform Microwave (CP-FTMW) spectroscopy and uniform supersonic flows. This combination promises a nearly universal detection method that can deliver quantitative isomer, conformer, and vibrational level specific detection; characterize unstable reaction products and intermediates; and perform unique spectroscopic, kinetics and dynamics measurements.

Thus, a new high-power K_a band (26 – 40 GHz) chirped pulse spectrometer with sub-MHz resolution was designed and constructed. In order to study smaller molecules, E-band (60 – 90 GHz) capabilities were also added to the spectrometer. A novel strategy for generating a pulsed uniform supersonic flow through a Laval nozzle is introduced. A new high-throughput pulsed piezoelectric stack valve was constructed and used to

produce a cold (20 K) uniform flow with large volumes and densities (~10^{16} molecules cm^{-3}). The uniform flow conditions for two of noble gases (argon and helium) were characterized using impact pressure measurements and rotational diagrams. It was demonstrated that a flow uniformity extending as far as 20 cm from the Laval nozzle exit can be achieved with a single compound turbo-molecular pump to maintain the operating pressure.

Two benchmark reactive systems were used to illustrate and characterize the performance of the new apparatus CPUF: the photodissociation of SO_2 at 193 nm, for which the vibrational populations of the SO product are monitored, and the reaction between CN and C_2H_2, for which the HCCCN product is detected in its vibrational ground-state. The results show that the combination also provides insight into the vibrational and rotational relaxation kinetics of the nascent reaction products.

CPUF has been used to determine product branching in a multichannel reaction. This work, the CN + CH_3CCH reaction was found to yield HCN via a direct H-abstraction reaction, while indirect addition/elimination pathways to HC_3N, CH_3C_3N, and H_2C_3HCN were also probed. From these observations, quantitative branching ratios were established for all products as 12(5)%, 66(4)%, 22(6)% and 0(8)% into HCN, HC_3N, CH_3C_3N, and H_2C_3HCN, respectively. The values are consistent with statistical calculations based on new ab initio results at the CBS-QB3 level of theory. New designer chirp schemes were developed for CPUF, targeting broader applications through reduced data acquisition time and enhanced signal.

AUTOBIOGRAPHICAL STATEMENT

CHAMARA S.W. ABEYSEKERA

Education:

August 2015 Ph.D. Chemistry (anticipated), Wayne State University
July 2009 B.S. in Chemistry, University of Peradeniya

Awards and Honors:

2015 Dan Trivich Memorial Award for Research in Physical Chemistry
2015 Graduate School Summer Dissertation Fellowship

Recent Publications**:**

1. C. Abeysekera, B. Joalland, N. Ariyasingha, L.N. Zack I. Sims, R. W. Field, A. G. Suits, Product branching in the low temperature reaction of CN with propyne by chirped-pulse microwave spectroscopy in a uniform supersonic flow. *J. Phys. Chem. Lett.* (2015), 6, 1599−1604 : DOI: 10.1021/acs.jpclett.5b00519
2. C. Abeysekera, B. Joalland, Y. Shi, A. Kamasah, J.M Oldham, A.G. Suits, A short-pulse high-intensity molecular beam valve based on a piezoelectric stack actuator. *Rev. Sci. Instrum.s* (2014) 85, 116107. DOI:10.1063/1.4902153
3. C. Abeysekera, L.N. Zack, G.B. Park, B. Joalland, J.M Oldham, K. Prozument, Nuwandi M. Ariyasingha, I.R. Sims, R.W. Field, A.G. Suits, A Chirped-Pulse Fourier-Transform Microwave/Pulsed Uniform Supersonic Flow Spectrometer: II. Performance and applications for reaction dynamics. *J. Chem. Phys*. (2014) 141, 214203. DOI:10.1063/1.4903253
4. J. M. Oldham, C. Abeysekera, B. Joalland, L. N. Zack, K. Prozument, G.B. Park I. R. Sims, R. W. Field, and A. G. Suits, A Chirped-Pulse Fourier-Transform Microwave/Pulsed Uniform Supersonic Flow Spectrometer: I. The Low-Temperature Flow System. *J. Chem. Phys.* (2014) 141, 154202. DOI:10.1063/1.4897979.
5. A. Dey, R. Fernando, C. Abeysekera, Z. Homayoon, J. M. Bowman, A. G. Suits, Photodissociation dynamics of nitromethane and methyl nitrite by infrared multiphoton dissociation imaging with quasiclassical trajectory calculations: Signatures of the roaming pathway. *J. Chem. Phys*. 140, 054305 (2014). DOI: 10.1063/1.4862691.
6. Z. Homayoon, J. M. Bowman, A. Dey, C. Abeysekera, R. Fernando, A. G. Suits, Experimental and Theoretical Studies of Roaming Dynamics in the Unimolecular Dissociation of CH_3NO_2 to CH_3O + NO. *Z. Phys. Chem*. (2013) DOI: 10.1524/zpch.2013.0409.